Mechanistic Studies on Photoinduced Reduction of a Flavin Cofactor in (6–4) Photolyase

Yuhei Hosokawa

March 2022

Mechanistic Studies on Photoinduced Reduction of a Flavin Cofactor in (6–4) Photolyase

A dissertation submitted to

THE GRADUATE SCHOOL OF ENGINEERING SCIENCE

OSAKA UNIVERSITY

in partial fulfillment of the requirements for the degree of

DOCTOR OF PHILOSOPHY IN SCIENCE

By

Yuhei Hosokawa

March 2022

Abstract

Life has been exposed to sunlight and evolutionarily developed ways to utilize it for an energy source and external stimulus. In contrast to the beneficial aspects of sunlight for life, the exposure of ultraviolet (UV) radiation from the sun has harmful effects on deoxyribonucleic acid (DNA), in which the sequence of nucleobases encodes genetic information. The UV irradiation of DNA alters the chemical structure of two adjacent pyrimidine nucleobases, yielding cyclobutane pyrimidine dimers (CPDs) and pyrimidine(6–4)pyrimidone photoproducts ((6–4) PPs). Because the DNA containing the unusual nucleobases are potential major carcinogens, organisms have repair machineries to remove them. Photolyases (PLs) are ancient but powerful enzymes that repair the UV-induced lesions, and found in all kingdoms of life. PLs have evolutionarily diverged into cryptochromes (CRYs), photoreceptive proteins involved in various signal transductions, represented by circadian rhythm regulation, but no longer able to repair the DNA lesions. Despite of the functional diversity, PLs and CRYs form a **P**hotolyase/**C**ryptochrome **S**uper**f**amily (PCSf) and share a similar architecture and a common flavin adenine dinucleotide (FAD) cofactor. In most PCSf proteins, reduction of FAD is required to express the functions and accomplished by a conserved process called photoactivation or photoreduction.

I have been interested in FAD photoreduction in PCSf proteins because of the following two aspects: (1) the reaction proceeds via formation of photoinduced charge-separated states between FAD and Trp residues, which are stabilized by a variety of ingenious strategies; (2) the conserved photoreduction process triggers various physiological functions, depending on the PCSf proteins. In

this thesis, I exclusively focused on the photoreduction in (6–4) PLs from plants and discovered new mechanisms stabilizing the charge-separated states, though unique to the plant (6–4) PLs. Interestingly, I also found that the FAD photoreduction in plant (6–4) PL accompanies conformational changes of the protein, which could also take place in and be relevant to a wide range of PCSf proteins.

In Chapter 1, I summarized physiological functions of PCSf proteins which are activated by photoreduction of FAD. It is noted that cryptochromes undergo structural changes upon the photoreduction to trigger biological events represented by circadian rhythm regulation. Because the process of FAD photoreduction has been optimized for each protein in the process of evolution, strategies that stabilize the photoinduced charge-separated states during the photoreduction were classified and described in detail. In the end of the chapter, one will find out the possibility that photoreduction in plant (6–4) PLs takes place via undefined mechanisms stabilizing the charge-separated states.

To reveal a factor that stabilizes the photoinduced charge-separated states in plant (6–4) PLs, I focused on the surroundings of the final electron donating Trp residue, because the environment of the FAD in plant (6–4) PLs is shared with that in other (6–4) PLs. In Chapter 2, a combination of computational and experimental analyses suggested that a water molecule is captured with a fixed orientation in a close proximity to the Trp residue and plays a key role in the photoreduction. The new insights obtained in the study will inspire future studies on the functions of surroundings of an electron donating Trp residue in other PCSf proteins.

In Chapter 3, I tried to uncover mechanisms enabling the water molecule mentioned in the

previous chapter to participate in photoreduction. By comparing the surrounding amino acid residues of the Trp residue between plant and animal (6–4) PLs, I discovered that the Trp residue is exclusively solvated with the captured water molecule by inhibiting access of the bulk solvent to the Trp residue. Time-resolved spectroscopy revealed that the regulated solvation controls lifetimes of the photoinduced charge-separated states. The mechanisms newly identified in plant (6–4) PLs will expand the arsenal of tricks employed by PCSf proteins to achieve efficient photoreduction.

In Chapter 4, I shed light on conformational changes in plant (6–4) PLs accompanied by FAD photoreduction. A combination of structural analyses, electrochemical measurements, and steady-state photoreduction kinetics suggested that photoinduced helix movements have an impact on photoreduction ability in plant (6–4) PLs. Because the helix movements could be conserved in other photolyases and cryptochromes, the new insights into photoinduced rearrangements could be helpful to understand the structural changes in cryptochrome.

Contents

Chapter 1

General introduction

1.1 Biological effects of sunlight

1.1.1 Sunlight indispensable to life

Since life appeared on Earth around 3.95 billion years ago[1], organisms on Earth is continuously exposed to sunlight. One of the biggest events in the history of life is the emergence of cyanobacteria around 2.7 billion years ago[2,3]. The cyanobacteria are the ancient oxygenic photosynthetic organisms that convert solar energy into chemical energy and release free oxygen (O_2) as a byproduct. The following rise of the O_2 level on Earth led to evolution of organisms to perform aerobic respiration and caused the diversity and complexity of life, because the aerobic respiration can produce more energy than anaerobic respiration[4].

Sunlight is indispensable to life not only as an energy source but also as an informative stimulus. Organisms have developed visual perception using photoreceptor proteins[5], which allowed them to visually sense the surrounding environment and the presence of predators. As well as the visual perception, circadian rhythm, in which internal rhythm is oscillated with a period of approximately 24 hours, has been exploited to adapt to the environment. Although circadian rhythm is generated autonomously, light plays an essential role in synchronizing it with an environment precisely[6].

1.1.2 Harmful effects of solar energy

In contrast to the benefit of sunlight to life, the exposure of ultraviolet (UV) radiation from the sun has harmful effects on organisms. Indeed, UV-B (ranging from 280 to 315 nm) and UV-C

(ranging from 100 to 280 nm) lights are known as major carcinogens inducing skin cancer in human[7]. The unfavorable effect of UV irradiation is originated from the formation of UV-induced DNA lesions. Upon excitation of DNA by the UV light, photocycloaddition between two adjacent pyrimidine takes place and results in formation of two major types of DNA lesions: cyclobutane pyrimidine dimers (CPDs) and pyrimidine(6–4)pyrimidone photoproducts ((6–4) PPs). The formation of (6–4) PPs in the case of two thymine bases accompanies a transfer of the O4' in the 3' side to the 5' side via an oxetane intermediate, as shown in Figure 1[8]. Because the DNA damage leads to mutagenesis[9] and cell death[10] by inhibiting DNA replication and transcription, organisms have repair machineries to remove the lesions and maintain their genome integrity. In human, a nucleotide excision repair (NER) system, where many proteins are involved, is responsible for the purpose. The necessity of NER is confirmed by genetic disorders such as xeroderma pigmentosum[11], Cockayne syndrome[12], and trichothiodystrophy[13], in which NER-related genes are inherently abnormal. These genetic diseases are associated with the extremely high sensitivity of the skin to UV and the severe risk of UV-induced skin cancer[14].

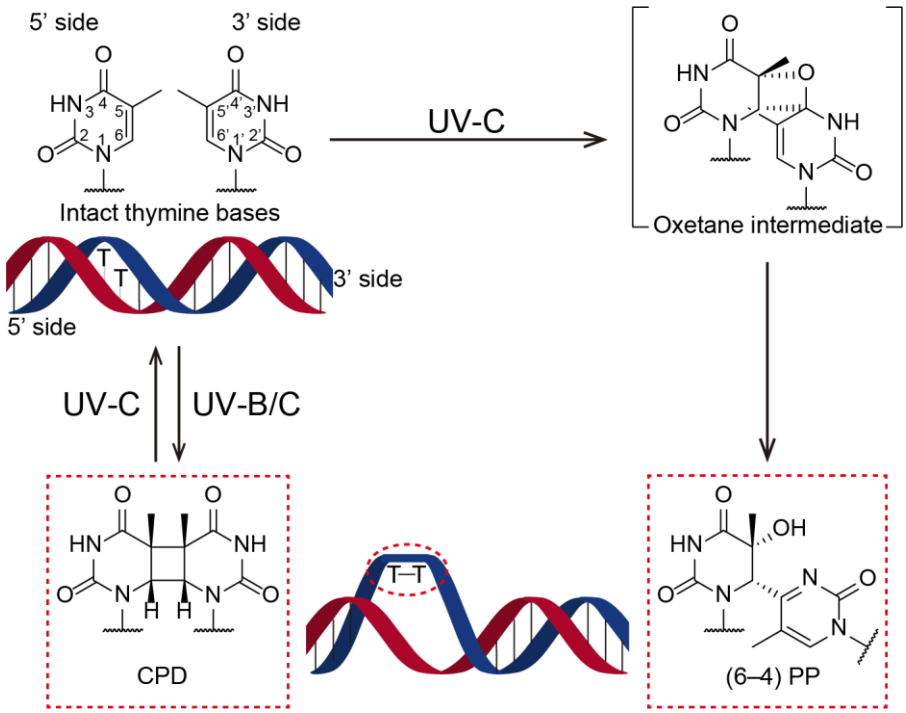

Figure 1. Formation of UV-induced DNA lesions between two adjacent thymine bases. The deoxyribose group is omitted from the chemical structures. The graphic representations illustrate the configurational effect of the crosslinks produced by CPD and (6–4) PP (shown in T–T) on DNA. The abnormal bases are repaired by some repair machineries to maintain the genome integrity of life.

1.2 Light-dependent reactions involved in photolyases

1.2.1 Repair of UV-damaged DNA by photolyases

In addition to the NER system, many organisms, from bacteria to vertebrate animals except for placental mammals, have powerful DNA repair enzymes called photolyases (PLs) able to repair the UV-induced lesions[15]. It is interesting that the repair by PLs does not require any other proteins but utilizes blue light to initiate the repair reaction. The findings of the light-induced reaction were reported in 1949, where the viability of UV-irradiated bacteria and bacteriophages was recovered by visible light treatment[16,17]. After the early study on the curious phenomenon, PLs were identified as responsible enzymes to perform the unique function[18,19].

PLs are flavoenymes[20] non-covalently harboring flavin adenine dinucleotide (FAD) as a catalytic cofactor and are divided into two major classes depending on their substrates. CPD PLs and (6–4) PLs[21] specifically repair the DNA containing CPDs and (6–4) PPs, respectively. Although a recent study reported the possibility that the Antarctic bacterium *Sphingomonas* sp. possesses a protein called UV9 to repair both substrates, the knowledge about how UV9 recognizes and repairs its substrates has not been matured[22]. The repair mechanism by CPD PLs and (6–4) PLs is partly shared, as suggested by the structural similarity between both enzymes (Figures 2a and b). In the case of both CPD PLs and (6–4) PLs, photoexcitation of the two-electron reduced anionic state of FAD ($FADH^-$) triggers an electron transfer to their substrates and following repair reactions[15]. In contrast to the repair of a CPD substrate, where the inserted electron splits the cyclobutane ring within 1 ns to yield intact nucleobases[23] (Figure 2a), the reaction mechanism repairing a (6–4) PP substrate is more complex than for the CPD repair, due to the demand for a transfer of a functional group (O4'H in Figure 2b) in the 5' side to the 3' side. While several reaction models for (6–4) PLs were proposed[24-26], a computational study in 2010[27] suggested that (6–4) PLs should require two photons to repair the substrates. In spite of the experimental difficulty to distinguish between a single-photon and two-photon process, Yamamoto *et al*. demonstrated in 2013[28] that the first photon process does not yield the intact nucleobases but does a long-lived intermediate (approximately 100 s of lifetime at 10 °C) with a low quantum yield ($5.8\% \leq \eta_1 \leq 8.8\%$), and the second photon process for the intermediate accomplishes the repair with a high quantum yield ($47\% \leq \eta_2 \leq 100\%$) equivalent to the value for the CPD repair by CPD PL ($40\% \leq \eta \leq 100\%$)[29]. While the structure of the intermediate has not been

resolved yet, the high quantum yield in the second photon process and the computational study[27] strongly suggest an oxetane-bridged dimer in Figure 2b as the intermediate.

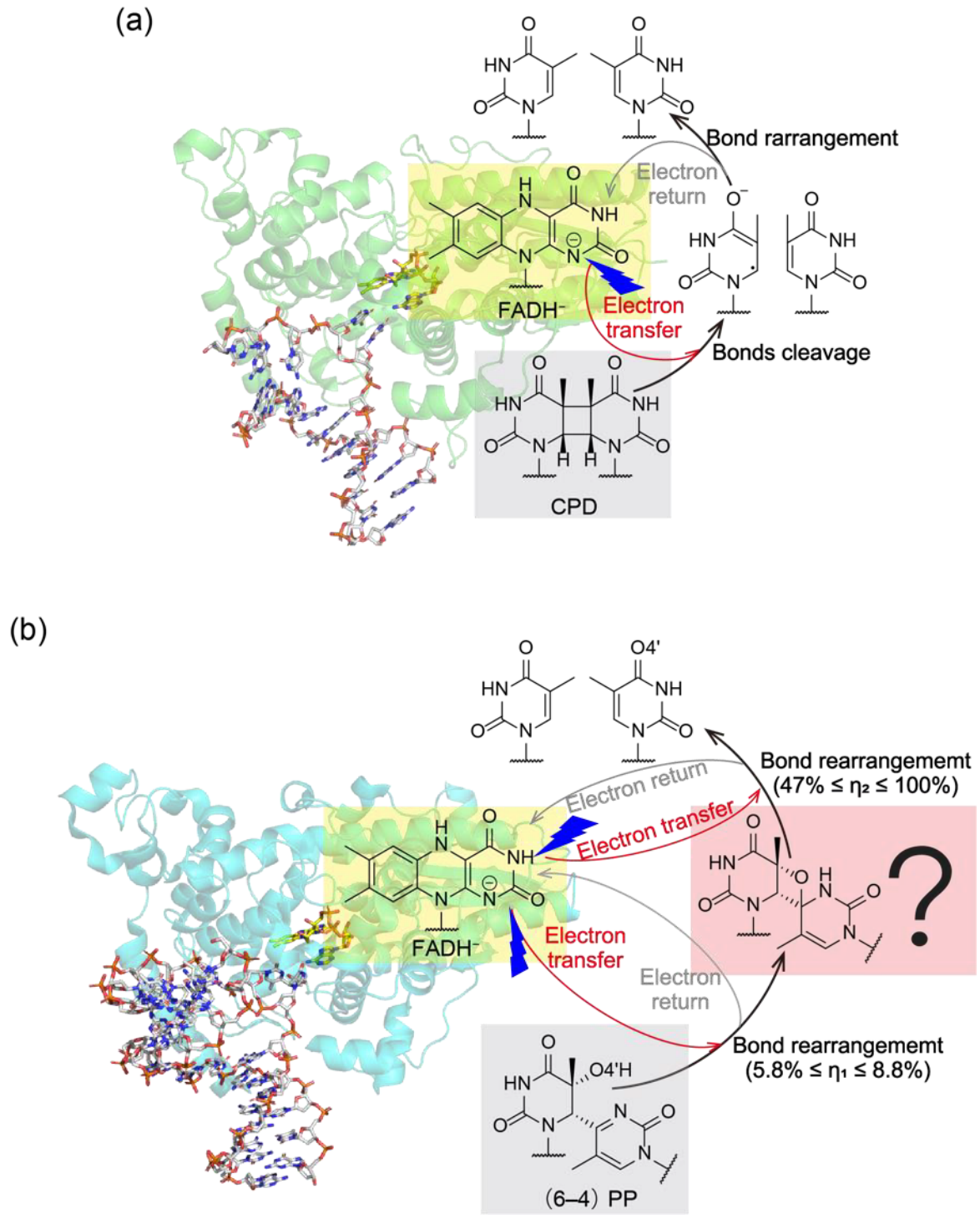

Figure 2. Plausible repair schemes of UV-induced DNA lesions by (a) CPD PLs and (b) (6–4) PLs. The crystal structures of (a) CPD PL from *Anacystis nidulans* (PDB ID: 1TEZ)[30] and (b) (6–4) PL from *Drosophila melanogaster* (PDB ID: 3CVV)[31] shows a structural homology between the two PLs. (a) CPD PL completes the repair of a CPD substrate by a single photoinduced electron transfer from $FADH^-$ to the substrate (red arrow). (b) The repair of a (6–4) PP substrate is proposed to require two-photon reactions. The photoinduced electron transfer steps are indicated with red arrows. The oxetane-bridged dimer is a possible candidate for the intermediate. The calculated quantum yields for the first and second reaction is shown in the scheme as η_1 and η_2.

1.2.2 Light-harvesting energy transfer from an antenna chromophore to FAD in photolyases

PLs often possess an auxiliary chromophore in addition to the catalytic FAD cofactor (Figure 3a). So far, 5,10-methenytetrahydrofolate (MTHF)[32], FAD[33], flavin mononucleotide (FMN)[34], 6,7-dimethyl-8-ribityllumazine (DMRL)[35], and 8-hydroxy-7,8-didemethyl-5-deazariboflavin (8-HDF)[31,36-38] have been found as the second chromophore (Figure 3b). These chromophores emit fluorescence overlapped with the absorption spectra of the $FADH^-$ state and can harvest and transfer the solar energy absorbed by them to the FAD cofactor via Förster resonance energy transfer (FRET) mechanism[39]. The chromophores are therefore called light-harvesting (antenna) chromophores, which allow PLs to efficiently exploit solar energy for the repair reaction. Because successful FRET requires an appropriate relative orientation of an antenna chromophore and FAD, the antenna chromophore should be bound to PLs in a properly regulated manner for the efficient photorepair[40].

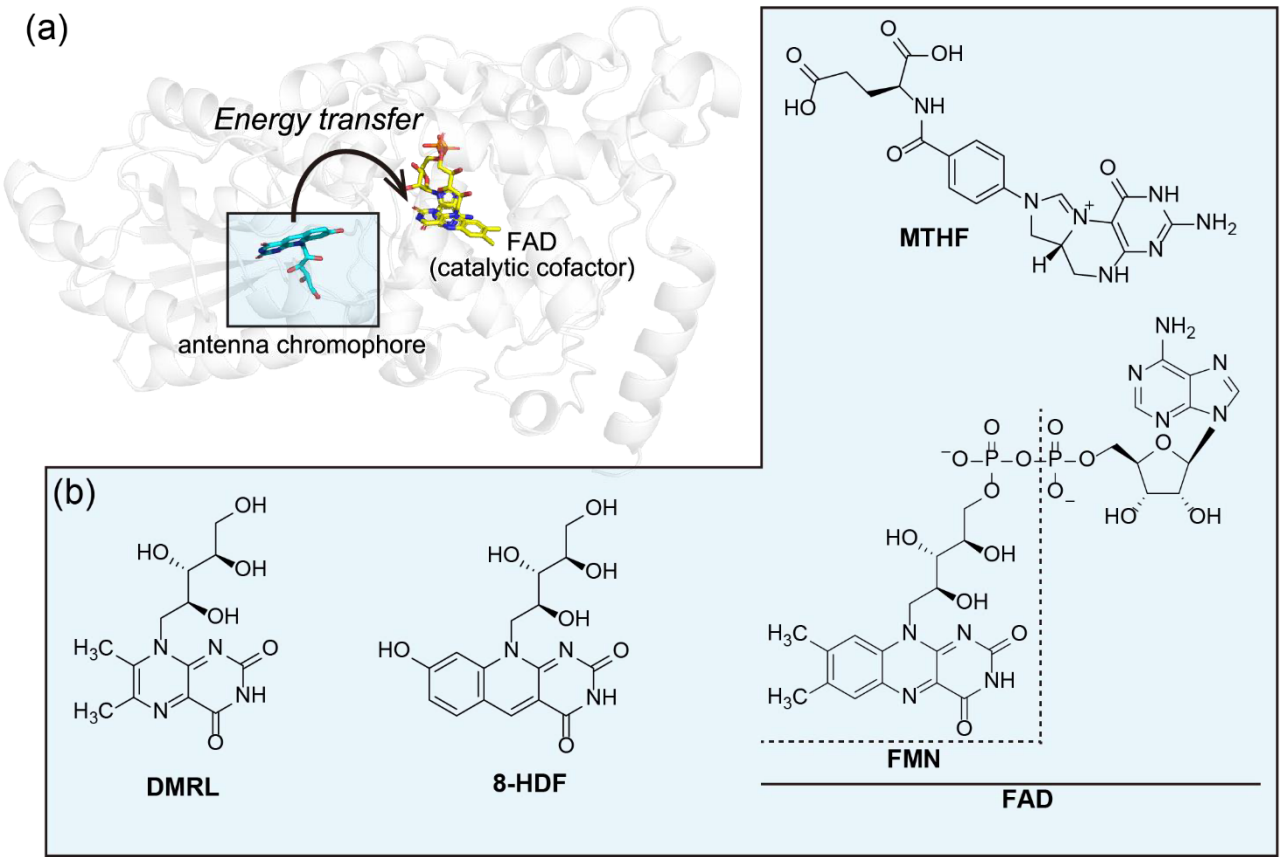

Figure 3. Structural aspects of antenna chromophores in PLs. (a) The crystal structure of CPD PL from *Anacystis nidulans* (PDB ID: 1TEZ)[30] showing the position of antenna chromophore (8-HDF) and FAD in the protein, for the photon energy transfer. (b) The compounds identified as antenna chromophores in PLs.

1.2.3 Activation of FAD in photolyases via a canonical pathway

Photoexcitation of FAD in PLs not only drives the repair reactions but also produces an active state of their FAD cofactor. FAD in PLs can be observed in several redox states, and the resting state in the dark is either the most oxidized state (FAD_{ox}) or the one-electron reduced neutral radical state ($FADH^{\bullet}$)[41,42]. Because $FADH^{-}$ is the exclusive active state for the repair, FAD in the resting states needs to be reduced to $FADH^{-}$. The process for the activation of FAD is accomplished by a highly conserved light-dependent reaction called photoactivation/photoreduction[43]. The photoactivation has attracted great attention because of the interest in the redox regulation of FAD by light reactions. The most canonical photoreduction pathway has been identified through studies on

bacterial CPD PLs. An early transient absorption spectroscopic study on CPD PL from *Escherichia coli* (*Ec*CPD) in 1990 suggested that the reduction of FAD occurs via a photoinduced intraprotein electron transfer from an intrinsic amino acid residue to FAD[44]. The following study identified Trp306 as the residue responsible for the electron transfer[45]. However, the crystal structure of *Ec*CPD revealed that Trp306 is spatially separated from FAD by 15 Å, and two more Trp residues (Trp359 and Trp382) are located between FAD and Trp306, as shown in Figure 4[32]. Further ultrafast transient absorption spectroscopic studies[46-48] and an energetic study[49] demonstrated that Trp359 and Trp382 are also involved in the electron transfer from Trp306 to FAD. A schematic example of the reduction of FAD_{ox} to the one-electron reduced FAD state ($FAD^{\bullet-}$) is summarized in Figure 4. The excited FAD abstracts an electron from Trp382 (annotated as Trp_1H, where H means the hydrogen atom bonded to the nitrogen atom of the indole moiety), and the resultant radical cation of Trp382 ($Trp_1H^{\bullet+}$) subsequently gets an electron from Trp359 (Trp_2H). Finally, Trp306 (Trp_3H) donates an electron to the radical cation of Trp359 ($Trp_2H^{\bullet+}$). These three electron-transferring Trp residues are well conserved among PLs and its relative cryptochromes (see **1.3.1**), and therefore called Trp-triad chain.

While the successive electron transfer yields a ~15 Å charge-separated state ($FAD^{\bullet-}$ $Trp_3H^{\bullet+}$), the charge-separated state is susceptible to charge recombination. Under cellular conditions, deprotonation of $Trp_3H^{\bullet+}$ to $Trp_3^{\bullet}$ by bulk solvent[46] and following quenching of $Trp_3^{\bullet}$ by external reducing agents[50] stabilize the $FAD^{\bullet-}$ state, in competition with charge recombination. The production of $FADH^-$ is accomplished by the second photoreduction of the $FADH^{\bullet}$ state produced by the protonation of $FAD^{\bullet-}$, in the same manner as the first photoreduction of FAD_{ox}[51]. In the canonical

photoreduction process, the electron transfer pathway via the three Trp residues is well established[52], but the protonation pathway is still elusive because of the difficulty in observing a proton transfer. So far, an Asn residue proximal to the N5 atom in FAD (Asn378 in Figure 4a) is known to be responsible for the proton transfer and the kinetic/thermodynamic stability of the $FADH^{\bullet}$ state[53-56].

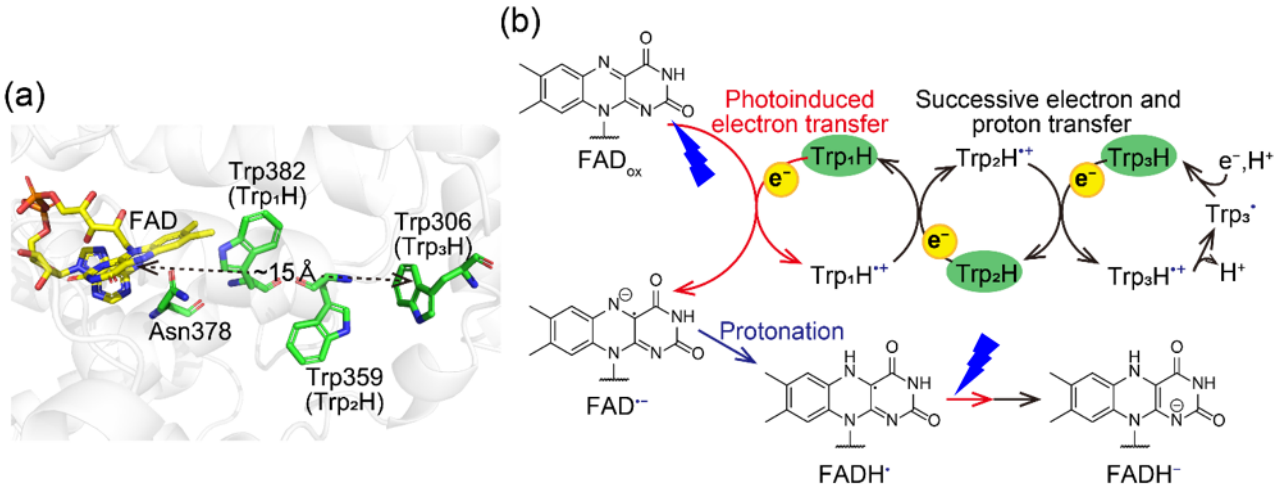

Figure 4. Canonical photoreduction scheme of FAD via three electron-transferring Trp residues. (a) The crystal structure of *Ec*CPD (PDB ID: 1DNP)[32] showing the position of FAD and the amino acid residues involved in photoreduction of FAD. (b) Canonical photoreduction of FAD in PLs composed of photoinduced electron transfer from Trp_1H to FAD (in red arrows) and successive electron and proton transfers from and/or to Trp residues (in black arrows). When the FAD_{ox} is reduced to $FADH^{-}$, $FAD^{\bullet-}$ is protonated to $FADH^{\bullet}$, and $FADH^{\bullet}$ is subjected to the photoreduction.

1.3 Functional diversity of cryptochromes

1.3.1 Cryptochromes evolutionarily related to photolyases

Plants, animals and a handful of other eukaryotes and prokaryotes have proteins evolutionarily related to PLs, which is called cryptochromes (CRYs). PLs and CRYs share a high homology in primary and tertiary structural aspects and form a **P**hotolyase/**C**ryptochrome **S**uper**f**amily (PCSf)[57]. Because PCSf is a large family, they are phylogenetically and functionally

divided into some classes (Table 1). It is interesting that CRYs show various functions based on the class: CRY-DASH is able to repair CPD lesions only in single-stranded DNA[58] (or topologically unusual DNA[59]); plant[60] and animal type I CRYs[61] show photoreceptive signal transduction functions related to circadian rhythms; animal type II CRYs behave as non-photoreceptive transcriptional repressors of genes responsible for the circadian rhythm generation[62]. In addition to the functions, CRY4 is suggested to be responsible for magnetoreception in a light-dependent manner[63].

Table 1. Classification of PCSf.

Class	Proposed Function	Representative Organism
Class I CPD PL	CPD in ssDNA and dsDNA repair	*Escherichia coli*
Class II CPD PL	CPD in ssDNA and dsDNA repair	*Methanosarcina mazei*
Class III CPD PL	CPD in ssDNA and dsDNA repair	*Agrobacterium tumefaciens*
CRY-DASH	CPD in ssDNA repair	*Synechocystis* sp. PCC6803
(6–4) PL	(6–4) PP in ssDNA and dsDNA repair	*Xenopus laevis*
Plant CRY	Photoreceptive signal transduction	*Arabidopsis thaliana*
Animal type I CRY	Photoreceptive signal transduction	*Drosophila melanogaster*
Animal type II CRY	Non-photoreceptive circadian rhythm generation	*Homo sapiens*
CRY4	Photoreceptive magnetoreception	*Erithacus rubecula*

1.3.2 Photoreception by plant CRYs

Plant CRYs are first identified as flavin-based blue light photoreceptor in 1993[64]. Plant CRYs are not a key component of the circadian rhythm regulation in plants, but the transcription of the genes encoding CRYs is controlled to peak in the middle of the day by circadian rhythms[65]. The produced CRYs are activated by blue-light and control numerous events relating to plant growth, such as stimulation of floral initiation[66] and inhibition of hypocotyl elongation[64]. Plant CRYs reportedly convey light signals to their signaling partners represented by CIB1 (cryptochrome-interacting basic-helix-loop-helix)[67], in the form of the homo-oligomers. Although the mechanism of oligomerization remains elusive, light-induced redox state change from FAD_{ox} to $FADH^{\bullet}$ is suggested to trigger the conformational change and homo-oligomerization, which establishes a binding site for the partner proteins[68,69] (Figure 5). Because the reduction of FAD in plant CRYs is also performed in a similar way to that in PLs, photoreduction process plays an essential role in plant CRYs.

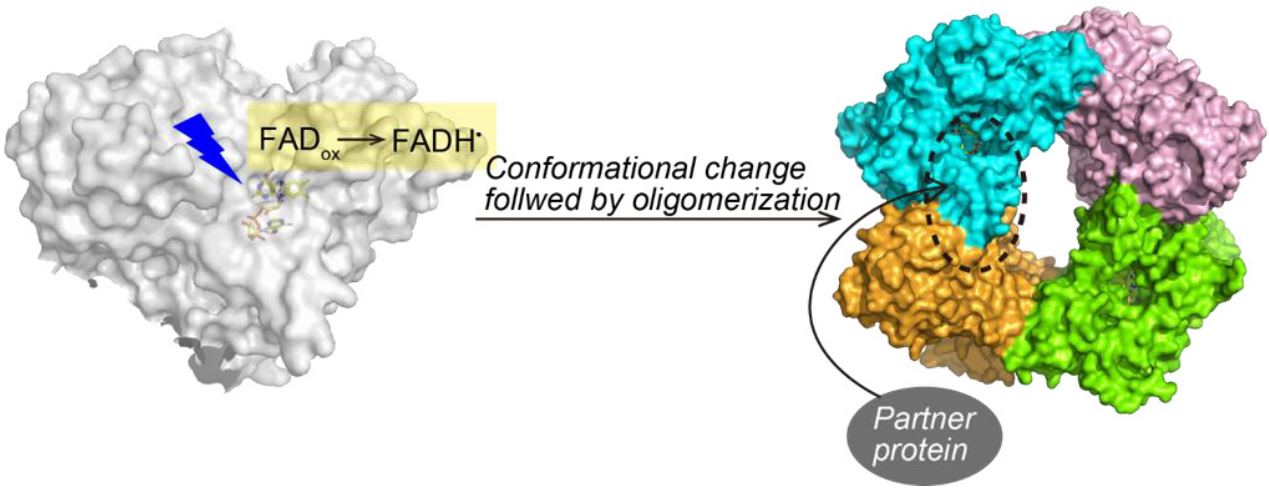

Figure 5. Photoreceptive signal transduction scheme in plant CRYs. The photoreduction of FAD triggers conformational change and oligomerization (dimerization or tetramerization). The tetramer structure is reported for cryptochrome 2 from *Arabidopsis thaliana* (PDB ID: 6X24)[68]. The oligomers interact signaling partner proteins to accomplish the signal transduction.

1.3.3 Photoreception by animal type I CRYs

In addition to plant CRYs, animal type I CRYs are photoreceptive CRYs subjected to many studies. CRY from *Drosophila melanogaster* (*Dm*CRY) is the most characterized animal type I CRY[61]. The function of *Dm*CRY, different from those of the plant CRYs and animal type II CRYs, is to synchronize the circadian rhythm generated by other clock proteins to the external light cycle[70]. In analogy to the signal transduction by plant CRYs, light-induced conformational changes of *Dm*CRY are required to bind target proteins. A report of the crystal structure of full-length *Dm*CRY[71] and the following studies[72-75] have suggested that light-induced undocking of C-terminal region from its binding site would activate *Dm*CRY (Figure 6). The light-activated *Dm*CRY binds to a circadian gene repressor protein called Timeless (TIM)[76] and recruits an E3 ubiquitin ligase named jetlag (JET)[77]. Because JET leads to the degradation of TIM, light stimulus ultimately can reduce the TIM level via *Dm*CRY and JET[77].

Although the most important process in the signal transduction by *Dm*CRY is the light-induced conformational change, researchers have not provided solid explanations for the molecular mechanism how the C-terminal region is undocked from its binding site. A group[73,78] supports the idea that the photoexcitation of FAD produces $FAD^{\bullet-}$, and the radical anion leads to the conformational change (Figure 6). Another[79] claims that the $FAD^{\bullet-}$ should be the biologically resting state under cellular conditions, and the excitation of $FAD^{\bullet-}$ causes a disruption of $FAD^{\bullet-}$ structure and surrounding environment, leading to the conformational change (Figure 6). One of the strategies to identify what factors exactly control the functional expression of *Dm*CRY is to pile up the knowledge on the photoinduced electron dynamics in PCSf proteins.

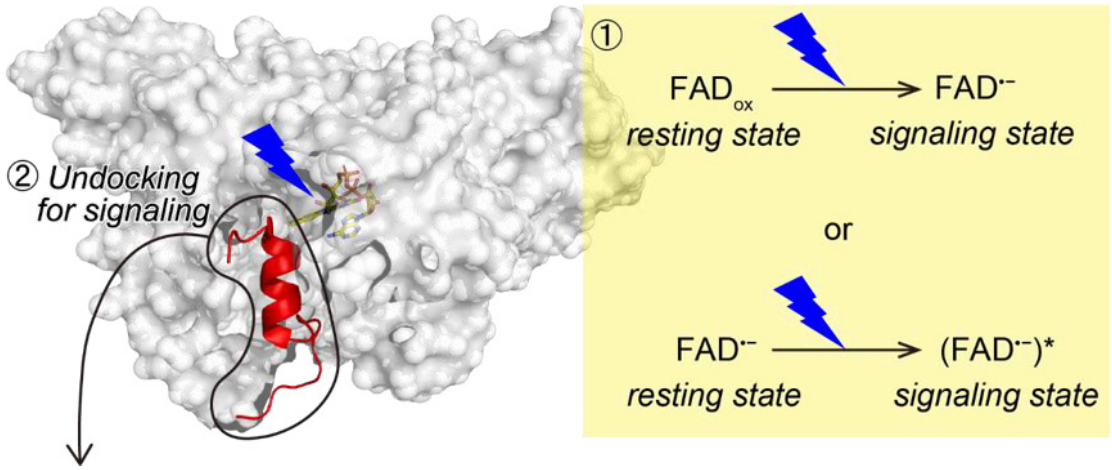

Figure 6. Photoreceptive signal transduction scheme in *Dm*CRY. The $FAD^{\bullet-}$ state produced by photoreduction of FAD_{ox} or the photoexcited $FAD^{\bullet-}$ state ($(FAD^{\bullet-})^*$) is considered to be the signaling state of FAD in *Dm*CRY. The lit state triggers conformational changes and presumably undocks the C-terminal region (in red) from its binding pocket, leading to the interaction with signaling partner proteins.

1.3.4 Rare bifunctional cryptochromes responsible for signal transduction and DNA repair

While many CRYs are involved only in photoreceptive or non-photoreceptive signal transduction as discussed above, bifunctional cryptochromes responsible for not only photoreceptive signal transduction but also the repair of DNA containing (6–4) PPs are found in green algae[36,80,81]. A cryptochrome from *Chlamydomonas reinhardtii* sharing high homology with the animal type CRYs, called *Cr*aCRY, is the representative binfunctional CRY[36]. Although the DNA repair by *Cr*aCRY is considered to be triggered by the electron transfer from the photoexcited $FADH^-$ cofactor to the lesion in the same way as the repair by (6–4) PL[36] (Figure 2), the functional redox state of FAD of CRY remains ambiguous. Beel *et al*.[82] reported that *Cr*aCRY can control the transcription of various genes by responding to both blue and red light *in vivo*. Because $FADH^\bullet$ is the only state that can absorb red light in addition to blue light, their group claimed that the resting state of FAD in *Cr*aCRY would be $FADH^\bullet$, and the signaling state could be the $FADH^-$ state produced by the photoreduction of $FADH^\bullet$. However, to establish the model, the midpoint potentials of the FAD/$FADH^\bullet$ and $FADH^\bullet$/$FADH^-$ couples should be determined, and the resting state of FAD under cellular conditions should be identified.

*Cr*aCRY is believed to undergo structural changes upon illumination and transduce the light signal to partner proteins in a similar way to other photoreceptive CRYs[83]. The structure of *Cr*aCRY is divided into a highly homologous region with PLs and a distinctive C-terminal extension (CTE), and the latter is assumed to be responsible for the structural changes and signal transduction because of the unique amino-acid sequence[36]. However, the structural information on CTE is lacking because

the crystal structure of *Cr*aCRY is available only in the PLs homologous region[36]. To address the possible structural perturbations on CTE upon photoexcitation, Franz-Badur *et al*.[84] performed structural analyses of *Cr*aCRY by hydrogen/deuterium exchange mass spectrometry (HDX-MS). By comparing the deuterium uptakes between the wild type of *Cr*aCRY and the CTE-truncated *Cr*aCRY, they suggested that the CTE can be anchored to the FAD-binding pocket, in both dark (FAD_{ox}) and light ($FADH^{-}$) states. In addition, they compared the uptakes between FAD_{ox} and $FADH^{-}$ states for each *Cr*aCRY variants and suggested that the loops around the residue involved in the photoreduction of FAD are disturbed upon blue light illumination. Tentatively, they proposed that the photoinduced electron transfer along an electron-transferring Trp chain triggered by the photoexcitation of FAD causes the perturbation of the loops, leading to conformational changes in the CTE region (Figure 7). Although the study provided new insights to the dynamics of the *Cr*aCRY structure, the knowledge on photoinduced conformational dynamics coupled by the photoreduction should be demanded to confirm the model, because the measurements were performed for completely equilibrated samples for the dark and light states.

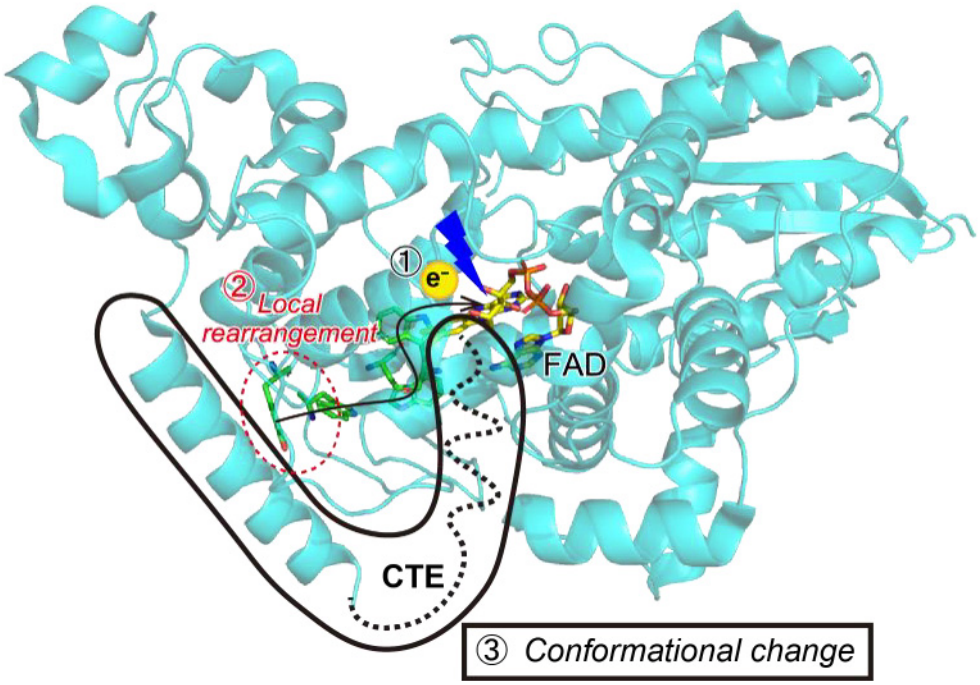

Figure 7. Proposed photoinduced conformational changes in *Cr*aCRY[84]. Photoexcitation of FAD triggers photoreduction of FAD via electron transferring residues (in green) as discussed in ***1.4.5***, leading to the local rearrangement around the region inside the red dashed circle. Then, the conformational changes propagate the CTE region (in black dashed line) along the last α helix.

1.4 Strategies for the productive photoreduction of FAD in PCSf proteins

1.4.1 Solvent-driven photoinduced electron transfer via Trp-triad chain in PLs

Because photoreduction of FAD is the most important process to express various functions of PCSf proteins, organisms should have optimized the proteins to acquire the productive photoreduction ability. For example, *Ec*CPD is demonstrated to perform an efficient photoinduced electron transfer. According to the transient absorption spectroscopic studies of *Ec*CPD in the fs–ps regime, the photoinduced charge separation between $FAD_{ox}/FADH^{\bullet}$ and Trp_3H occurs in a few hundred ps[52] and the back transfer is well repressed with a time constant of >100 ns[52,51,85,86]. As a result, 65% of the charge-separated states can survive over 5 ns[86].

To explore the mechanisms enabling the efficient photoinduced electron transfer, computational methods besides experimental approach are useful. An early electrostatic calculations based on the Poisson–Boltzmann equation confirmed that the successive electron transfer along the Trp-triad chain is a downhill reaction[49]. Considering that Trp_3H is more exposed to solvent than Trp_2H and Trp_1H, and $Trp_3H^{\bullet+}$ could be more stabilized by solvation (Figure 8a), the driving force was tentatively assigned to the stabilization of $Trp_3H^{\bullet+}$ by solvent. In 2011, Woiczikowski *et al*. confirmed the assignment by calculating the free energy difference and solvent reorganization energy between each charge-separated states based on the structures optimized by quantum mechanics/molecular mechanics (QM/MM) simulation[87] (Figure 8b). The sophisticated study demonstrated that the stabilization of $Trp_3H^{\bullet+}$ is more likely caused by solvation rather than protein conformational changes within hundred ps. Although slower protein conformational changes on a ns time scale could occur to stabilize the charge-separated state and repress the charge recombination, evaluation of the effect has not been performed for PLs with the canonical Trp-triad chain.

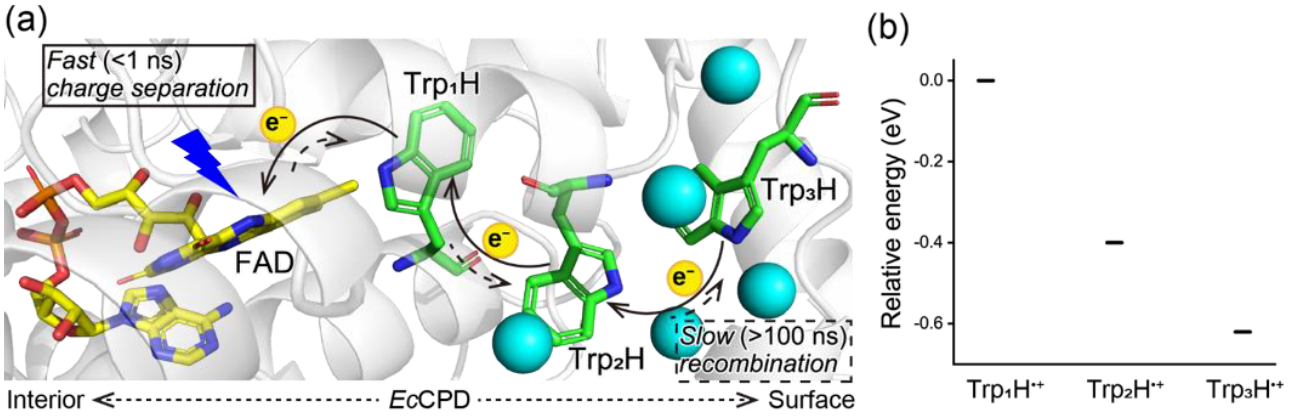

Figure 8. Fast charge separation and slow recombination in photoreduction pathway in *Ec*CPD ensured by solvent. (a) The crystal structure of *Ec*CPD (PDB ID: 1DNP)[32] showing that water molecules (cyan sphere) can more easily access Trp residues on the surface side than in the protein interior. (b) Estimation of the relative energy of the system possessing each radical cation normalized to the system energy of $Trp_1H^{\bullet+}$ state, by free energy calculation based on the structures optimized by QM/MM simulation[87].

1.4.2 Fast protonation of $FAD^{\bullet-}$ for the efficient production of $FADH^{\bullet}$ in plant CRYs

The photoreduction process described for the case of canonical PLs is largely applicable to that of other PCSf proteins. For example, the photoexcitation of FAD_{ox} in plant CRYs also yields the $FAD^{\bullet-}\cdots Trp_3H^{\bullet+}$ charge-separated state as in canonical PLs. However, the produced $FAD^{\bullet-}$ in plant CRYs is more rapidly[88] (~1.5 μs) protonated to $FADH^{\bullet}$ than in other PCSf proteins[86] (typically in an order of ms to s). The proton donor is assigned to be an Asp residue (Asp396 in Figure 9) located proximal to the N5 atom in FAD, according to Fourier transform infrared (FTIR) spectroscopic studies[89,90]. Many studies[88,91] showed that the Asp residue is the key factor to distinguish plant CRYs from PLs, because the Asp residue is substituted for an Asn residue in PLs (Asn378 in Figure 4a). However, a transient absorption measurement of an N378D mutant of *Ec*CPD mimicking plant CRYs showed a formation of an atypical FAD radical in the range of μs, instead of complete protonation of $FAD^{\bullet-}$ to $FADH^{\bullet}$. Considering the observation that the signaling state of FAD in plant CRYs is $FADH^{\bullet}$,

the protonation pathway in plant CRYs should evolutionarily be optimized by acquiring the Asp residue and other undefined factors.

A further ns–μs transient absorption measurement of plant CRY[92] revealed another trick to acquire and stabilize the $FADH^{\bullet}$ state, where ATP binding to plant CRYs up-shifts the pK_a of the Asp residue from 7.4 to >9.0, resulting in the favorable protonation of $FAD^{\bullet-}$ in the wide range of pH. These studies on the Asp residue and the ATP effect show that plant CRYs share the common charge-separated states with PLs but optimize their photoreduction pathway for the formation of $FADH^{\bullet}$.

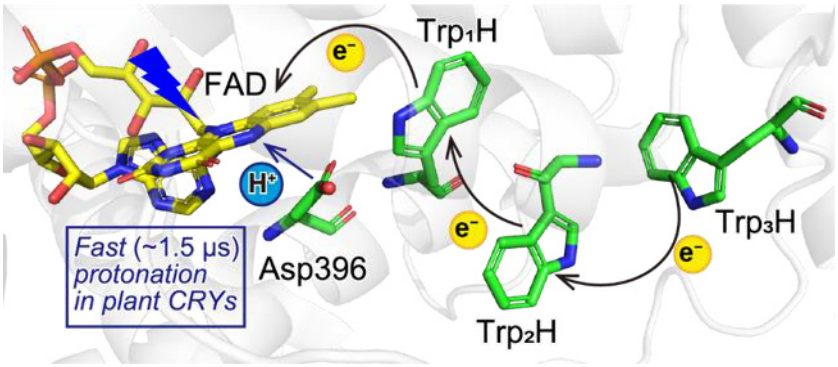

Figure 9. Photoreduction pathway of FAD highlighted in the crystal structure of cryptochrome 1 from *Arabidopsis thaliana* (PDB ID: 1U3D)[93]. Asp396 is involved in the fast protonation of the $FAD^{\bullet-}$ state produced by photoinduced electron transfer through three Trp residues.

1.4.3 Alternative photoinduced electron transfer pathway yielding complex charge-separated states

In contrast to the canonical photoreduction pathway, a rare bacterial class of CPD PL, annotated as class III CPD PL[94], shows a unique structure comprising two possible photoinduced electron transfer pathways[95] (Figure 10). The pathways branch into the canonical Trp-triad pathway (Trp_1H, Trp_2H, Trp_3H) and an alternative pathway composed of Trp_1H and three additional Trp residues (Trp_BH, Trp_CH, Trp_DH in Figure 10a). Mutational analyses of the Trp residues showed that

both of the pathways are involved in the photoreduction of FAD in class III CPD PL[95], suggesting the formation of complex charge-separated states.

A recent simulation[96] of the time-dependent charge propagation in the protein by quantum mechanics/molecular mechanics molecular dynamics (QM/MM MD) illustrated that photoinduced electron transfer firstly occurs along the canonical chain in the similar time region (~ps) to that in the case of canonical PLs, but the back electron transfer from Trp_1H to $Trp_3H^{\bullet+}$ through Trp_2H subsequently occurs unlike the canonical case. Nonetheless, the futile back electron transfer from $FAD^{\bullet-}$ to $Trp_1H^{\bullet+}$ is found to be repressed by the stabilization of $FAD^{\bullet-}$ due to the reorganization of the surrounding residues during the electron transfer along the canonical chain (a few hundred ps). After all, $Trp_1H^{\bullet+}$ was reduced by a successive electron transfer via the alternative chain, which produces a thermodynamically stabilized $Trp_DH^{\bullet+}$ radical cation. These studies[96] suggest that class III CPD PL is optimized to use both the kinetically favored canonical pathway and the thermodynamically favored alternative pathway for their productive photoreduction. The above mechanism is summarized in Figure 10b, though the scheme has not been confirmed by transient absorption data for class III CPD PL.

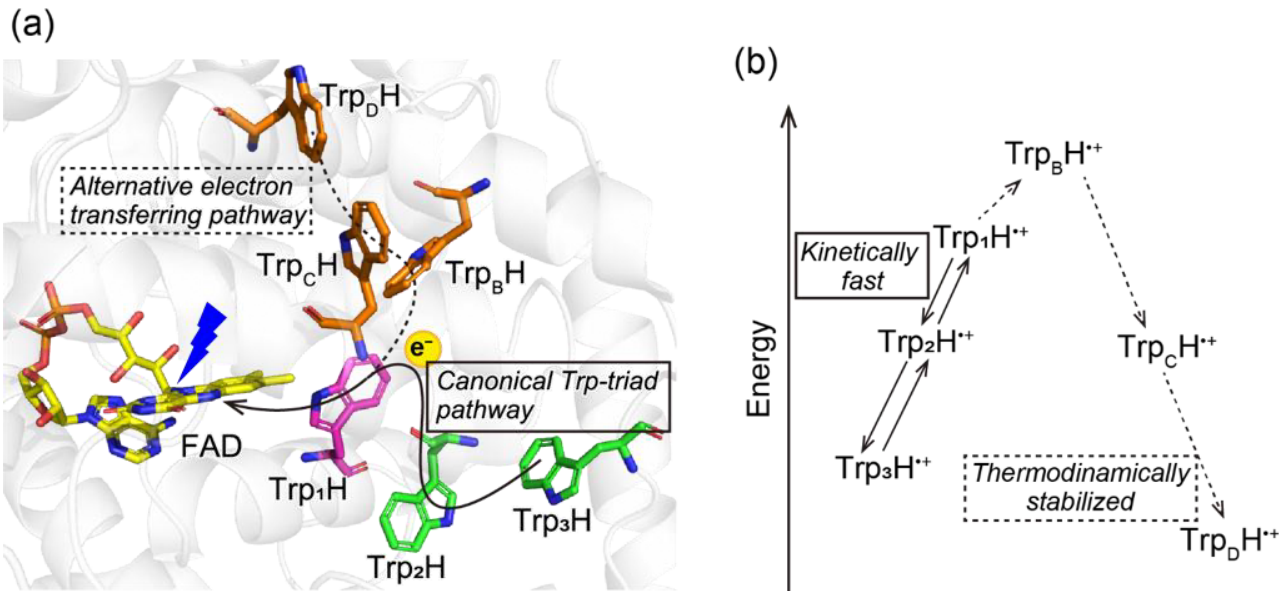

Figure 10. Plausible photoreduction pathway in class III CPD PLs. (a) The crystal structure of class III CPD PL from *Agrobacterium tumefaciens* (PDB ID: 4U63)[94] suggesting the possibility that six Trp residues are involved in the photoinduced electron transfer to FAD. (b) Energetic estimation of each system possessing an indicated radical cation. The canonical Trp triad pathway is kinetically favored, but the alternative electron transferring pathway is thermodynamically favored[96].

1.4.4 Extended electron transfer pathway in animal (6–4) PLs and CRYs

While the branching electron transfer pathway in class III CPD PL has not been fully characterized, another electron transfer pathway distinct from canonical Trp-triad chain is enthusiastically studied. The pathway is composed of the canonical three Trp residues in addition to one or two Trp or Tyr residues, which does not branch off from the canonical chain but extends the chain, and therefore is called an extended electron transfer pathway. In 2015, Müller *et al*. discovered that the accessory fourth Trp (Trp_4H in Figure 11) plays a key role in the photoinduced electron transfer to FAD in (6–4) PL from *Xenopus laevis* (*Xl*64) and is highly conserved in animal (6–4) PLs and cryptochromes[97]. The ns–μs transient absorption measurement of the photoinduced electron transfer in *Xl*64 showed that (i) Trp_4H reduces $Trp_3H^{\bullet+}$ within 20 ns, (ii) the resultant $Trp_4H^{\bullet+}$ is

deprotonated in 2.5 μs, and (iii) the extremely long-lived (40 ms) $FAD^{\bullet-}\cdots Trp_4^{\bullet}$ radical pair is produced. Because the mutation of Trp_4H by a non-reducible Phe residue (W370F) accelerates the charge recombination between $FAD^{\bullet-}$ and $Trp^{\bullet}$ radical pair by 4000-fold, the stabilized radical pair in *Xl*64 cannot be formed without the presence of Trp_4H. Furthermore, the following energetic study of the photoinduced electron transfer in *Xl*64 by QM/MM calculation confirmed that the successive electron transfer via the four Trp residues is downhill[98]. These results suggest that the elongated distance between FAD and final electron-donating Trp residue by Trp_4H (20 Å for the distance between FAD and Trp_4H *vs.* 15 Å for the distance between FAD and Trp_3H) represses the charge recombination among the photoinduced charge separated states efficiently. Furthermore, Yamamoto *et al*. revealed that Trp_4H in *Xl*64 is essential for not only its photoreduction ability but also its (6–4) PP repairing activity *in vivo*[42]. The study is surprising, because the photoreduction pathway lacking Trp_4H in *Xl*64 seems to be structurally equivalent to the canonical Trp-triad chain, but is found to be functionally inactive. However, these studies did not give any molecular explanations for the mysterious findings.

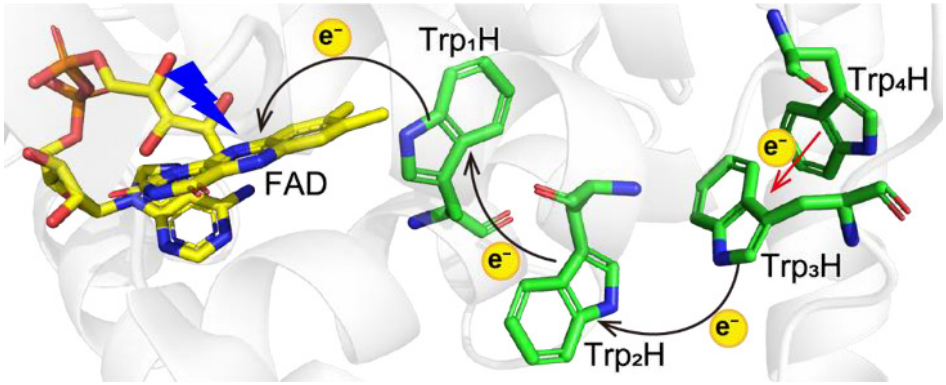

Figure 11. Extended photoinduced electron transfer pathway in animal (6–4) PLs. The crystal structure of (6–4) PL from *Drosophila melanogaster* highly homologous to *Xl*64 (PDB ID: 3CVU)[26] shows that animal (6–4) PLs have a fourth electron transferring Trp residue (Trp_4H).

In addition to the benefit of the extended chain for FAD photoreduction ability in (6–4) PLs, the chain attracts great attention because of its magnetic sensitivity of animal CRYs. Since the first proposal for the possible involvement of CRYs in the detection of Earth's magnetic field in 2000[99], the molecular origin of their magnetoreception has been discussed. One of the most discussed mechanisms sensing magnetic field is called radical pair mechanism (RPM). RPM is based on the observation that an external magnetic field affects distribution of spin states of photoinduced radical pairs, and different spin states can be discriminated by different recombination rates. Because CRYs can produce the photoinduced radical pairs between FAD and Trp residues and maintain the pairs on a relatively long time scale sufficient for the signal transduction, they have been suggested as one of the most promising candidate for proteins exerting RPM[100-102]. Recent comprehensive analyses of radical pairs in CRY4 from a migratory bird (*Erithacus rubecula*), by UV/vis and electron paramagnetic resonance spectroscopy combined with spin dynamics simulation, revealed that the presence of Trp_4H is essential in sensing magnetic field as weak as the Earth's magnetic field[63].

1.4.5 Inhibition of charge-recombination by fast deprotonation of electron donating residues

*Cr*aCRY, a bifunctional animal type CRY, has an extra Tyr residue[36,103] (annotated as TyrOH373, where OH means the phenolic hydroxyl group) instead of Trp_4H. In analogy to Trp_4H, TyrOH373 is shown to participate in the photoinduced electron transfer[104] (Figure 12a) and to donate an electron to $Trp_3H^{\bullet+}$ by the fs–ns transient absorption measurements of the wild type and a Y373F mutant[106]. In contrast to Trp_4H, the oxidized Tyr is rapidly deprotonated to $TyrO^{\bullet}373$ via proton-coupled electron transfer in 800 ps, without any significant kinetic isotope effect nor a pH effect between pH 6.5 and 9.0[105]. The proton acceptor was strongly suggested to be Asp321 because of its close contact with TyrOH373 (3.0 Å) and a low p*K*a value of an Asp residue (p*K*a = 3.9 in aqueous solution). The ultrafast deprotonation is a good choice to suppress the nonproductive charge recombination, and the $FAD^{\bullet-}\cdots TyrO^{\bullet}373$ radical pair is formed with a higher quantum yield than the $FAD^{\bullet-}\cdots Trp_4^{\bullet}$ radical pair in *Xl*64 (~50% for *Cr*aCRY *vs.* ~25% for *Xl*64)[97,105].

Another prominent example of ultrafast deprotonation of electron donating residues occurs in *Methanosarcina mazei* class II CPD PL (*Mm*CPDII). The crystal structure of *Mm*CPDII shows that *Mm*CPDII does not retain the canonical Trp-triad chain but another chain composed of three Trp residues and a fourth Tyr residue[106]. The alternative chain plays a similar role in the photoreduction of FAD to that of the canonical chain[106], and photoinduced electron transfer takes place along the chain[107]. A fraction of the third tryptophan radical cation ($Trp_CH^{\bullet+}$) produced via the successive electron transfer in 200 ps is subjected to the reduction from Tyr (~30%), but major subset of $Trp_CH^{\bullet+}$ is mainly deprotonated in ~400 ps[107]. Because the ultrafast deprotonation shows a kinetic isotope

effect (~800 ps in a D_2O buffer), a well-coordinated water cluster around Trp_CH is suggested to mediate the deprotonation (Figure 12b).

These results show that surroundings of the distal radical cations accelerate the deprotonation to cancel futile recombination, leading to productive photoreduction of FAD in *Cr*aCRY and *Mm*CPDII.

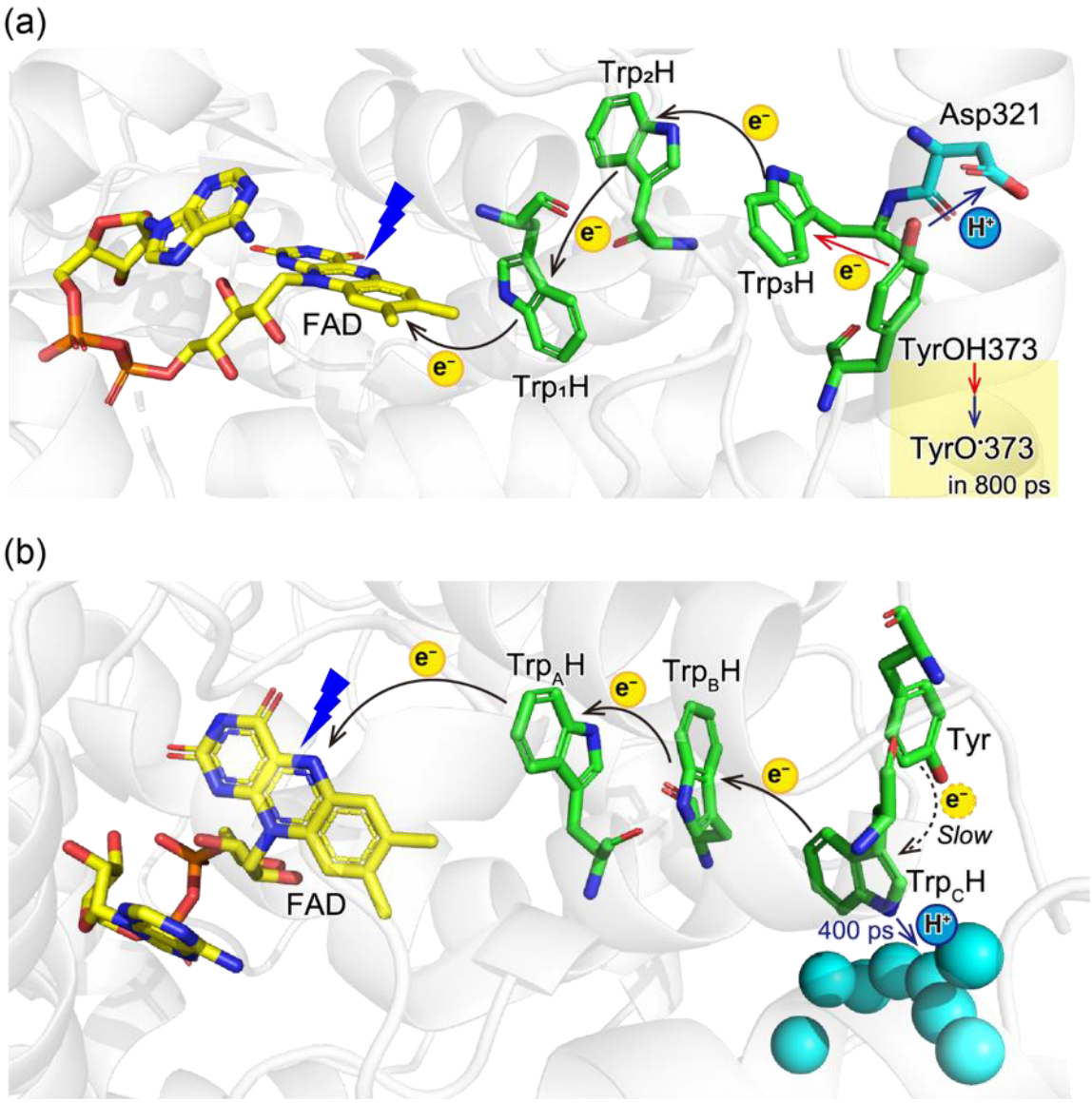

Figure 12. Fast deprotonation of electron donating residues for efficient photoreduction of FAD in (a) *Cr*aCRY and (b) class II CPD PLs. (a) The crystal structure of *Cr*aCRY (PDB ID: 6FN3)[36] showing a photoinduced electron transfer pathway composed of the canonical three Trp residues and an additional Tyr residue (TyrOH373). TyrOH373 is rapidly oxidized via proton-coupled electron transfer modulated by Asp321 (800 ps). (b) The crystal structure of *Mm*CPDII (PDB ID: 2XRZ)[106] showing an uncommon electron transferring Trp residues and an auxiliary Tyr residue. The Trp residues are annotated as Trp_AH, Trp_BH, and Trp_CH to distinguish them from the canonical Trp chain (Trp_1H, Trp_2H, and Trp_3H). The radical cation on Trp_CH produced by the photoinduced electron transfer is more often subjected to the fast deprotonation by a water cluster than the slow reduction by the Tyr residue. Müller *et al*. referred eight water molecules observed in the crystal structure (shown in cyan sphere) as the member of the water cluster[107].

1.5 Background and outline of this thesis

Photolyase/**C**ryptochrome **S**uper**f**amily (PCSf) is an evolutionarily old photoreceptor protein family present in all kingdoms of life and expresses a variety of indispensable functions, such as repair of UV-damaged DNA by PLs and circadian rhythm regulation by CRYs. In spite of the functional diversity, PCSf proteins share a part of the pathway to activate themselves, in which FAD is reduced to active redox states by absorbing photon energy. In the process called photoactivation/photoreduction, FAD gets an electron from a nearby Trp residue, and a successive electron transfer along an intraprotein Trp chain composed of the canonical three Trp residues lets the cation on the Trp residue go away and represses the futile backward electron transfer, stabilizing the reduced FAD state. A recent report that the presence of a fourth Trp residue (Trp_4H) in animal (6–4) PLs and CRYs yields a long-lived charge-separated state has attracted great attention, because the trick to inhibit the charge recombination between FAD and Trp residues is suggested to be directly involved in signal transductions by CRYs.

On the other hand, the surprising findings of the functionally essential Trp_4H in animal (6–4) PLs give rise a question how plant (6–4) PLs, which utilize the canonical three Trp residues, can accomplish the same function with animal (6–4) PLs. In this thesis, I tried to disclose an undefined mechanism allowing plant (6–4) PLs to perform the productive photoinduced electron transfer and photoreduction of FAD. This thesis should not only reveal a strategy which the natural system has found out for the efficient photoreaction in the process of evolution, but also provide a new suggestion for photoinduced conformational changes in (6–4) PLs and CRYs.

Chapter 2. I focused on an effect of a water molecule on photoreduction of FAD in plant *Arabidopsis thaliana* (6–4) PL (*At*64). The water molecule is located proximal to the terminal electron transferring Trp residue (Trp_3H) in the reported crystal structure of *At*64. Molecular dynamics simulations indicated that the water is stably captured in a fixed orientation, while a mutation of Ser412 disturbs the orientation and causes the water displacement from the binding site. Steady-state photoreduction kinetics measurements and a functional assay revealed that the mutation impaired the photoreduction ability *in vitro* and *in vivo*. The combination of computational and experimental analyses suggested that the water molecule plays a key role in the photoreduction of FAD in plant (6–4) PLs, presumably due to its involvement in the stabilization of the photoinduced charge separated states between FAD and Trp_3H.

Chapter 3. In the previous chapter, I discovered that a water molecule close to Trp_3H is required for the efficient photoreduction in plant (6–4) PLs, but the mechanism enabling the water to participate in the reaction was not fully identified. In this chapter, I found that a regulated solvation of Trp_3H yields an extraordinarily long-lived charge-separated state for the productive photoreduction. I focused on a clearly different residue neighboring Trp_3H between plant (6–4) PLs and animal (6–4) PLs (His and Ser are strongly conserved in plant and animal (6–4) PLs, respectively.). Molecular dynamics simulation showed that mutations of the His residue alters accessibility of the bulk solvent to Trp_3H. Steady-state and time-resolved spectroscopy revealed that the disturbed solvation of Trp_3H

by the mutations impairs photoreduction ability by affecting lifetimes of the photoinduced charge-separated states between FAD and Trp_3H. I discovered that the surprisingly regulated solvation of Trp_3H including the water molecule discussed in the previous chapter enables plant (6–4) PLs to perform the efficient photoreduction. The newly identified mechanisms will expand the arsenal of tricks employed by PCSf proteins to achieve efficient photoreduction.

Chapter 4. In Chapters 2 and 3, I discovered the distinctive mechanisms allowing plant (6–4) photolyases to stabilize photoinduced charge-separated states for the productive photoreduction. In Chapter 4, I tried to uncover a common factor regulating FAD photoreduction in a wide range of PCSf proteins by shedding light on their conformational changes accompanied by FAD photoreduction. Hydrogen/deuterium exchange mass spectrometry (HDX-MS) measurement of *At*64 revealed small but significant conformational changes upon the photoreduction. The detailed movement of residues was investigated by an electrochemical measurement of a mutant, in which a residue concerning the conformational changes is replaced to block the rearrangements. Finally, steady-state photoreduction kinetics for the mutant and an additional mutant suggested that conformational changes in two helices modulate the photoreduction ability of *At*64. Because the key residues to exert the changes are strongly conserved among other (6–4) PLs and animal cryptochromes, the proposed mechanism could provide a new insight into photoinduced conformational changes in various PCSf proteins.

Reference

1. Tashiro, T., Ishida, A., Hori, M., Igisu, M., Koike, M., Mejean, P., Takahata, N., Sano, Y. & Komiya, T., Early trace of life from 3.95 Ga sedimentary rocks in Labrador, Canada. *Nature* **549**, 516–518 (2017).
2. Brocks, J. J., Logan, G. A., Buick, R. & Summons, R. E., Archean molecular fossils and the early rise of eukaryotes. *Science* **285**, 1033–1036 (1999).
3. Lyons, T. W., Reinhard, C. T. & Planavsky, N. J., The rise of oxygen in Earth's early ocean and atmosphere. *Nature* **506**, 307–315 (2014).
4. Schmidt-Rohr, K., Oxygen is the high-energy molecule powering complex multicellular life: fundamental corrections to traditional bioenergetics. *ACS Omega* **5**, 2221–2233 (2020).
5. Palczewski, K., G protein-coupled receptor rhodopsin. *Annu. Rev. Biochem.* **75**, 743–767 (2006).
6. Wright, K. P., Jr., McHill, A. W., Birks, B. R., Griffin, B. R., Rusterholz, T. & Chinoy, E. D., Entrainment of the human circadian clock to the natural light-dark cycle. *Curr. Biol.* **23**, 1554–1558 (2013).
7. Jans, J., Schul, W., Sert, Y. G., Rijksen, Y., Rebel, H., Eker, A. P., Nakajima, S., van Steeg, H., de Gruijl, F. R., Yasui, A., Hoeijmakers, J. H. & van der Horst, G. T., Powerful skin cancer protection by a CPD-photolyase transgene. *Curr. Biol.* **15**, 105–115 (2005).
8. Varghese, A. J. & Wang, S. Y., Thymine-thymine adduct as a photoproduct of thymine. *Science* **160**, 186–187 (1968).
9. You, Y. H., Lee, D. H., Yoon, J. H., Nakajima, S., Yasui, A. & Pfeifer, G. P., Cyclobutane pyrimidine dimers are responsible for the vast majority of mutations induced by UVB irradiation in mammalian cells. *J. Biol. Chem.* **276**, 44688–44694 (2001).
10. Lo, H. L., Nakajima, S., Ma, L., Walter, B., Yasui, A., Ethell, D. W. & Owen, L. B., Differential biologic effects of CPD and 6–4PP UV-induced DNA damage on the induction of apoptosis and cell-cycle arrest. *BMC Cancer* **5**, 135 (2005).
11. DiGiovanna, J. J. & Kraemer, K. H., Shining a light on xeroderma pigmentosum. *J. Invest. Dermatol.* **132**, 785–796 (2012).
12. Taghdiri, M., Dastsooz, H., Fardaei, M., Mohammadi, S., Farazi Fard, M. A. & Faghihi, M. A., A novel mutation in ERCC8 gene causing cockayne syndrome. *Front. Pediatr.* **5**, 169 (2017).
13. Faghri, S., Tamura, D., Kraemer, K. H. & Digiovanna, J. J., Trichothiodystrophy: a systematic review of 112 published cases characterises a wide spectrum of clinical manifestations. *J. Med. Genet.* **45**, 609–621 (2008).
14. de Boer, J. & Hoeijmakers, J. H., Nucleotide excision repair and human syndromes. *Carcinogenesis* **21**, 453–460 (2000).
15. Sancar, A., Structure and function of DNA photolyase and cryptochrome blue-light photoreceptors. *Chem. Rev.* **103**, 2203–2237 (2003).

16. Kelner, A., Effect of visible light on the recovery of streptomyces griseus conidia from ultraviolet irradiation injury. *Proc. Natl. Acad. Sci. USA* **35**, 73–79 (1949).
17. Dulbecco, R., Reactivation of ulatra-violet-inactivated bacteriophage by visible light. *Nature* **163**, 949–950 (1949).
18. Rupert, C. S., Photoenzymatic repair of ultraviolet damage in DNA. II. Formation of an enzyme-substrate complex. *J. Gen. Physiol.* **45**, 725–741 (1962).
19. Sancar, A. & Rupert, C. S., Cloning of the phr gene and amplification of photolyase in *Escherichia coli*. *Gene* **4**, 295–308 (1978).
20. Sancar, A. & Sancar, G. B., *Escherichia coli* DNA photolyase is a flavoprotein. *J. Mol. Biol.* **172**, 223–227 (1984).
21. Todo, T., Takemori, H., Ryo, H., Ihara, M., Matsunaga, T., Nikaido, O., Sato, K. & Nomura, T., A new photoreactivating enzyme that specifically repairs ultraviolet light-induced (6–4)photoproducts. *Nature* **361**, 371–374 (1993).
22. Marizcurrena, J. J., Acosta, S., Canclini, L., Hernandez, P., Valles, D., Lamparter, T. & Castro-Sowinski, S., A natural occurring bifunctional CPD/(6–4)-photolyase from the Antarctic bacterium *Sphingomonas* sp. UV9. *Appl. Microbiol. Biotechnol.* **104**, 7037–7050 (2020).
23. Liu, Z., Tan, C., Guo, X., Kao, Y. T., Li, J., Wang, L., Sancar, A. & Zhong, D., Dynamics and mechanism of cyclobutane pyrimidine dimer repair by DNA photolyase. *Proc. Natl. Acad. Sci. USA* **108**, 14831–14836 (2011).
24. Hitomi, K., Nakamura, H., Kim, S. T., Mizukoshi, T., Ishikawa, T., Iwai, S. & Todo, T., Role of two histidines in the (6–4) photolyase reaction. *J. Biol. Chem.* **276**, 10103–10109 (2001).
25. Li, J., Liu, Z., Tan, C., Guo, X., Wang, L., Sancar, A. & Zhong, D., Dynamics and mechanism of repair of ultraviolet-induced (6–4) photoproduct by photolyase. *Nature* **466**, 887–890 (2010).
26. Maul, M. J., Barends, T. R., Glas, A. F., Cryle, M. J., Domratcheva, T., Schneider, S., Schlichting, I. & Carell, T., Crystal structure and mechanism of a DNA (6–4) photolyase. *Angew. Chem. Int. Ed.* **47**, 10076–10080 (2008).
27. Sadeghian, K., Bocola, M., Merz, T. & Schutz, M., Theoretical study on the repair mechanism of the (6–4) photolesion by the (6–4) photolyase. *J. Am. Chem. Soc.* **132**, 16285–16295 (2010).
28. Yamamoto, J., Martin, R., Iwai, S., Plaza, P. & Brettel, K., Repair of the (6–4) photoproduct by DNA photolyase requires two photons. *Angew. Chem. Int. Ed.* **52**, 7432–7436 (2013).
29. Thiagarajan, V., Villette, S., Espagne, A., Eker, A. P., Brettel, K. & Byrdin, M., DNA repair by photolyase: a novel substrate with low background absorption around 265 nm for transient absorption studies in the UV. *Biochemistry* **49**, 297–303 (2010).
30. Mees, A., Klar, T., Gnau, P., Hennecke, U., Eker, A. P., Carell, T. & Essen, L. O., Crystal structure of a photolyase bound to a CPD-like DNA lesion after in situ repair. *Science* **306**, 1789–1793 (2004).

31. Glas, A. F., Maul, M. J., Cryle, M., Barends, T. R., Schneider, S., Kaya, E., Schlichting, I. & Carell, T., The archaeal cofactor F0 is a light-harvesting antenna chromophore in eukaryotes. *Proc. Natl. Acad. Sci. USA* **106**, 11540–11545 (2009).
32. Park, H. W., Kim, S. T., Sancar, A. & Deisenhofer, J., Crystal structure of DNA photolyase from *Escherichia coli*. *Science* **268**, 1866–1872 (1995).
33. Fujihashi, M., Numoto, N., Kobayashi, Y., Mizushima, A., Tsujimura, M., Nakamura, A., Kawarabayasi, Y. & Miki, K., Crystal structure of archaeal photolyase from *Sulfolobus tokodaii* with two FAD molecules: implication of a novel light-harvesting cofactor. *J. Mol. Biol.* **365**, 903–910 (2007).
34. Ueda, T., Kato, A., Kuramitsu, S., Terasawa, H. & Shimada, I., Identification and characterization of a second chromophore of DNA photolyase from *Thermus thermophilus* HB27. *J. Biol. Chem.* **280**, 36237–36243 (2005).
35. Zhang, F., Scheerer, P., Oberpichler, I., Lamparter, T. & Krauss, N., Crystal structure of a prokaryotic (6–4) photolyase with an Fe-S cluster and a 6,7-dimethyl-8-ribityllumazine antenna chromophore. *Proc. Natl. Acad. Sci. USA* **110**, 7217–7222 (2013).
36. Franz, S., Ignatz, E., Wenzel, S., Zielosko, H., Putu, E., Maestre-Reyna, M., Tsai, M. D., Yamamoto, J., Mittag, M. & Essen, L. O., Structure of the bifunctional cryptochrome aCRY from *Chlamydomonas reinhardtii*. *Nucleic Acids Res.* **46**, 8010–8022 (2018).
37. Kiontke, S., Gnau, P., Haselsberger, R., Batschauer, A. & Essen, L. O., Structural and evolutionary aspects of antenna chromophore usage by class II photolyases. *J. Biol. Chem.* **289**, 19659–19669 (2014).
38. Eker, A. P., Kooiman, P., Hessels, J. K. & Yasui, A., DNA photoreactivating enzyme from the cyanobacterium *Anacystis nidulans*. *J. Biol. Chem.* **265**, 8009–8015 (1990).
39. Tan, C., Guo, L., Ai, Y., Li, J., Wang, L., Sancar, A., Luo, Y. & Zhong, D., Direct determination of resonance energy transfer in photolyase: structural alignment for the functional state. *J. Phys. Chem. A* **118**, 10522–10530 (2014).
40. Morimoto, A., Hosokawa, Y., Miyamoto, H., Verma, R. K., Iwai, S., Sato, R. & Yamamoto, J., Key interactions with deazariboflavin cofactor for light-driven energy transfer in *Xenopus* (6–4) photolyase. *Photochem. Photobiol. Sci.* **20**, 875–887 (2021).
41. Li, J., Uchida, T., Ohta, T., Todo, T. & Kitagawa, T., Characteristic structure and environment in FAD cofactor of (6–4) photolyase along function revealed by resonance Raman spectroscopy. *J. Phys. Chem. B* **110**, 16724–16732 (2006).
42. Yamamoto, J., Shimizu, K., Kanda, T., Hosokawa, Y., Iwai, S., Plaza, P. & Müller, P., Loss of fourth electron-transferring tryptophan in animal (6–4) photolyase impairs DNA repair activity in bacterial cells. *Biochemistry* **56**, 5356–5364 (2017).
43. Byrdin, M., Sartor, V., Eker, A. P., Vos, M. H., Aubert, C., Brettel, K. & Mathis, P., Intraprotein electron transfer and proton dynamics during photoactivation of DNA photolyase from *E. coli*: review and new insights from an "inverse" deuterium isotope effect. *Biochim. Biophys. Acta* **1655**, 64–70 (2004).

44. Heelis, P. F., Okamura, T. & Sancar, A., Excited-state properties of *Escherichia coli* DNA photolyase in the picosecond to millisecond time scale. *Biochemistry* **29**, 5694–5698 (1990).
45. Li, Y. F., Heelis, P. F. & Sancar, A., Active site of DNA photolyase: tryptophan-306 is the intrinsic hydrogen atom donor essential for flavin radical photoreduction and DNA repair in vitro. *Biochemistry* **30**, 6322–6329 (1991).
46. Aubert, C., Vos, M. H., Mathis, P., Eker, A. P. & Brettel, K., Intraprotein radical transfer during photoactivation of DNA photolyase. *Nature* **405**, 586–590 (2000).
47. Byrdin, M., Eker, A. P., Vos, M. H. & Brettel, K., Dissection of the triple tryptophan electron transfer chain in *Escherichia coli* DNA photolyase: Trp382 is the primary donor in photoactivation. *Proc. Natl. Acad. Sci. USA* **100**, 8676–8681 (2003).
48. Byrdin, M., Villette, S., Eker, A. P. & Brettel, K., Observation of an intermediate tryptophanyl radical in W306F mutant DNA photolyase from *Escherichia coli* supports electron hopping along the triple tryptophan chain. *Biochemistry* **46**, 10072–10077 (2007).
49. Popovic, D. M., Zmiric, A., Zaric, S. D. & Knapp, E. W., Energetics of radical transfer in DNA photolyase. *J. Am. Chem. Soc.* **124**, 3775–3782 (2002).
50. Heelis, P. F., Payne, G. & Sancar, A., Photochemical properties of *Escherichia coli* DNA photolyase: selective photodecomposition of the second chromophore. *Biochemistry* **26**, 4634–4640 (1987).
51. Liu, Z., Tan, C., Guo, X., Li, J., Wang, L. & Zhong, D., Dynamic determination of active-Site reactivity in semiquinone photolyase by the cofactor photoreduction. *J. Phys. Chem. Lett.* **5**, 820–825 (2014).
52. Liu, Z., Tan, C., Guo, X., Li, J., Wang, L., Sancar, A. & Zhong, D., Determining complete electron flow in the cofactor photoreduction of oxidized photolyase. *Proc. Natl. Acad. Sci. USA* **110**, 12966–12971 (2013).
53. Xu, L., Mu, W., Ding, Y., Luo, Z., Han, Q., Bi, F., Wang, Y. & Song, Q., Active site of *Escherichia coli* DNA photolyase: Asn378 is crucial both for stabilizing the neutral flavin radical cofactor and for DNA repair. *Biochemistry* **47**, 8736–8743 (2008).
54. Balland, V., Byrdin, M., Eker, A. P., Ahmad, M. & Brettel, K., What makes the difference between a cryptochrome and DNA photolyase? A spectroelectrochemical comparison of the flavin redox transitions. *J. Am. Chem. Soc.* **131**, 426–427 (2009).
55. Damiani, M. J., Yalloway, G. N., Lu, J., McLeod, N. R. & O'Neill, M. A., Kinetic stability of the flavin semiquinone in photolyase and cryptochrome-DASH. *Biochemistry* **48**, 11399–11411 (2009).
56. Damiani, M. J., Nostedt, J. J. & O'Neill, M. A., Impact of the N5-proximal Asn on the thermodynamic and kinetic stability of the semiquinone radical in photolyase. *J. Biol. Chem.* **286**, 4382–4391 (2011).
57. Mei, Q. & Dvornyk, V., Evolutionary history of the photolyase/cryptochrome superfamily in eukaryotes. *PLoS One* **10**, e0135940 (2015).
58. Selby, C. P. & Sancar, A., A cryptochrome/photolyase class of enzymes with single-stranded DNA-specific photolyase activity. *Proc. Natl. Acad. Sci. USA* **103**, 17696–17700 (2006).

59. Pokorny, R., Klar, T., Hennecke, U., Carell, T., Batschauer, A. & Essen, L. O., Recognition and repair of UV lesions in loop structures of duplex DNA by DASH-type cryptochrome. *Proc. Natl. Acad. Sci. USA* **105**, 21023–21027 (2008).
60. Wang, X., Wang, Q., Nguyen, P. & Lin, C., Cryptochrome-mediated light responses in plants. *Enzymes* **35**, 167–189 (2014).
61. Damulewicz, M. & Mazzotta, G. M., One actor, multiple roles: The performances of cryptochrome in *Drosophila*. *Front. Physiol.* **11**, 99 (2020).
62. Sancar, A., Regulation of the mammalian circadian clock by cryptochrome. *J. Biol. Chem.* **279**, 34079–34082 (2004).
63. Xu, J., Jarocha, L. E., Zollitsch, T., Konowalczyk, M., Henbest, K. B., Richert, S., Golesworthy, M. J., Schmidt, J., Dejean, V., Sowood, D. J. C., Bassetto, M., Luo, J., Walton, J. R., Fleming, J., Wei, Y., Pitcher, T. L., Moise, G., Herrmann, M., Yin, H., Wu, H., Bartolke, R., Kasehagen, S. J., Horst, S., Dautaj, G., Murton, P. D. F., Gehrckens, A. S., Chelliah, Y., Takahashi, J. S., Koch, K. W., Weber, S., Solov'yov, I. A., Xie, C., Mackenzie, S. R., Timmel, C. R., Mouritsen, H. & Hore, P. J., Magnetic sensitivity of cryptochrome 4 from a migratory songbird. *Nature* **594**, 535–540 (2021).
64. Ahmad, M. & Cashmore, A. R., HY4 gene of *A. thaliana* encodes a protein with characteristics of a blue-light photoreceptor. *Nature* **366**, 162–166 (1993).
65. Toth, R., Kevei, E., Hall, A., Millar, A. J., Nagy, F. & Kozma-Bognar, L., Circadian clock-regulated expression of phytochrome and cryptochrome genes in *Arabidopsis*. *Plant Physiol.* **127**, 1607–1616 (2001).
66. Guo, H. Yang, H., Mockler, T. C. & Lin, C., Regulation of flowering time by *Arabidopsis* photoreceptors. *Science* **279**, 1360–1363 (1998).
67. Liu, H., Yu, X., Li, K., Klejnot, J., Yang, H., Lisiero, D. & Lin, C., Photoexcited CRY2 interacts with CIB1 to regulate transcription and floral initiation in *Arabidopsis*. *Science* **322**, 1535–1539 (2008).
68. Palayam, M., Ganapathy, J., Guercio, A. M., Tal, L., Deck, S. L. & Shabek, N., Structural insights into photoactivation of plant Cryptochrome-2. *Commun. Biol.* **4**, 28 (2021).
69. Shao, K., Zhang, X., Li, X., Hao, Y., Huang, X., Ma, M., Zhang, M., Yu, F., Liu, H. & Zhang, P., The oligomeric structures of plant cryptochromes. *Nat. Struct. Mol. Biol.* **27**, 480–488 (2020).
70. Emery, P., So, W. V., Kaneko, M., Hall, J. C. & Rosbash, M., CRY, a *Drosophila* clock and light-regulated cryptochrome, is a major contributor to circadian rhythm resetting and photosensitivity. *Cell* **95**, 669–679 (1998).
71. Zoltowski, B. D., Vaidya, A. T., Top, D., Widom, J., Young, M. W. & Crane, B. R., Structure of full-length *Drosophila* cryptochrome. *Nature* **480**, 396–399 (2011).
72. Ozturk, N., Selby, C. P., Annayev, Y., Zhong, D. & Sancar, A., Reaction mechanism of *Drosophila* cryptochrome. *Proc. Natl. Acad. Sci. USA* **108**, 516–521 (2011).

73. Vaidya, A. T., Top, D., Manahan, C. C., Tokuda, J. M., Zhang, S., Pollack, L., Young, M. W. & Crane, B. R., Flavin reduction activates *Drosophila* cryptochrome. *Proc. Natl. Acad. Sci. USA* **110**, 20455–20460 (2013).
74. Berntsson, O., Rodriguez, R., Henry, L., Panman, M. R., Hughes, A. J., Einholz, C., Weber, S., Ihalainen, J. A., Henning, R., Kosheleva, I., Schleicher, E. & Westenhoff, S., Photoactivation of *Drosophila melanogaster* cryptochrome through sequential conformational transitions. *Sci. Adv.* **5**, eaaw1531 (2019).
75. Chandrasekaran, S., Schneps, C. M., Dunleavy, R., Lin, C., DeOliveira, C. C., Ganguly, A. & Crane, B. R., Tuning flavin environment to detect and control light-induced conformational switching in *Drosophila* cryptochrome. *Commun Biol* **4**, 249 (2021).
76. Ceriani, M. F., Darlington, T. K., Staknis, D., Mas, P., Petti, A. A., Weitz, C. J. & Kay, S. A., Light-dependent sequestration of TIMELESS by CRYPTOCHROME. *Science* **285**, 553–556 (1999).
77. Koh, K., Zheng, X. & Sehgal, A., JETLAG resets the *Drosophila* circadian clock by promoting light-induced degradation of TIMELESS. *Science* **312**, 1809–1812 (2006).
78. Lin, C., Top, D., Manahan, C. C., Young, M. W. & Crane, B. R., Circadian clock activity of cryptochrome relies on tryptophan-mediated photoreduction. *Proc. Natl. Acad. Sci. USA* **115**, 3822–3827 (2018).
79. Ozturk, N., Selby, C. P., Zhong, D. & Sancar, A., Mechanism of photosignaling by *Drosophila* cryptochrome: role of the redox status of the flavin chromophore. *J. Biol. Chem.* **289**, 4634–4642 (2014).
80. Zou, Y., Wenzel, S., Muller, N., Prager, K., Jung, E. M., Kothe, E., Kottke, T. & Mittag, M., An animal-like cryptochrome controls the *Chlamydomonas* sexual cycle. *Plant Physiol.* **174**, 1334–1347 (2017).
81. Heijde, M., Zabulon, G., Corellou, F., Ishikawa, T., Brazard, J., Usman, A., Sanchez, F., Plaza, P., Martin, M., Falciatore, A., Todo, T., Bouget, F. Y. & Bowler, C., Characterization of two members of the cryptochrome/photolyase family from *Ostreococcus tauri* provides insights into the origin and evolution of cryptochromes. *Plant Cell Environ.* **33**, 1614–1626 (2010).
82. Beel, B., Prager, K., Spexard, M., Sasso, S., Weiss, D., Muller, N., Heinnickel, M., Dewez, D., Ikoma, D., Grossman, A. R., Kottke, T. & Mittag, M., A flavin binding cryptochrome photoreceptor responds to both blue and red light in *Chlamydomonas reinhardtii*. *Plant Cell* **24**, 2992–3008 (2012).
83. Spexard, M., Thoing, C., Beel, B., Mittag, M. & Kottke, T., Response of the sensory animal-like cryptochrome aCRY to blue and red light as revealed by infrared difference spectroscopy. *Biochemistry* **53**, 1041–1050 (2014).
84. Franz-Badur, S., Penner, A., Strass, S., von Horsten, S., Linne, U. & Essen, L. O., Structural changes within the bifunctional cryptochrome/photolyase *Cr*aCRY upon blue light excitation. *Sci. Rep.* **9**, 9896 (2019).

85. Lukacs, A., Eker, A. P., Byrdin, M., Brettel, K. & Vos, M. H., Electron hopping through the 15 A triple tryptophan molecular wire in DNA photolyase occurs within 30 ps. *J. Am. Chem. Soc.* **130**, 14394–14395 (2008).
86. Müller, P., Brettel, K., Grama, L., Nyitrai, M. & Lukacs, A., Photochemistry of wild-type and N378D mutant *E. coli* DNA Photolyase with oxidized FAD cofactor studied by transient absorption spectroscopy. *Chemphyschem* **17**, 1329–1340 (2016).
87. Woiczikowski, P. B., Steinbrecher, T., Kubar, T. & Elstner, M., Nonadiabatic QM/MM simulations of fast charge transfer in *Escherichia coli* DNA photolyase. *J. Phys. Chem. B* **115**, 9846–9863 (2011).
88. Langenbacher, T., Immeln, D., Dick, B. & Kottke, T., Microsecond light-induced proton transfer to flavin in the blue light sensor plant cryptochrome. *J. Am. Chem. Soc.* **131**, 14274–14280 (2009).
89. Immeln, D., Pokorny, R., Herman, E., Moldt, J., Batschauer, A. & Kottke, T., Photoreaction of plant and DASH cryptochromes probed by infrared spectroscopy: the neutral radical state of flavoproteins. *J. Phys. Chem. B* **114**, 17155–17161 (2010).
90. Kottke, T., Batschauer, A., Ahmad, M. & Heberle, J., Blue-light-induced changes in *Arabidopsis* cryptochrome 1 probed by FTIR difference spectroscopy. *Biochemistry* **45**, 2472–2479 (2006).
91. Burney, S., Wenzel, R., Kottke, T., Roussel, T., Hoang, N., Bouly, J. P., Bittl, R., Heberle, J. & Ahmad, M., Single amino acid substitution reveals latent photolyase activity in *Arabidopsis* cry1. *Angew. Chem. Int. Ed.* **51**, 9356–9360 (2012).
92. Müller, P., Bouly, J. P., Hitomi, K., Balland, V., Getzoff, E. D., Ritz, T. & Brettel, K., ATP binding turns plant cryptochrome into an efficient natural photoswitch. *Sci. Rep.* **4**, 5175 (2014).
93. Brautigam, C. A., Smith, B. S., Ma, Z., Palnitkar, M., Tomchick, D. R., Machius, M. & Deisenhofer, J., Structure of the photolyase-like domain of cryptochrome 1 from *Arabidopsis thaliana*. *Proc. Natl. Acad. Sci. USA* **101**, 12142–12147 (2004).
94. Ozturk, N., Kao, Y. T., Selby, C. P., Kavakli, I. H., Partch, C. L., Zhong, D. & Sancar, A., Purification and characterization of a type III photolyase from *Caulobacter crescentus*. *Biochemistry* **47**, 10255–10261 (2008).
95. Scheerer, P., Zhang, F., Kalms, J., von Stetten, D., Krauss, N., Oberpichler, I. & Lamparter, T., The class III cyclobutane pyrimidine dimer photolyase structure reveals a new antenna chromophore binding site and alternative photoreduction pathways. *J. Biol. Chem.* **290**, 11504–11514 (2015).
96. Holub, D., Lamparter, T., Elstner, M. & Gillet, N., Biological relevance of charge transfer branching pathways in photolyases. *Phys. Chem. Chem. Phys.* **21**, 17072–17081 (2019).
97. Müller, P., Yamamoto, J., Martin, R., Iwai, S. & Brettel, K., Discovery and functional analysis of a 4th electron-transferring tryptophan conserved exclusively in animal cryptochromes and (6–4) photolyases. *Chem. Commun.* **51**, 15502–15505 (2015).

98. Cailliez, F., Müller, P., Firmino, T., Pernot, P. & de la Lande, A., Energetics of photoinduced charge migration within the tryptophan tetrad of an animal (6–4) photolyase. *J. Am. Chem. Soc.* **138**, 1904–1915 (2016).
99. Ritz, T., Adem, S. & Schulten, K., A model for photoreceptor-based magnetoreception in birds. *Biophys. J.* **78**, 707–718 (2000).
100. Gegear, R. J., Foley, L. E., Casselman, A. & Reppert, S. M., Animal cryptochromes mediate magnetoreception by an unconventional photochemical mechanism. *Nature* **463**, 804–807 (2010).
101. Otsuka, H., Mitsui, H., Miura, K., Okano, K., Imamoto, Y. & Okano, T., Rapid oxidation following photoreduction in the avian cryptochrome4 photocycle. *Biochemistry* **59**, 3615–3625 (2020).
102. Zoltowski, B. D., Chelliah, Y., Wickramaratne, A., Jarocha, L., Karki, N., Xu, W., Mouritsen, H., Hore, P. J., Hibbs, R. E., Green, C. B. & Takahashi, J. S., Chemical and structural analysis of a photoactive vertebrate cryptochrome from pigeon. *Proc. Natl. Acad. Sci. USA* **116**, 19449–19457 (2019).
103. Oldemeyer, S., Franz, S., Wenzel, S., Essen, L. O., Mittag, M. & Kottke, T., Essential role of an unusually long-lived tyrosyl radical in the response to red light of the animal-like cryptochrome aCRY. *J. Biol. Chem.* **291**, 14062–14071 (2016).
104. Hong, G., Pachter, R., Essen, L. O. & Ritz, T., Electron transfer and spin dynamics of the radical-pair in the cryptochrome from *Chlamydomonas reinhardtii* by computational analysis. *J. Chem. Phys.* **152**, 065101 (2020).
105. Lacombat, F., Espagne, A., Dozova, N., Plaza, P., Müller, P., Brettel, K., Franz-Badur, S. & Essen, L. O., Ultrafast oxidation of a tyrosine by proton-coupled electron transfer promotes light activation of an animal-like cryptochrome. *J. Am. Chem. Soc.* **141**, 13394–13409 (2019).
106. Kiontke, S., Geisselbrecht, Y., Pokorny, R., Carell, T., Batschauer, A. & Essen, L. O., Crystal structures of an archaeal class II DNA photolyase and its complex with UV-damaged duplex DNA. *EMBO J.* **30**, 4437–4449 (2011).
107. Müller, P., Ignatz, E., Kiontke, S., Brettel, K. & Essen, L. O., Sub-nanosecond tryptophan radical deprotonation mediated by a protein-bound water cluster in class II DNA photolyases. *Chem. Sci.* **9**, 1200–1212 (2018).

Chapter 2

Involvement of a water molecule in photoactivation of plant (6–4) photolyases

2.1 Introduction

In this chapter, I investigated a factor that stabilizes photoinduced charge-separated states in plant *Arabidopsis thaliana* (6–4) photolyase (*At*64), by shedding light on the surroundings of the final electron donating Trp residue. This was the first investigation to suggest that a fixed water molecule proximal to the Trp residue has an impact on the stabilization of the charge-separated states in (6–4) photolyase. The results will inspire future theoretical and experimental works aiming at the molecular mechanisms of the stabilization of the charge-separated states caused by the Trp environment.

Photolyases (PLs) are flavoproteins able to repair crosslinks in DNA formed by exposure to ultraviolet (UV) in sunlight in a light-dependent manner, i.e. reverting cyclobutane pyrimidine dimers (CPDs) and pyrimidine(6–4)pyrimidone photoproducts ((6–4) PPs) to the intact pyrimidine nucleobases[1,2]. The key reaction of the light-driven DNA repair by PLs is an electron transfer from the excited state of fully-reduced flavin adenine dinucleotide ($FADH^-$) to the UV-damaged DNA[3]. On the other hand, FAD in PLs can take several redox states, namely oxidized (FAD_{ox}), semi-quinoid ($FADH^•$), and fully-reduced FAD ($FADH^-$), and PLs obtained as recombinant proteins generally possess fully or partially oxidized FADs, but not catalytic $FADH^-$[4,5]. FAD is buried in the active site where the UV-lesions are accommodated upon DNA recognition[6,7], and thus external reducing agents such as glutathione are hardly accessible to the FAD chromophore. For the efficient reduction of the FAD chromophore, there is a distinct photoreaction for reduction of oxidized FADs in PLs upon light illumination, in addition to the light-dependent DNA repair. This process is so-called photoactivation (and/or photoreduction)[8]. Upon FAD excitation, the excited state of FAD abstracts an electron from a neighboring tryptophan (Trp_1H) side chain[9], forming a charge-separated state of an FAD-Trp radical

pair. Subsequently, the radical cation of Trp_1H ($Trp_1H^{\bullet+}$) gets reduced by a secondary outer Trp (Trp_2H), and $Trp_2H^{\bullet+}$ is again reduced by the third Trp (Trp_3H) within <200 ps, as if the hole migrates toward the protein surface by hopping on the three Trp residues (Figure 1a)[10-12]. The charge separation between FAD and Trp_3H by ~14 Å inhibits the charge recombination, and the radical pair survives with a lifetime of up to milliseconds[13]. $Trp_3H^{\bullet+}$ is reduced by external reducing agents in solutions, stabilizing the reduced state of FAD.

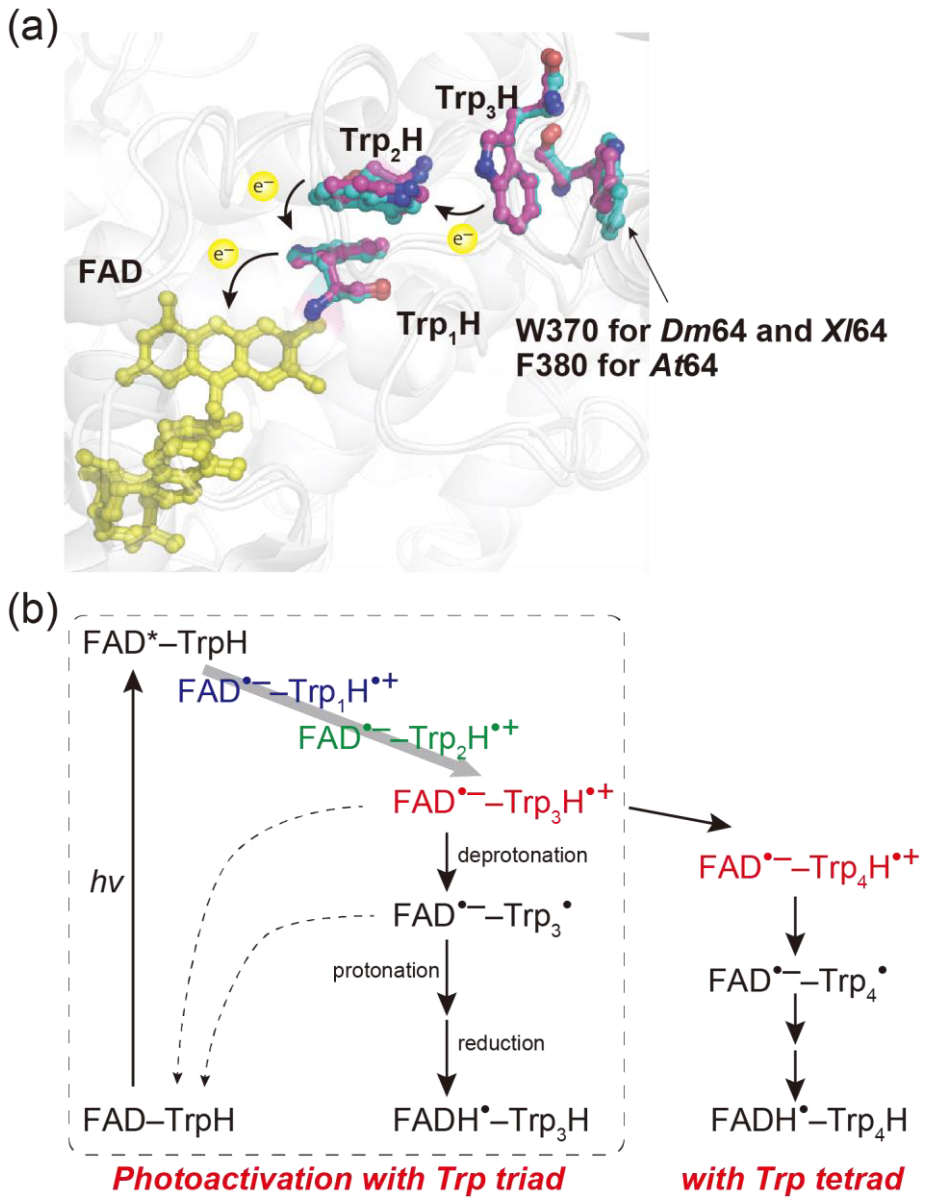

Figure 1. Photoactivation of FAD chromophore using Trp chains. (a) Superimposition of structures of *Arabidopsis thaliana* and *Drosophila melanogaster* (6–4) photolyases (3FY4[14] and 3CVU[7]). Their FAD and electron-transferring Trp chains are highlighted. The Trp chain in *Dm*64 and *At*64 are colored in cyan and magenta, respectively. Note that *Dm*64 and *Xl*64 share the presence of Trp_4H. (b) Reaction scheme for FAD photoreduction with the canonical Trp triad and tetrad. Abbreviations: *Xl* = *Xenopus laevis*; *At* = *Arabidopsis thaliana*; *Dm* = *Drosophila melanogaster*.

In some PLs, the final electron donor in the photoactivation is known to be an additional aromatic residue that reduces the third $TrpH^{\bullet+}$. In *Xenopus laevis* (6–4) PL (*Xl*64), a Trp residue at the 370th position (Trp370) exists proximal to Trp_3H, and its mutation to non-reducing phenylalanine (W370F) resulted in accelerated charge recombination by a factor of 4000, as compared to that of the wild type (WT)[15]. Such acceleration of the charge recombination in W370F of *Xl*64 significantly

affected its DNA repair ability in bacterial cells[16], due to the incapability of the formation of $FADH^{-}$, indicating that *Xl*64 utilizes Trp370 as the final electron donor in the photoactivation with the Trp tetrad. As the 4th Trp (Trp_4H) is located slightly away from the FAD chromophore, charge recombination between the FAD-Trp_4H pair would be suppressed better than the FAD-Trp_3H pair. According to the sequence alignment analysis, *Arabidopsis thaliana* (6–4) photolyase (*At*64) lacks Trp_4H but possess phenylalanine instead, meaning that *At*64 and *Xl*64-W370F share their photoactivating Trp chain (Figure 1a). Nonetheless, bacteria transformed with the plasmid containing the *At*64 gene reportedly survived upon successive illumination of UV and white light[16], indicating that photoactivation of *At*64 utilizes the canonical Trp triad. The contradictory observations between *At*64-WT and *Xl*64-W370F, sharing the same photoactivation Trp chain, implies an underlying mechanism for stabilization of the FAD-Trp radical pair independent on the radical pair distance.

The key processes for suppression of the charge recombination are protonation of the reduced FAD ($FAD^{\bullet-}$) and/or deprotonation of $TrpH^{\bullet+}$[17], the latter forming a neutral tryptophanyl radical ($Trp^{\bullet}$). In *Xl*64-WT, for instance, the time constant for the charge recombination of the $FAD^{\bullet-}$-$Trp_4H^{\bullet+}$ pair is reportedly >25 μs, while that of the $FAD^{\bullet-}$-$Trp_4^{\bullet}$ pair is 40 ms[15]. The deprotonation of $Trp_4H^{\bullet+}$ in *Xl*64-WT occurs in 2.5 μs, which is 10-times faster than the charge recombination process, and therefore the charge-separated state easily gets stabilized. In *Xl*64-W370F, on the other hand, the time constants for the charge recombination of the $FAD^{\bullet-}$-$Trp_3H^{\bullet+}$ pair and the deprotonation of $Trp_3H^{\bullet+}$ are coincident (400 ns)[15], leading to the less-stabilized charge-separated state in *Xl*64-W370F than in *Xl*64-WT. As superimposition of the crystal structures of *Drosophila melanogaster*

(6–4) photolyase (*Dm*64, sharing the Trp tetrad with *Xl*64) and *At*64 indicated that the distance and orientation between FAD and Trp_3H are almost identical (Figure 1a), the circumstance surrounding Trp_3H would significantly influence the fate of the charge-separated state of the FAD-Trp radical pair. Yet, the key factors that potentially control the physical process of the enzyme activation remain obscure. The FAD photoreduction process is also important for blue-light receptor cryptochromes (CRYs), regulatory proteins involved in gene expression, signal transduction, and circadian clock, as PLs and CRYs form a superfamily (PCSf) and share the electron-transferring Trp chains[1,18]. Understanding of the photoactivation process of PLs would thus potentially provide insights into the light-dependent functions of CRYs.

By revisiting the reported crystal structure of *At*64[14] in order to search for candidates that would stabilize the FAD-Trp radical pair, I noticed the presence of a water molecule proximal to Trp_3H. In this chapter, I investigate the role of the water molecule in the photoactivation of *At*64 by molecular dynamics (MD) simulations and photochemical/biochemical analyses using WT and mutants of *At*64, and found that the water molecule has a striking impact on the photoactivation of *At*64. The new insights obtained in this study into the photoactivation of FAD would be helpful to understand the photoactivation in other PLs and CRYs.

2.2 Results

2.2.1 Characteristic behaviors of a water molecule investigated by molecular dynamic simulations

To seek for the molecular origin of the stabilization of $Trp_3H^{\bullet+}$ in *At*64, I carefully inspected the reported structure of *At*64, and noticed the presence of a water molecule (Wat3139) at a distance

of 3.01 Å from the nitrogen atom in the indole moiety of Trp_3H (W329, Figure 2a). Because the previous theoretical study suggested that solvation of $TrpH^{\bullet+}$ could be one of the driving force of the hole transfer in the Trp tetrad[19], the water molecule proximal to the electron-transferring Trp residue would play a key role in the photoactivation of *At*64. Interestingly, not only Chain A of this coordinate but also Chains B and C contain the water molecule at the identical position. This water is located proximal to the main chain of Lys325 and side chains of Ser412, Trp383 (Trp_2H), Trp329 (Trp_3H), and Cys324 within hydrogen-bonding distances (Figure 2a). Since this water binding site is located near the protein surface, Wat3139 would perhaps be located by chance. In order to evaluate the behavior of this water molecule, molecular dynamic simulations of the *At*64 were carried out. The coordinate of the protein, the water molecules, and the chromophore of *At*64-WT was wrapped with the TIP3P water model, and the water coordinate in the crystal structure was replaced with the TIP3P model. After energy minimization, heating from 0 to 300 K, and equilibration for 1 ns, MD simulation was performed at 300 K for 200 ns. The distance between the oxygen atom of the water molecule in the binding site and the nitrogen of the indole ring of Trp_3H ($d_{O\cdots N}$) was extracted from the trajectory, and plotted over the simulation time (Figure 2b). In *At*64-WT, the water located in the binding site slightly fluctuated but did not escape from the binding site, keeping the average $d_{O\cdots N}$ of 3.04 ± 0.19 Å. Therefore, the water is stably captured by the surrounding amino acid residues.

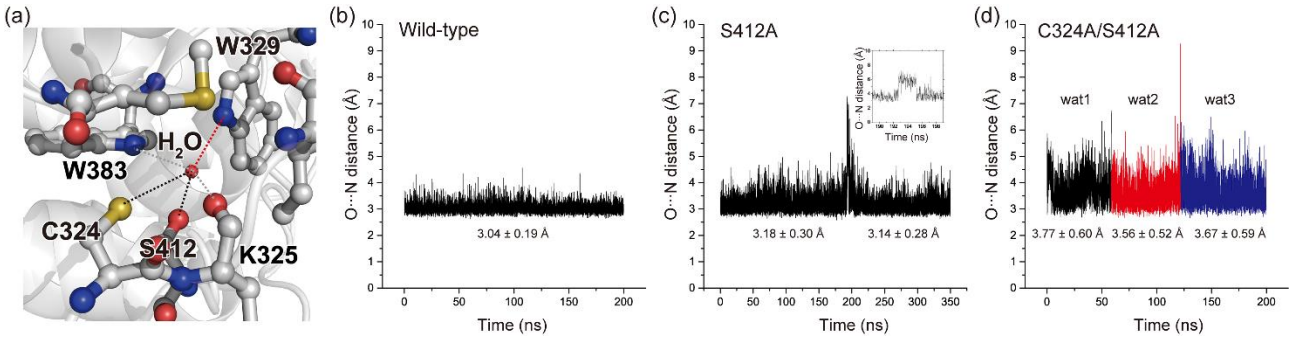

Figure 2. Characteristic behaviors of a water molecule proximal to Trp_3H in the MD simulations. (a) The structure of the water binding site in the close vicinity of Trp_3H of *At*64. The amino acids residues located within 4 Å from Wat3139 in the coordinates (Chain A of 3FY4) are highlighted. Gray dotted lines represent interactions between the water and the nitrogen atom of the indole ring of W383 (Trp_2H) or the carbonyl group in the main chain of K325, with their distances of 2.92 and 2.83 Å, respectively. Black dotted lines represent interactions between the water and the side chain of C324 or S412, with their distances of 3.37 and 2.87 Å. A red dotted line represents interaction between the water and the nitrogen atom of the indole ring of W329 (Trp_3H), with its distance of 3.01 Å. (b–d) Time developments of $d_{O\cdots N}$ in the MD simulations of (b) *At*64-WT, (c) the S412A mutant of *At*64, and (d) the C324A/S412A double mutant of *At*64. The inset in the panel (c) represents an expanded view of the position shift of the water molecule in the S412A simulation. The average O···N distances are noted in each panel.

As above mentioned, the side chains of Ser412 and Cys324, which are conserved well among (6–4) PLs and animal CRYs[15], seem to participate in the water recognition, and therefore the MD simulation for the S412A mutant was performed in the same way as for WT (Figure 2c). In this case, the average $d_{O\cdots N}$ within the first 180 ns was 3.18 ± 0.30 Å, indicating that the water molecule in S412A fluctuated a bit more than in WT. At ~190 ns simulation time, interestingly, $d_{O\cdots N}$ suddenly increased up to 7 Å (inset of Figure 2c), and after a few ns trip, the water came back to the binding site. Thus, I further performed an additional 150 ns simulation. The returned water was located at the average $d_{O\cdots N}$ of 3.14 ± 0.28 Å during the 150 ns simulation. These results demonstrated that the water was recognized less by the S412A mutant than by WT, indicating that the Ser412 side chain participates in the water recognition.

To check the involvement of Cys324 in the water recognition, MD simulation of the

C324A/S412A double mutant was performed in the same way (Figure 2d). In the first 58 ns simulation, the water was located at the average $d_{O\cdots N}$ of 3.77 ± 0.60 Å, indicating that the water molecule is less recognized in the binding site. Even more interestingly, Wat528, which is the water molecule initially located in the binding site (wat1), escaped to the bulk and the Wat25943 molecule occupied the binding site instead of wat1. Although the second water (wat2) was located in the binding site at the average $d_{O\cdots N}$ of 3.56 ± 0.52 Å during 60 ns simulation time, $d_{O\cdots N}$ of wat2 suddenly became large again and wat2 was hidden in the bulk. Instead, third water, Wat20605 (wat3), came into the binding site from the bulk. The wat3 was located at the average $d_{O\cdots N}$ of 3.67 ± 0.59 Å for the rest of the simulation time without replacement. These results demonstrate that introduction of the C324A mutation drastically increases the frequency of water replacement.

2.2.2 Roles of Ser412 and Cys324 in the water recognition

To gain insights into the possible role of the Ser412 and Cys324 residues in the water recognition, the structures obtained by the MD simulations were carefully surveyed. Interestingly, two hydrogen atoms of the captured water molecule in the *At*64-WT simulation kept directing toward the O atom of the main chain of Lys325 and the O atom of the side chain of Ser412, forming hydrogen bonds (Figure 3a). These two H atoms were not distinctive because the flipping of the water molecule was observed during the 200 ns MD simulation (Figures 3b and c). However, the dipole moment of the water kept directing toward the margin between Lys325 and Ser412, meaning that the orientation of the water molecule is strictly regulated by the protein environment. In the S412A structure, on the

other hand, the water molecule was mainly held by the main chain of Lys325 and side chains of Trp329 and Trp383, and the direction of the dipole moment of the water in the S412A simulation was totally different from that in the WT simulation, with more fluctuation than in WT. These observations suggest that Ser412 would play a role in anchoring the water molecule.

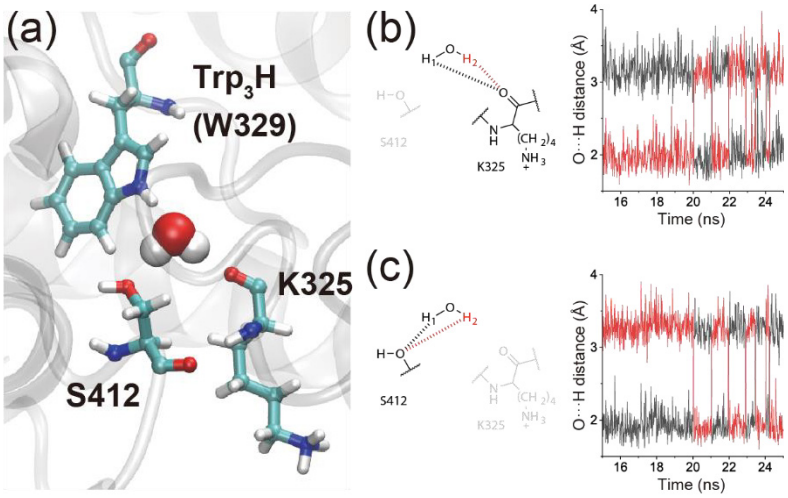

Figure 3. Orientation of the captured water molecule in the MD simulations. (a) A snapshot of the structure of *At*64-WT. K325, W329 (Trp_3H), and S412 residues in addition to the captured water molecule are highlighted. (b and c) Distance analysis of hydrogen bonds between two hydrogen atoms of the captured water (H_1 and H_2 shown in black and red, respectively) and (b) the O atom of the main chain of K325 or (c) the O atom of the side chain of S412, in 15–25 ns simulation time.

Even more interestingly, the trajectory of S412A simulation revealed that the distance between the sulfur atom of Cys324 and the O atom of Lys325 suddenly increased at the occurrence of the water displacement (Figure 4b and c). As shown in Figure 2d, the absence of Cys324, i.e. the C324A/S412A double mutant, caused the increased frequency of water replacement in the binding site. In some cases, two water molecules were observed in the binding site (Figure 4d and e), indicating that loss of the Cys324 side chain increases the accessibility of water to the Trp_3H. By

contrast, *in silico* attempt whether the water can spontaneously be incorporated into the binding site of WT was unsuccessful with a 200 ns simulation time, and no water molecule was incorporated into the binding site when the initial structure without the captured water was used (data not shown). These results indicate that Cys324 would play a role in water gating, inhibiting water molecules going in and out of the water binding site.

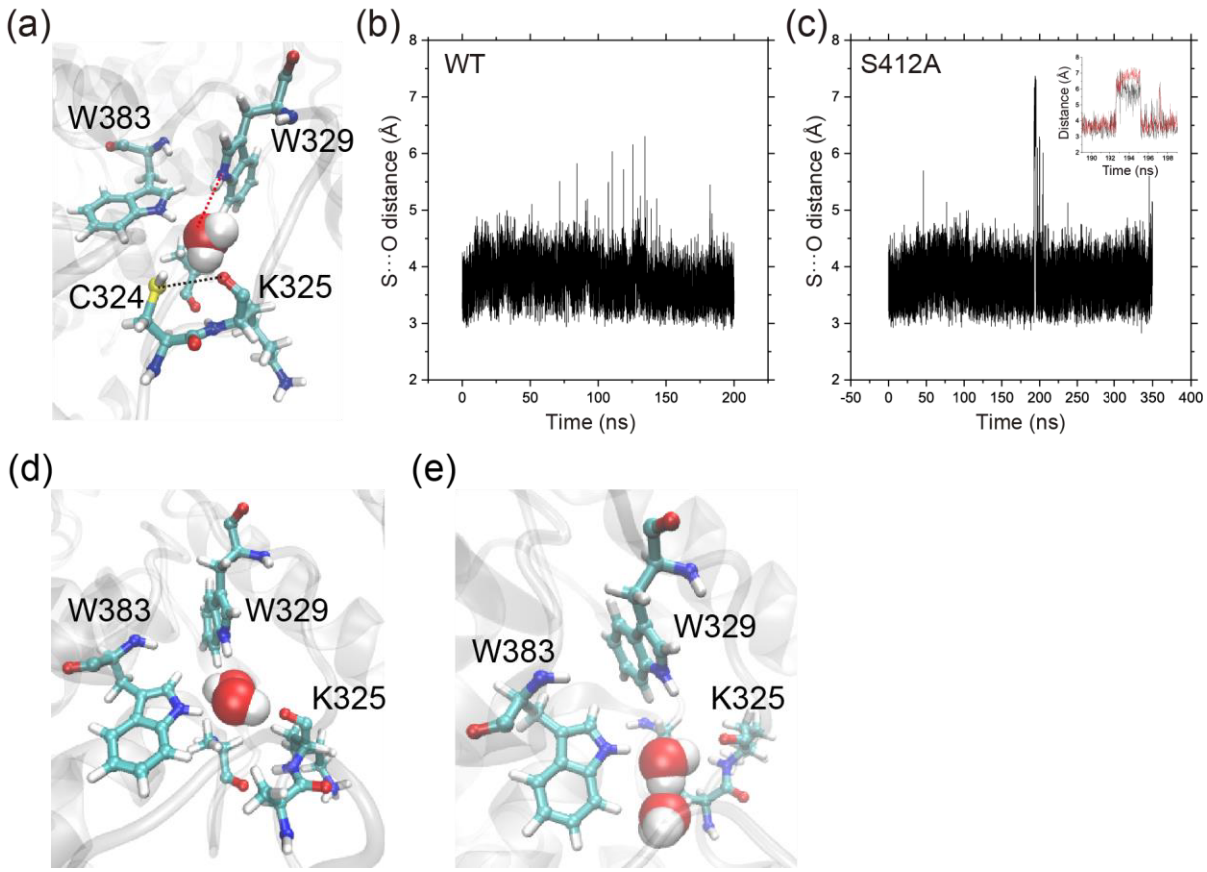

Figure 4. Plausible roles of C324 in the water binding. (a) A snapshot of the trajectory for the S412A simulation. The black and red dotted lines represent the focused distances. (b and c) Distance analysis between the sulfur atom of the side chain of C324 and the oxygen atom of the main chain of K325 (S···O distance) in the (b) WT or (c) S412A trajectories. The inset in panel (c) is a superimposition of the expanded view of the S···O distance (black) and $d_{O\cdots N}$ (red). The latter is reproduced from Figure 2c. The occurrence of the water trip and the Cys-Lys gate opening is obviously coincident. (d and e) Two water molecules in the binding site in the MD simulation of the C324A/S412A double mutant. Snapshots of the trajectory at (d) 36 ns and (e) 125 ns are shown.

2.2.3 FAD photoreduction abilities of WT and mutants of At64 in bacteria and in vitro

The MD simulations of the WT and the mutants of *At*64 suggested that the water molecule proximal to the Trp_3H is well recognized in the binding site through the hydrogen bonds, while mutations of the amino acid residues in the binding site increases the accessibility of water. To link the behavior of the water molecule observed in the MD simulation to the characteristic function of *At*64, FAD photoreduction abilities of the WT and the mutants of *At*64 were investigated. In the previous study on the FAD photoreduction of *Xl*64, mutation of the Trp tetrad significantly reduced the survival of bacteria upon successive illumination of UV and white light[16], indicating that *Xl*64 requires the photoactivation process for the formation of catalytic $FADH^-$ in bacteria, while this process is reportedly not required for *E. coli* PL in bacteria[20,21]. For *At*64 utilizing the canonical Trp triad, it has been shown that the mutation of Trp_3H into non-reducible phenylalanine caused significant decrease in survival[16]. If the water molecule captured in the binding site contributes to the stabilization of the charge-separated state of the FAD-Trp radical pair, survival of bacteria transformed with the plasmids containing the S412A or C324A/S412A mutant genes would be reduced as compared to those expressing the WT gene, because $FADH^-$ formation required for the DNA repair ability of PLs would be suppressed. To check FAD photoreduction abilities of these mutants, the UV survival assay was performed in the same way as in the previous study (Figure 5). At 0.6 J m^{-2} UV irradiation, the survival of bacteria expressing the Trp_3H-lacking mutant (W329F) gene was significantly reduced (1.3 ± 0.2%) as compared to those producing the WT (17 ± 2.7%). Interestingly, survivals of S412A- and C324A/S412A-expressing bacteria at 0.6 J m^{-2} irradiation were

found to be 2.4 ± 2.3% and 3.6 ± 1.5% with their *P*-values of 0.0024 and 0.0019, respectively, as compared to the results obtained for the WT, and their survivals were in the similar range to those expressing W329F. These results suggest that the stably captured water in the binding site has an impact on the DNA repair ability of *At*64, presumably due to inefficient formation of catalytic $FADH^{-}$.

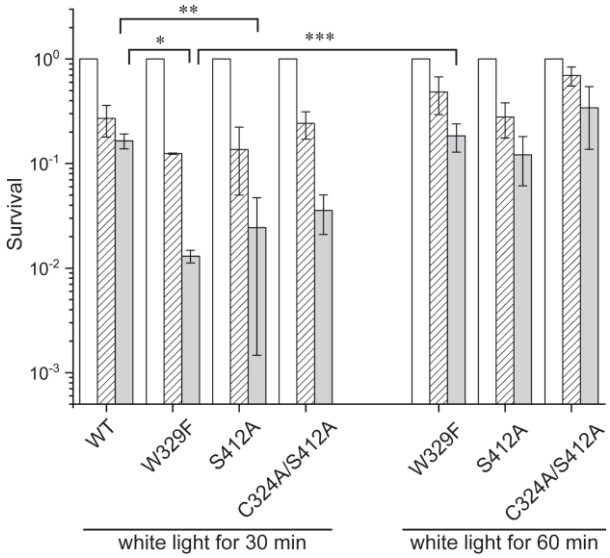

Figure 5. Survivals of *E. coli* transformed with the plasmids containing the WT or the mutants of *At*64 genes upon 0 (open bar), 0.3 (shaded bar), and 0.6 (gray bar) J m^{-2} UV irradiation, followed by white light illumination for 30 or 60 min. The experiment was performed in triplicate ($n = 3$), and the data were statistically analyzed by Student's *t*-test. Statistic significance was set to $P < 0.05$. Each point and error bar represents mean ± SD. Asterisks indicate *P* values of 0.0024 (*), 0.0019 (**), and 0.0061 (***), respectively.

To gain insights into what extent the captured water molecule has impact on the photoactivation, UV survival with the prolonged white light illumination was investigated. In the previous study, the prolonged white light illumination up to 90 min did not affect the survival of the bacteria transformed with the plasmid containing the *Xl*64-W370F gene[16]. The FAD photoreduction of recombinant *Xl*64-W370F was 1000-fold decelerated as compared to that of *Xl*64-WT, and thus the $FADH^{-}$ formation of *Xl*64-W370F was strongly inhibited in cells. If the photoreduction is not so

slow in the *At*64-S412A, $FADH^-$ would be formed upon extended illumination of white light, leading to the recovery of the survival. The survival of the S412A-expressing bacteria with the white light illumination for 60 min was found to be 12 ± 6%, which is in the range similar to that for *At*64-WT with the 30 min illumination. Interestingly, the similar tendency was observed for the bacteria expressing the *At*64-W329F or *At*64-C324A/S412A genes with the prolonged white light illumination, and their survivals were found to be 18 ± 4.5% for *At*64-W329F and 34 ± 20% for *At*64-C324A/S412A. These results indicate that the mutants of *At*64 acquired the DNA repair activity by the prolonged white light illumination, in contrast to the previous results of the UV survival assay using bacteria expressing the *Xl*64-W370F gene.

In order to investigate the FAD photoreduction abilities of the mutants of *At*64, the S412A and C324A/S412A mutants of *At*64 in addition to *At*64-WT were obtained as recombinant proteins bearing FAD_{ox}, and their photoreduction under anaerobic conditions were performed (Figure 6). Upon light illumination, FAD_{ox} in *At*64-WT was immediately reduced, and almost all FAD_{ox} molecules were converted to $FADH^-$ after 3 min (Figure 6a). The decay of the absorbance at 450 nm (A_{450}), which is the characteristic absorption band of FAD_{ox}, was fitted with a monoexponential function, and its half-life ($t_{1/2}$) was found to be 0.36 ± 0.0089 min under the experimental conditions. The same experiment was performed with the W329F mutant of *At*64 (Figure 6b), and its $t_{1/2}$ was 7.37 ± 0.23 min, indicating a 20-folds slower reaction than in the WT. The FAD photoreduction in the S412A mutant was decelerated as compared to that in the WT (Figure 6c), and its $t_{1/2}$ was 1.55 ± 0.10 min. Interestingly, the C324A/S412A double mutant, in which the water molecule was frequently replaced

during the simulation time (Figure 6d), exhibited the FAD photoreduction kinetics similar to the S412A mutant, and $t_{1/2}$ of the double mutant was 1.54 ± 0.093 min. These observations indicated that the hydrogen-bonding network including the captured water, not merely the presence of the water molecules near Trp_3H, would be important for the proper photoactivation of *At*64.

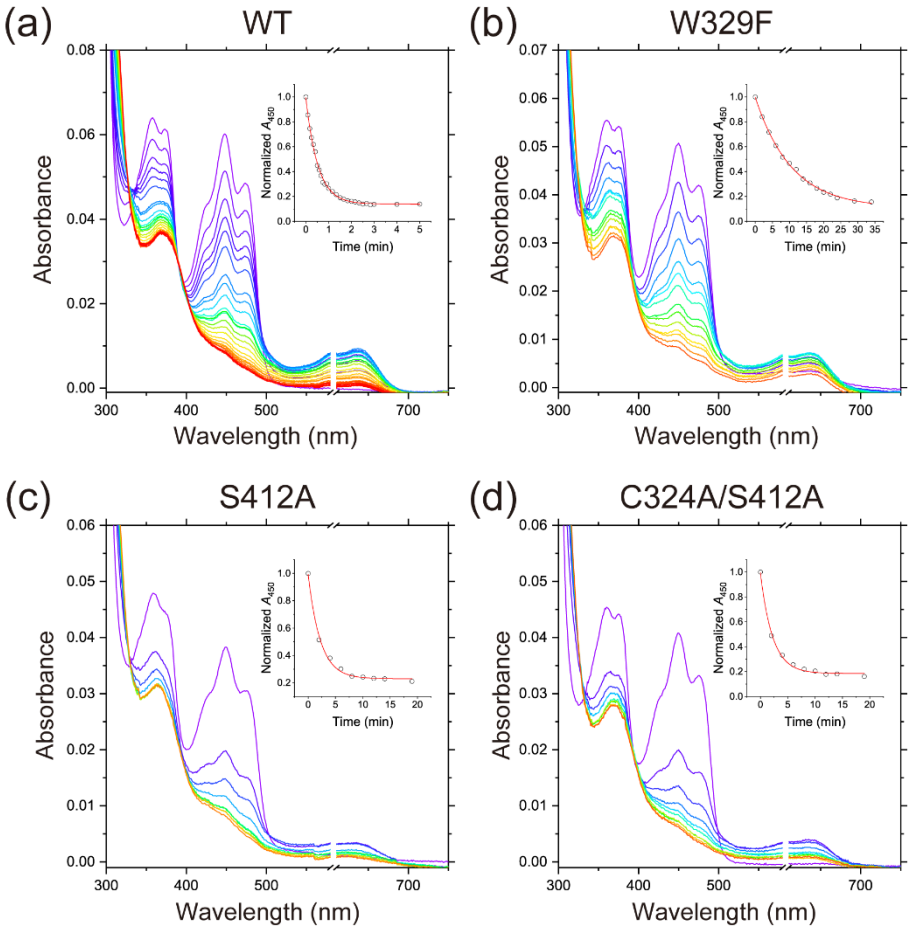

Figure 6. Photoreduction of FAD in recombinant *At*64 under anaerobic conditions. The recombinant proteins of (a) WT, (b) W329F, (c) S412A, and (d) C324A/S412A of *At*64 were illuminated with >430 nm white light for a certain period under anaerobic conditions, and their spectra were recorded. This process was repeated until the formation of $FADH^-$ was observed. The spectra shown in purple, blue, green, yellow, and red represent the initial to final states upon the light illumination in order. Note that the spectra in 580–610 nm regions are omitted, because there was a non-reproducible bump in this region caused by instrumental problems. The inset in each panel represents the decay of normalized A_{450} plotted over the total illumination time. The data points were fitted with a monoexponential decay function, and the obtained curves are shown in red.

The survival of the bacteria transformed with the plasmids containing the Trp_3H-lacking

*At*64 gene was recovered upon the prolonged white light illumination (Figure 5), while such prolonged white light illumination did not improve the survival of the bacteria transformed with the plasmid containing the Trp_4H-lacking *Xl*64 gene[16]. These observations suggest that the $FADH^-$ ratio in the photostationary states of FAD in *At*64 upon the white light illumination would significantly be higher than that in *Xl*64. The possible reason for the effect of the prolonged white light illumination would be the difference in the reoxidation rates of FAD in *At*64 and *Xl*64. $FADH^-$ formation in cells is in competition with the spontaneous reoxidation, and thus $FADH^-$ can hardly be formed if the reoxidation is much faster than the FAD photoreduction. To check the reoxidation of *At*64-WT and *Xl*64-WT, anaerobically-prepared $FADH^-$ in *At*64 and *Xl*64 was exposed to air, by removing the cap of the anaerobic cuvette, and the absorption spectra were measured (Figure 7). Obviously, formation of FAD_{ox} in *At*64 was much slower than in *Xl*64, and even after 3 hours, $FADH^-$ was the major redox state, whereas reoxidation of $FADH^-$ back to FAD_{ox} in *Xl*64 was achieved quickly (within 5 min). These results suggested that the FAD photoreduction of *Xl*64-W370F in bacteria was strongly suppressed due to the decelerated FAD photoreduction and the fast reoxidation back to FAD_{ox}. In the mutants of *At*64 in bacteria, on the other hand, the reoxidation of the reduced FAD is not as significant as in *Xl*64, and $FADH^-$ would be accumulated upon white light illumination slowly, leading to the recovery of the survival.

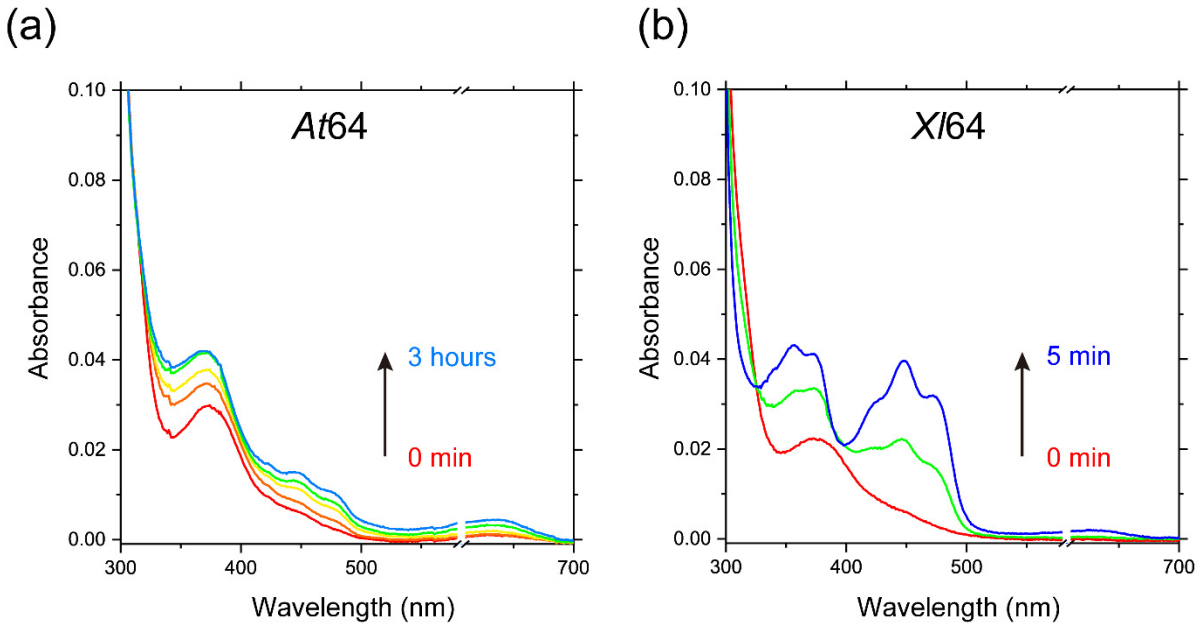

Figure 7. Reoxidation of $FADH^-$ in (a) *At*64 and (b) *Xl*64 under the aerobic conditions. After the photoreduction experiments under the anaerobic conditions, the cap of the anaerobic cuvette was removed. The nitrogen atmosphere in the cuvette was gently replaced with air, and the absorption spectra were measured at appropriate intervals without the cap. Note that the spectra in 580–610 nm regions are omitted, as described in the legend of Figure 6.

2.3 Discussion

2.3.1 Plausible roles of the captured water molecule in the photoactivation of At64

To find clues to the molecular basis of the function of the captured water molecule, I focused the outside of the water binding site. The direction of the hydroxyl group of Ser412 is almost fixed during the MD simulation of the WT, and the Ser412 side chain interacts with the hydroxyl group of Ser410 through a hydrogen bond (Figure 8a). Furthermore, the hydroxyl group of Ser410 interacts with C=O of Trp406 (Trp_1H) through a hydrogen bond (Figure 8a). These hydrogen-bonding networks including Ser412-H_2O-Lys325 would contribute to the suppression of the local fluctuation, keeping the relative orientation and distance between FAD and the Trp triad constant. One may thus consider that break of the hydrogen-bonding network by introduction of the S412A mutation would cause the disordered fluctuation around the Trp triad, leading to decelerated FAD photoreduction. To

check the possibility, the root mean square fluctuation (RMSF) of the trajectories was analyzed (Figure 8b). Indeed, the RMSF values in the 413–435 region for the C324A/S412A mutant were much more prominent than for the WT and the S412A mutant. Because the water molecule ties up two loops where Ser412 and Lys325 are located (Figure 8a), this observation would be caused by the loss of the ordered hydrogen-bonding network including the captured water, meaning that the water molecule would contribute to the stabilization of the protein structure to some extent. However, the RMSF values in the region where the Trp triad is located were not changed by the mutations, indicating that the absence of the captured water molecule would hardly cause fluctuation of the Trp triad.

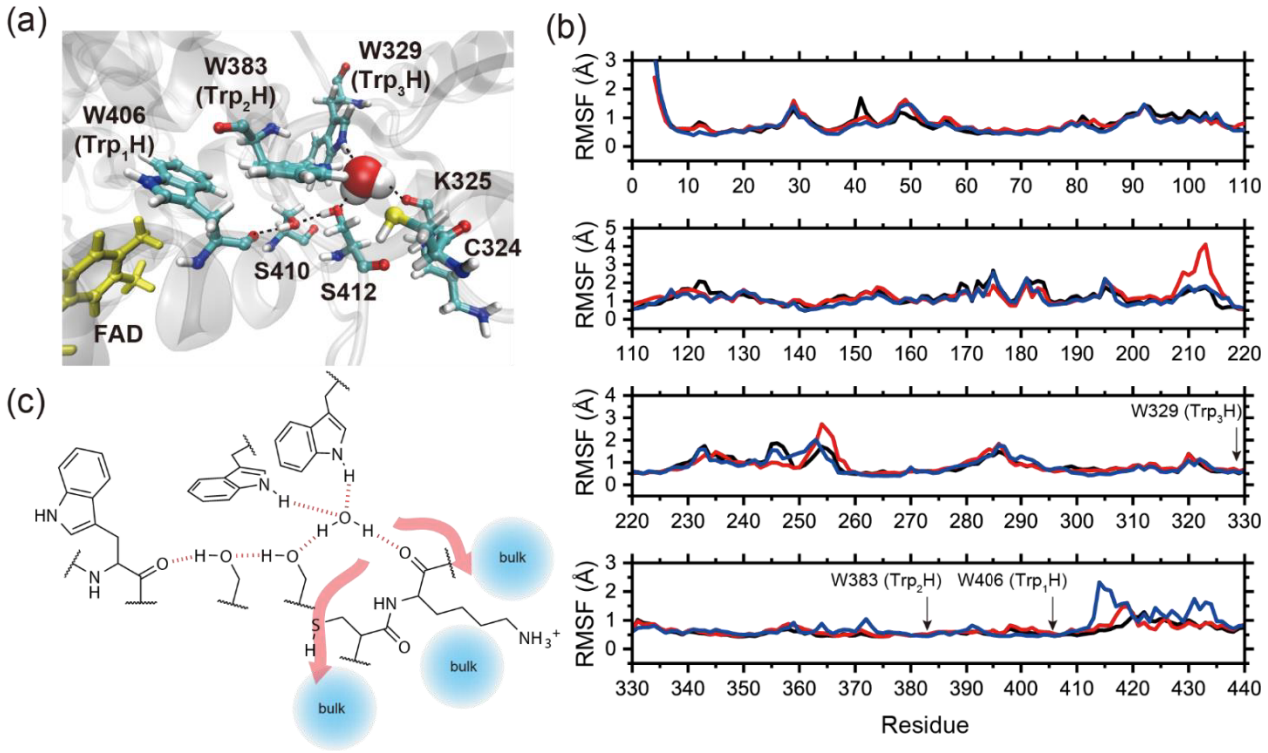

Figure 8. Role of the hydrogen-bonding network including the captured water molecule. (a) A snapshot of the MD trajectory of *At*64-WT. FAD, the Trp triad, and the amino acid residues involved in the hydrogen-bonding network are highlighted. (b) Root mean square fluctuation (RMSF) analysis of the trajectories of the WT (black), S412A (red), or C324A/S412A (blue) MD simulations. Although *At*64 consists of ~520 amino acids, the results up to 440 amino acids are shown. The positions of the Trp triad for *At*64 are highlighted in red in the sequence. Obviously, the RMSF values of the Trp triad for the mutants are almost the same as that for the WT, indicating that the absence of the captured water hardly has an impact on the fluctuation of the Trp triad. (c) A schematic view of the hydrogen-bonding network. The hydrogen bonds are shown in red, and possible proton release pathways to the bulk are shown with red arrows.

Considering possible roles of the water molecule apart from the structural stabilization, the captured water molecule with the hydrogen-bonding network would directly be involved in the stabilization of the FAD-Trp radical pair, probably through the deprotonation of $Trp_3H^{\bullet+}$. The deprotonation process facilitates the formation of the $FAD^{\bullet-}$-$Trp_3^{\bullet}$ radical pair, the charge recombination of which is in general much slower than that of the $FAD^{\bullet-}$-$Trp_3H^{\bullet+}$ pair[22]. The Ser412-H_2O-Lys325 hydrogen-bonding network finely regulates the position and the orientation of the captured water molecule (Figures 2 and 3), directing the lone pair of the O atom of H_2O toward the

N-H of Trp_3H, and therefore this captured water molecule would function as a proton acceptor of the $Trp_3H^{\bullet+}$ (Figure 8c). Supposing the possible involvement of water as the proton acceptor, the question is how and to where the proton would be released. The primary candidate of the proton release pathway would be along the hydrogen-bonding network, although the pathway toward Trp406 is directed toward the inner side of the protein and there are no proton accepting groups around Lys325 (Figure 8a). The second possibility would be involvement of Cys324 in the proton release from the $Trp_3H^{\bullet+}$ radical cation, working as a proton relay (Figure 8c). During the MD simulations, some water molecules were prone to be located outside of the Cys324, and therefore the proton might be released through the Cys324 side chain to the bulk.

Such a facilitated proton release of $TrpH^{\bullet+}$ to the water cluster has recently been reported for *Methanosarcina mazei* class II CPD (*Mm*CPDII), in which the proton release of the oxidized tryptophan takes place in a sub-ns order (0.2–0.4 ns)[23,24]. The Trp_3H of *Mm*CPDII (Trp388) is surrounded by a protein-bound cluster of 8 water molecules, and one of the water molecules (Wat247) is located near the N-H group of Trp388 in the crystal structure[25]. This Wat247 is recognized by Glu387, and the E387Q mutation of *Mm*CPDII scarcely alters the deprotonation kinetics of Trp388, suggesting that the water cluster, not the Glu387 residue, would directly be involved in the proton acceptor. In the case of *Mm*CPDII, the final electron donor of its photoactivation is considered to be a tyrosine residue at the 345th position, and the rapid formation of $Trp^{\bullet}$ would be important both for the stabilization of the FAD-Trp radical pair and the proton-coupled electron transfer from Tyr345 to $Trp388^{\bullet}$, leading to the formation of the stable $FAD^{\bullet-}$-$Tyr^{\bullet}$ radical pair. It is hence likely that *At*64

would also utilize the hydrogen-bonding network including the captured water found in this study, for the stabilization of the FAD-Trp radical pair, although the detailed kinetic analysis will be required to determine the role of the network in photoactivation of *At*64.

2.3.2 Relevance of photoactivation of PLs to CRYs

PCSf shares FAD photoreduction utilizing the Trp chain, whereas the light-absorbing form of FAD is $FADH^-$ for PLs and FAD_{ox} for CRYs. The photoactivation process of CRYs largely attracts attentions of researchers as the proteins with the reduced form of FAD is thought to be the signaling state and also the FAD-Trp radical pair in CRYs would sense the magnetic field on Earth[18,26]. One of the key factors that tunes the redox state of FAD in PCSf is an amino acid residue near the N5 of the isoalloxazine ring, and in principle, asparagine is exclusively conserved among PLs[27]. In *Drosophila melanogaster* CRY, the conserved Asn is replaced with Cys, which greatly prolongs the lifetime of $FAD^{\bullet-}$, and the Asn-to-Cys mutation in *Synechocystis sp.* CRY-DASH reportedly modulated the photoactivation ability[28]. In *Arabidopsis thaliana* CRY1, the conserved Asn is replaced with Asp, which remarkably facilitates the protonation of $FAD^{\bullet-}$ as compared to PLs[29]. Although the amino acid residues surrounding the FAD chromophore are relatively well conserved among PCSf except the above two examples, the surroundings of the final electron donor of the photoactivating Trp chain are critically diverse. Recent theoretical studies demonstrate that the solvent is a driving force for the downhill hole transfer along the Trp chain, and contributes to the stabilization of the FAD-Trp radical pair[19,30]. Thus, the circumstance of the photoactivation Trp chain would also have an impact on tuning

the photoactivation process of PCSf. Nonetheless, systematic investigations about the surroundings of the final electron donor have not been performed, except a recent research on *Drosophila melanogaster* CRY[31]. It is noteworthy that the hydrogen-bonding network highlighted in this study is located near the junction to the C-terminus domain, which plays a key role in the CRY functions[18]. This implies that the hydrogen-bonding network would potentially be involved in the light-dependent structural change of the C-terminus domain of CRYs, although more studies should be performed in future. This work, in addition to the recent *Mm*CPDII studies[23,24], will provide an idea that water is attributable to the photoactivation of PCSf.

2.4 Methods

Classical Molecular Dynamics Simulation

All molecular dynamics (MD) simulations were performed with the AMBER 16 program package[32]. The atomic coordinates of *At*64-WT were obtained from Protein Data Bank (with its accession number of 3FY4), and Chain A of 3FY4 was used as the initial structure. The initial structures of S412A and C324A/S412A mutants of *At*64 were generated with SWISS-MODEL[33] using 3FY4 as the template structure. The geometric optimization and the electronic structure calculation for $FADH^-$ were performed using Gaussian09[34] at B3LYP/6-31G(d) and MP2/6-311++G(2d,2p) level, respectively. The obtained results were converted into the Amber force field using the Antechamber module[35] of the AMBER 16 program package. In this study, I applied the Amber force field 14SB[36] for the proteins and TIP3P water model[37] for the water molecules. For the

simulation boxes, I constructed a margin of at least 12 Å from the proteins to the box boundaries. To neutralize the system, some counter ions (Cl^-) were added. The total atom numbers for WT, S412A, and C324A/S412A were 74385, 79742, and 80029, respectively.

In this study, I performed MD simulations as follows. First, the energy minimization for each system was performed for 5000 steps using the Sander module by imposing restrictions on heavy atoms, with a force constant of 10 kcal mol^{-1} $Å^{-2}$. Then, the energy minimization without any restrictions was performed for 10000 steps. Each system was then heated from 0 K to 300 K for 100 ps with an *NVT* ensemble (T = 300 K). Next, the equilibration runs were performed for 1 ns with an *NPT* ensemble (P = 1 atm and T = 300 K). Finally, the production runs were performed with the *NPT* ensemble (P = 1 atm and T = 300 K) for 200 ns on the WT and the C324A/S412A double mutant and for 350 ns on the S412A mutant. In all MD simulations, the SHAKE algorithm was used for the constraints[38], and the periodic boundary condition with the particle mesh Ewald method was applied[39]. The simulation time step was set to 2 fs, and a snapshot was recorded in every 20 ps. The trajectories were analyzed by the CPPTRAJ module of the AMBER 16 program package[40], and visualized with a VMD software[41].

Mutagenesis

The S412A and W329F mutant genes of *At*64 were generated with QuikChange Site-Directed Mutagenesis Kit (Agilent Technologies, La Jolla, CA) using the pGEX-4T-1 plasmid encoding *At*64 as a template[16]. The following sets of PCR primers were used:

d(GTGGTTATCATGTGCGTCGTTCTTTTACCA) and d(TGGTAAAAGAACGACGCACATGATAACCAC) for S412A; and d(TGCAAACAGATTCCATTCAACGAGGATCAT) and d(ATGATCCTCGTTGAATGGAATCTGTTTGCA) for W329F. The C324A/S412A double mutant gene was generated with QuikChange Site-Directed Mutagenesis Kit using the pGEX-4T-1 plasmid carrying the S412A mutant as a template. The set of PCR primers for introduction of the C324A mutation was as follows: d(GGGAAACCGGATCGCCAAACAGATTCCATG) and d(CATGGAATCTGTTTGGCGATCCGGTTTCCC).

After the treatment of the PCR product with a restriction enzyme DpnI, *E. coli* DH5α competent cells were transformed with the products. The purified plasmids were sequenced and used for the survival assay and construction of the pET plasmids.

Cell Culture

The *E. coli* SY32 strain lacking *phr*, *recA*, and *uvrA* genes, but transfected with the pACYC184 plasmid encoding CPD-PL from *E. coli* to ensure specific photorepair of the CPD lesions, was used for the survival assay[42]. After colony selection by Luria-Broth (LB) agar plates containing tetracycline (10 μg mL^{-1}), chloramphenicol (15 μg mL^{-1}), and kanamycin (10 μg mL^{-1}), the cells were further transformed with the pGEX-4T-1 plasmid encoding *At*64-WT or its S412A, W329F, or C324A/S412A mutant. The co-transfected bacteria were cultured in 1.5 mL LB medium containing tetracycline (10 μg mL^{-1}) and ampicillin (80 μg mL^{-1}) at 37°C overnight. The culture was diluted to

OD_{600} = 0.5 with LB medium. The diluted culture (1 mL) was induced with 2.4 μL of 10 mg mL^{-1} isopropyl β-D-1-thiogalactopyranoside (IPTG) at 37°C for 1 hour.

Survival Assay

The survival assay was performed as described previously[16,43]. Briefly, the culture described above was appropriately diluted with phosphate buffered saline, and aliquots (150 μL) were spread onto LB agar plates containing tetracycline and ampicillin. The plates were illuminated with a 20 W UV germicidal lamp (UVL20PH-6, Sen Lights Co. Ltd., Osaka, Japan) through metal mesh filters (2.0 μW cm^{-2}, calibrated with a UVX radiometer equipped with a 254 nm probe, UVP, LLC, Upland, CA) for 15 or 30 s, to yield a total irradiance of 0.3 or 0.6 J m^{-2}, respectively. Subsequently, the plates were illuminated with fluorescent lamps (18W×4, FL20SSD/18, Toshiba, Tokyo, Japan) for 30 or 60 min and incubated at 37°C overnight. The obtained colonies were counted, and the numbers were corrected taking into account the dilution percentage. All survival rates were normalized to the number of colonies formed without UV irradiation (set thus to 1). The experiments were independently performed in triplicate, and the data were analyzed by a Student's *t*-test. Statistical significance was set to $P < 0.05$.

Protein Purification

Constructs for protein production were prepared as follows. WT and mutants of *At*64 genes in the pGEX-4T-1-plasmids described above were amplified by PCR with PrimeSTAR MAX DNA

polymerase (Takara), using a forward primer possessing a *NdeI* restriction enzyme site, d(CCCCATATGGCTACTGGATCCGGT), and a reverse primer possessing a *XhoI* restriction enzyme site, d(GGGCTCGAGCTATTTGAGTTTTGGTCGTTG). The PCR product was treated with *NdeI* and *XhoI* at 37°C for 1 hour, and the excised product was purified with agarose gel. The modified pET-28a plasmid bearing *Xenopus laevis* (6–4) PL gene[15] was also treated with *NdeI* and *XhoI* at 37°C for 1 hour, and the 5 kb product was purified with agarose gel. The PCR product and the vector treated with *NdeI* and *XhoI* were ligated using Ligation High mix (Toyobo), and DH5α competent cells were transformed with the ligation mixture. The purified plasmid bearing the *At*64 genes were sequenced and used for the following procedure, in a similar manner to the previous report[44].

E. coli C41(DE3)/pLysS (Lucigen) cells transformed with the pET28a-based plasmids were cultivated in 2 mL LB medium containing ampicillin (50 μg mL^{-1}) and chloramphenicol (100 μg mL^{-1}) at 37°C overnight. The preculture was inoculated into 2 L LB medium containing ampicillin (50 μg mL^{-1}) in a 5 L flask with baffles, and cells were grown at 25°C until OD_{600} reached 1.2 – 1.6. After IPTG was added at a final concentration of 0.2 mM, the culture was further incubated at 25°C for 24 h. After harvest, the pellet was resuspended in 40 mL of a lysis buffer (20 mM NaH_2PO_4, 500 mM NaCl, 5% glycerol pH 7.4 adjusted by KOH, plus 65 mg of lysozyme) and lysed by sonication. After centrifugation of the cell lysate, supernatant was poured into an open column filled with TALON® Metal Affinity Resin (Clontech, TaKaRa) equilibrated with the lysis buffer. The column was washed with four column volumes of a wash buffer (20 mM NaH_2PO_4, 500 mM NaCl, 10 mM imidazole, 5% glycerol, pH 7.4 adjusted by KOH), and the His-tagged protein was eluted with an elution buffer (20

mM NaH_2PO_4, 500 mM NaCl, 500 mM imidazole, 5% glycerol, pH 7.4 adjusted by KOH). The blue-green eluate was loaded onto a HiTrap Heparin HP Column (GE Healthcare), and the column was manually washed with 5 mL of Buffer 1 (50 mM Tris-HCl, 5% glycerol, 100 mM NaCl), Buffer 2 (50 mM Tris-HCl, 5% glycerol, 200 mM NaCl), Buffer 3 (50 mM Tris-HCl, 5% glycerol, 300 mM NaCl) and Buffer 4 (50 mM Tris-HCl, 5% glycerol, 400 mM NaCl). The purified enzyme was confirmed by SDS-PAGE and the concentration was measured on the basis of the FAD absorbance at 450 nm, using a molecular extinction coefficient of 11300 L mol^{-1} cm^{-1}.

Photoreduction Assay

The purified enzyme solution (70 μL) diluted to 20 μM was applied to a Micro Bio-Spin 6 column (BIO-RAD) equilibrated with a reaction buffer, consisting of 20 mM phosphate (pH 7.5), 500 mM NaCl, 10% glycerol. The eluate (60 μL) was transferred to an anaerobic 10 mm × 2 mm × 8 mm (length × width × height) inner volume quartz cuvette (Starna, 16.160-F/4/Q/10 GL 14/2/Z15), and the sample was sealed with a screw cap and PTFE-coated silicone and rubber septa. The atmosphere in the cuvette was degassed and replaced with nitrogen through the septa, and the cuvette was transferred into an anaerobic glove box. Under anaerobic and dark conditions, the sample was mixed with L-cysteine (the final concentration of which was 5 mM) and the reaction buffer, and the final volume of the sample solution was 240 μL.

The anaerobic samples were illuminated with continuous light (~430–800 nm) from a MAX-150 xenon lamp (ASAHI SPECTRA), through the 10 mm × 8 mm window. After illumination of the sample on ice for a certain period, the sample solution was mixed by gentle shaking, and an absorption spectrum was measured at 10°C through the 10 mm path on a Lambda 35 UV/VIS spectrometer (PerkinElmer), equipped with a sample holder connected to a water cooling system. The absorbance at 450 nm of the obtained spectra were plotted and fitted with a monophasic exponential decay function with an Origin2019 software.

2.5 Conclusions

I investigated the possible involvement of a water molecule proximal to the Trp_3H of the *At*64 crystal structure in the photoactivation process. MD simulations clearly suggested that the water is stably captured in the WT, while the mutation of S412, which is a hydrogen-bonding partner of the water molecule, impaired DNA repair in bacteria and decelerated FAD photoreduction in the recombinant protein. The experimental observations in addition to *in silico* protein and water behaviors indicate that the hydrogen-bonding network around the final electron-donating Trp_3H significantly plays a key role, presumably in the stabilization of the FAD-Trp_3H radical pair of *At*64. Although more detailed analysis will be required in future so as to address the molecular mechanisms of the stabilization of the radical pair, this work provided an example that showed the direct involvement of the water in the photoactivation.

References

1. Sancar, A., Structure and function of DNA photolyase and cryptochrome blue-light photoreceptors. *Chem. Rev.* **103**, 2203–2238 (2003).
2. Yamamoto, J., Plaza, P. & Brettel, K., Repair of (6–4) lesions in DNA by (6–4) photolyase: 20 years of quest for the photoreaction mechanism. *Photochem. Photobiol.* **93**, 51–66 (2017).
3. Zhong, D., Electron transfer mechanisms of DNA repair by photolyase. *Annu. Rev. Phys. Chem.* **66**, 691–715 (2015).
4. Sancar, A., Smith, F. W. & Sancar, G. B., Purification of *Escherichia coli* DNA photolyase. *J. Biol. Chem.* **259**, 6028–6032 (1984).
5. Todo, T., Kim, S.-T., Hitomi, K., Otoshi, E., Inui, T., Morioka, H., Kobayashi, H., Ohtsuka, E., Toh, H. & Ikenaga, M., Flavin adenine dinucleotide as a chromophore of the *Xenopus* (6–4)photolyase. *Nucleic Acids Res.* **25**, 764–768 (1997).
6. Mees, A., Klar, T., Gnau, P., Hennecke, U., Eker, A. P. M., Carell, T. & Essen, L.-O., Crystal structure of a photolyase bound to a CPD-Like DNA lesion after in situ repair. *Science* **306**, 1789–1793 (2004).
7. Maul, M. J., Barends, T. R. M., Glas, A. F., Cryle, M. J., Domratcheva, T., Schneider, S., Schlichting, I. & Carell, T., Crystal structure and mechanism of a DNA (6–4) photolyase. *Angew. Chem. Int. Ed.* **47**, 10076–10080 (2008).
8. Aubert, C., Vos, M. H., Mathis, P., Eker, A. P. M. & Brettel, K., Intraprotein radical transfer during photoactivation of DNA photolyase. *Nature* **405**, 586–590 (2000).
9. Byrdin, M., Eker, A. P. M., Vos, M. H. & Brettel, K., Dissection of the triple tryptophan electron transfer chain in *Escherichia coli* DNA photolyase: Trp382 is the primary donor in photoactivation. *Proc. Natl. Acad. Sci. U.S.A.* **100**, 8676–8681 (2003).
10. Brazard, J., Usman, A., Lacombat, F., Ley, C., Martin, M. M., Plaza, P., Mony, L., Heijde, M., Zabulon, G. & Bowler, C., Spectro-temporal characterization of the photoactivation mechanism of two new oxidized cryptochrome/photolyase photoreceptors. *J. Am. Chem. Soc.* **132**, 4935–4945 (2010).
11. Liu, Z., Tan, C., Guo, X., Li, J., Wang, L., Sancar, A. & Zhong, D., Determining complete electron flow in the cofactor photoreduction of oxidized photolyase. *Proc. Natl. Acad. Sci. U.S.A.* **110**, 12966–12971 (2013).
12. Martin, R., Lacombat, F., Espagne, A., Dozova, N., Plaza, P., Yamamoto, J., Müller, P., Brettel, K. & de la Lande, A., Ultrafast flavin photoreduction in an oxidized animal (6-4) photolyase through an unconventional tryptophan tetrad. *Phys. Chem. Chem. Phys.* **19**, 24493–24504 (2017).
13. Byrdin, M., Sartor, V., Eker, A. P. M., Vos, M. H., Aubert, C., Brettel, K. & Mathis, P., Intraprotein electron transfer and proton dynamics during photoactivation of DNA photolyase from *E. coli*: review and new insights from an “inverse” deuterium isotope effect. *Biochim. Biophys. Acta* **1655**, 64–70 (2004).

14. Hitomi, K., DiTacchio, L., Arvai, A. S., Yamamoto, J., Kim, S.-T., Todo, T., Tainer, J. A., Iwai, S., Panda, S. & Getzoff, E. D., Functional motifs in the (6–4) photolyase crystal structure make a comparative framework for DNA repair photolyases and clock cryptochromes. *Proc. Natl. Acad. Sci. U.S.A.* **106**, 6962–6967 (2009).
15. Müller, P., Yamamoto, J., Martin, R., Iwai, S. & Brettel, K., Discovery and functional analysis of a 4th electron-transferring tryptophan conserved exclusively in animal cryptochromes and (6–4) photolyases. *Chem. Commun.* **51**, 15502–15505 (2015).
16. Yamamoto, J., Shimizu, K., Kanda, T., Hosokawa, Y., Iwai, S., Plaza, P. & Müller, P., Loss of fourth electron-transferring tryptophan in animal (6–4) photolyase impairs DNA repair activity in bacterial cells. *Biochemistry* **56**, 5356–5364 (2017).
17. Byrdin, M., Lukacs, A., Thiagarajan, V., Eker, A. P. M., Brettel, K. & Vos, M. H., Quantum yield measurements of short-lived photoactivation intermediates in DNA photolyase: toward a detailed understanding of the triple tryptophan electron transfer chain. *J. Phys. Chem. A* **114,** 3207–3214 (2010).
18. Chaves, I., Pokorny, R., Byrdin, M., Hoang, N., Ritz, T., Brettel, K., Essen, L.-O., van der Horst, G. T. J., Batschauer, A. & Ahmad, M., The cryptochromes: blue light photoreceptors in plants and animals. *Annu. Rev. Plant Biol.* **62**, 335–364 (2011).
19. Cailliez, F., Müller, P., Firmino, T., Pernot, P. & de la Lande, A., Energetics of photoinduced charge migration within the tryptophan tetrad of an animal (6–4) photolyase. *J. Am. Chem. Soc.* **138**, 1904–1915 (2016).
20. Payne, G., Heelis, P. F., Rohrs, B. R. & Sancar, A., The active form of *Escherichia coli* DNA photolyase contains a fully reduced flavin and not a flavin radical, both *in vivo* and *in vitro*. *Biochemistry* **26**, 7121–7127 (1987).
21. Kavakli, I. H. & Sancar, A., Analysis of the role of intraprotein electron transfer in photoreactivation by DNA photolyase *in vivo*. *Biochemistry* **43**, 15103–15110 (2004).
22. Brettel, K. & Byrdin, M., Reaction mechanisms of DNA photolyase. *Curr. Opin. Struct. Biol.* **20**, 693–701 (2010).
23. Müller, P., Ignatz, E., Kiontke, S., Brettel, K. & Essen, L.-O., Sub-nanosecond tryptophan radical deprotonation mediated by a protein-bound water cluster in class II DNA photolyases. *Chem. Sci.* **9**, 1200–1212 (2018).
24. Lacombat, F., Espagne, A., Dozova, N., Plaza, P., Ignatz, E., Kiontke, S. & Essen, L.-O., Delocalized hole transport coupled to sub-ns tryptophanyl deprotonation promotes photoreduction of class II photolyases. *Phys. Chem. Chem. Phys.* **20**, 25446–25457 (2018).
25. Kiontke, S., Geisselbrecht, Y., Pokorny, R., Carell, T., Batschauer, A. & Essen, L.-O., Crystal structures of an archaeal class II DNA photolyase and its complex with UV-damaged duplex DNA. *EMBO J.* **30**, 4437–4449 (2011).
26. Gegear, R. J., Foley, L. E., Casselman, A. & Reppert, S. M., Animal cryptochromes mediate magnetoreception by an unconventional photochemical mechanism. *Nature* **463**, 804–807 (2010).

27. Wijaya, I. M. M., Domratcheva, T., Iwata, T., Getzoff, E. D. & Kandori, H., Single hydrogen bond donation from flavin N5 to proximal asparagine ensures FAD reduction in DNA photolyase. *J. Am. Chem. Soc.* **138**, 4368–4376 (2016).
28. Iwata, T., Zhang, Y., Hitomi, K., Getzoff, E. D. & Kandori, H., Key dynamics of conserved asparagine in a cryptochrome/photolyase family protein by fourier transform infrared spectroscopy. *Biochemistry* **49**, 8882–8891 (2010).
29. Müller, P., Bouly, J.-P., Hitomi, K., Balland, V., Getzoff, E. D., Ritz, T. & Brettel, K., ATP binding turns plant cryptochrome into an efficient natural photoswitch. *Sci. Rep.* **4**, 5175 (2014).
30. Lüdemann, G., Solov'yov, I. A., Kubař, T. & Elstner, M., Solvent driving force ensures fast formation of a persistent and well-separated radical pair in plant cryptochrome. *J. Am. Chem. Soc.* **137**, 1147–1156 (2015).
31. Lin, C., Top, D., Manahan, C. C., Young, M. W. & Crane, B. R., Circadian clock activity of cryptochrome relies on tryptophan-mediated photoreduction. *Proc. Natl. Acad. Sci. USA* **115**, 3822–3827 (2018).
32. Case, D. A., Babin, V., Berryman, J. T., Betz, R. M., Cai, Q., Cerutti, D. S., Cheatham, T. E., Darden, T. A., Duke, R. E., Gohlke, H., *et al.* Amber16. University of California, San Francisco.
33. Waterhouse, A., Bertoni, M., Bienert, S., Studer, G., Tauriello, G., Gumienny, R., Heer, F. T., de Beer, T. A. P., Rempfer, C., Bordoli, L., *et al.* SWISS-MODEL: Homology modelling of protein structures and complexes. *Nucleic Acids Res.* **46**, W296–W303 (2018).
34. Frisch, M. J., Trucks, G. W., Schlegel, H. B., Scuseria, G. E., Robb, M. A., Cheeseman, J. R., Scalmani, G., Barone, V., Mennucci, B., Petersson, G. A., *et al.* Gaussian09. 1st ed. Gaussian, Inc.: Wallingford CT.
35. Wang, J., Wang, W., Kollman, P. A. & Case, D. A., Automatic atom type and bond type perception in molecular mechanical calculations. *J. Mol. Graph. Model.* **25**, 247–260 (2006).
36. Maier, J. A., Martinez, C., Kasavajhala, K., Wickstrom, L., Hauser, K. E. & Simmerling, C., ff14SB: Improving the accuracy of protein side chain and backbone parameters from ff99SB. *J. Chem. Theory Comput.* **11**, 3696–3713 (2015).
37. Jorgensen, R. W., Chandrasekhar, J., Madura, J. D., Impey, R. W. & Klein, M. L., Comparison of simple potential functions for simulating liquid water. *J. Chem. Phys.* **79**, 926–935 (1983).
38. Ryckaert, J.-P., Ciccotti, G. & Berendsen, H. J. C., Numerical integration of the cartesian equations of motion of a system with constraints: molecular dynamics of n-alkanes. *J. Comput. Phys.* **23**, 327–341 (1977).
39. Darden, T., York, D. & Pedersen, L., Particle mesh Ewald: an N·log(N) method for Ewald sums in large systems. *J. Chem. Phys.* **98**, 10089–10092 (1993).

40. Roe, D. R. & Cheatham, T. E., III. PTRAJ and CPPTRAJ: software for processing and analysis of molecular dynamics trajectory data. *J. Chem. Theory Comput.* **9**, 3084–3095 (2013).
41. Humphrey, W., Dalke, A. & Schulten, K., VMD: visual molecular dynamics. *J. Mol. Graph.* **14**, 33–38 (1996).
42. Todo, T., Ryo, H., Yamamoto, K., Toh, H., Inui, T., Ayaki, H., Nomura, T. & Ikenaga, M., Similarity among the *Drosophila* (6–4)photolyase, a human photolyase homolog, and the DNA photolyase-blue-light photoreceptor family. *Science* **272**, 109–112 (1996).
43. Terai, Y., Sato, R., Yumiba, T., Harada, R., Shimizu, K., Toga, T., Ishikawa-Fujiwara, T., Todo, T., Iwai, S., Shigeta, Y. & Yamamoto, J., Coulomb and CH–π interactions in (6–4) photolyase–DNA complex dominate DNA binding and repair abilities. *Nucleic Acids Res.* **46**, 6761–6772 (2018).
44. Li, J., Liu, Z., Tan, C., Guo, X., Wang, L., Sancar, A. & Zhong, D. Dynamics and mechanism of repair of ultraviolet-induced (6–4) photoproduct by photolyase. *Nature* **466**, 887–890 (2010).

Chapter 3

Essential roles of limited solvation of an electron donating tryptophan in photoactivation of plant (6–4) photolyases

3.1 Introduction

In the previous chapter, I discovered that a water molecule close to the final electron donating Trp residue is required for the efficient photoreduction in plant (6–4) photolyases, but the mechanism enabling the water to participate in the reaction was not fully identified. In this chapter, comprehensive analyses by steady-state photoreduction experiments, transient absorption spectroscopy, and molecular dynamics simulations revealed that regulated solvation of the Trp residue including the water molecule stabilizes photoinduced charge-separated state. The newly identified mechanisms will expand the arsenal of tricks employed by photolyases and cryptochromes to achieve efficient photoreduction.

Photolyases and cryptochromes constitute a superfamily (PCSf) of ubiquitous structurally related photoactive flavoproteins[1,2]. The evolutionarily older photolyases (PLs) have specialized in the photoenzymatic repair of major UV-induced lesions: cyclobutane pyrimidine dimers (CPDs; specifically repaired by CPD PLs) and pyrimidine(6–4)pyrimidone photoproducts ((6–4) PPs; specifically repaired by (6–4) PLs). Cryptochromes (CRYs), which branched off from photolyases, have gradually lost their ability to repair DNA, but have progressively acquired new physiological functions as blue light receptors driving photomorphogenesis in plants or entraining the circadian clock in both plants and animals[2]. Numerous theoretical and experimental works suggest that animal cryptochromes, which group together with animal (6–4) photolyases, are also responsible for the ability of migratory birds and other animals to sense the Earth's magnetic field and use it for orientation[3,4].

PCSf proteins perform two distinct kinds of photoreactions: photorepair and photoactivation. In photorepair, which is unique to photolyases and a few rare 'dual' proteins (capable of acting as both DNA repair enzymes and photoreceptors[5–7]), the photoexcited fully reduced flavin ($^*FADH^-$) transfers an electron to the DNA lesion fixed in a nearby specific binding pocket. This electron transfer (ET) triggers bond rearrangement within the lesion, which, upon electron return to the intrinsically semi-oxidized (or semi-reduced) $FADH^\bullet$, ultimately leads to restoration of two intact bases and thus to DNA repair.

Nevertheless, the flavin cofactor in PLs is not always in the catalytically active (fully reduced) form and therefore needs to be activated (reduced). This happens in the latter reaction called photoactivation. Photoactivation, which is common to both PLs and CRYs, is a light-induced reduction of the oxidized (FAD_{ox}) or semi-reduced ($FADH^\bullet$) flavin chromophore via a chain of electron-transferring aromatic residues, typically three tryptophans. Upon excitation, $^*FAD_{ox}$ or $^*FADH^\bullet$ abstract an electron from a nearby Trp residue[8] (Trp_1H), producing a ~4 Å charge-separated state ($FAD^{\bullet-}/FADH^- \cdots Trp_1H^{\bullet+}$). $Trp_1H^{\bullet+}$ subsequently gets an electron from a second Trp residue[9] (Trp_2H), and the resulting radical cation $Trp_2H^{\bullet+}$ in turn acquires an electron from yet another Trp residue near the protein surface[10–12] (Trp_3H), as illustrated in Figure 1a. The successive ET on the sub-nanosecond time scales yields a ~15 Å charge-separated state ($FAD^{\bullet-}/FADH^- \cdots Trp_3H^{\bullet+}$). Finally, deprotonation[13] of $Trp_3H^{\bullet+}$ to $Trp_3^\bullet$ and quenching of $Trp_3^\bullet$ by external reducing agents[14] stabilize the $FAD^{\bullet-}/FADH^-$ state[15] (see Figure 1b detailing the first photoactivation step starting with FAD_{ox} and yielding the semi-reduced $FAD^{\bullet-}/FADH^\bullet$). While the catalytically active redox form of FAD in DNA

repair by PLs is $FADH^-$, light signaling by CRYs is believed to be triggered by FAD_{ox} photoreduction to $FAD^{\bullet-}$ (or by a negative charge on a neighboring residue that protonated $FAD^{\bullet-}$ to $FADH^{\bullet}$)[16-18]. Most CRYs hence seem to use only the first photoactivation step.

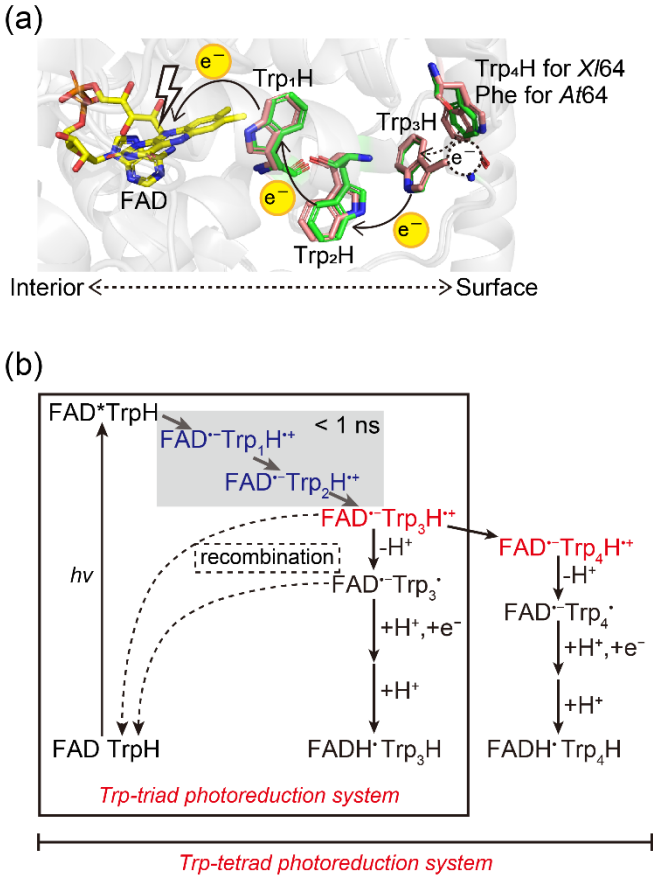

Figure 1. Scheme of FAD photoreduction in PCSf proteins. (a) The crystal structure of *At*64 (PDB entry 3FY4)[19] is superimposed onto a homology model structure of *Xl*64 using the crystal structure of (6–4) PL from *Drosophila melanogaster* (6–4) PL (PDB entry 3CVU)[20] as template. FAD is shown in yellow, electron-transferring tryptophans and redox-inactive phenylalanine in *At*64 and *Xl*64 are shown in green and in salmon, respectively. (b) Reaction scheme detailing typical photo-induced charge transfer, charge separation and radical stabilization in PCSf proteins with Trp triads and tetrads. TrpH, $TrpH^{\bullet+}$, and $Trp^{\bullet}$ denote the normal (non-oxidized) tryptophan state, the one-electron-oxidized cation radical, and the one-electron-oxidized deprotonated neutral radical, respectively.

To ensure efficient photoactivation, PCSf proteins employ a plethora of ingenious tricks stabilizing the light-induced radicals and preventing futile charge recombination: *e.g.*, branching

and/or elongation of the ET chain to four or even five residues[21–23], rapid (~μs) protonation of $FAD^{\bullet-}$ (unique to plant cryptochromes)[24], or rapid (sub-ns) deprotonation of the last member of the ET chain. The latter can be achieved by the presence of a proton acceptor next to the terminal member of the ET chain (*e.g.*, a deprotonated aspartic or glutamic acid[25] or a cluster of structured water molecules communicating with the surrounding buffer[26]) or by using tyrosine as the terminal residue of the chain (while $TrpH^{\bullet+}$ has a pK_a of ~4[27], $TyrH^{\bullet+}$ has a p*K*a of ~ −2[28] and deprotonates immediately in aqueous buffers).

In this chapter, I focused on the (6–4) photolyase from *Arabidopsis thaliana* (*At*64), which, despite possessing a mere Trp triad, exhibits surprisingly high activity in bacterial cells – comparable to that of *Xenopus laevis* (6–4) PL (*Xl*64)[29], which contains a Trp tetrad, and the photoactivation of which is known to yield very stable charge separation and unusually long-lived radical pairs[21]. After a series of experimental and theoretical studies, *At*64 is suggested to achieve efficient photoactivation by using a different set of tricks from other PCSf proteins: 1) rapid localization of the electron hole on the 3rd Trp (which is inferred from an unusually high (>80%) quantum yield of the $FAD^{\bullet-}$ $Trp_3H^{\bullet+}$ pairs, implying proportionally low losses of primary and secondary $FAD^{\bullet-}$ $TrpH^{\bullet+}$ pairs by ultrafast recombination), and 2) prevention of solvent access to $Trp_3H^{\bullet+}$, which extends its lifetime by a factor of ten (compared to a mutant with solvent-exposed 3rd Trp). I proposed that a histidine residue adjacent to the 3rd Trp and highly conserved in plant (6–4) PLs plays a key role in stabilization of $Trp_3H^{\bullet+}$, thus expanding the arsenal of tricks leading to efficient photoactivation of PCSf proteins.

3.2 Results

3.2.1 Primary and tertiary structures revealing major differences in the environment of Trp_3H in plant and animal (6–4) PLs

To address how plant (6–4) PLs are finely adapted to FAD photoreduction via the Trp triad, I assumed that residues around Trp_3H affect the formation and/or stabilization of the photoinduced $FAD^{\bullet-}$ $Trp_3H^{\bullet+}$ charge-separated state. To explore the differences in the environment of Trp_3H in plant and animal (6–4) PLs, the crystal structure of *At*64[19] (PDB entry 3FY4) was superimposed onto a homology model structure of *Xl*64 generated as previously described[21] (Figure 2a). Apart from the phenylalanine residue (Phe380 in *At*64), which is replaced with the fourth tryptophan in animal (6–4) PLs (Trp370 in *Xl*64), the only major difference in the closest neighborhood of Trp_3H (within 4 Å) is that a histidine residue conserved in plant (6–4) PLs (His382 in *At*64) is substituted with a serine in animal (6–4) PLs (Ser372 in *Xl*64). The remaining residues around Trp_3H are either conserved (Trp383 and Met318 in *At*64 numbering) or very similar (Ile327 in *At*64 *vs.* Val317 in *Xl*64).

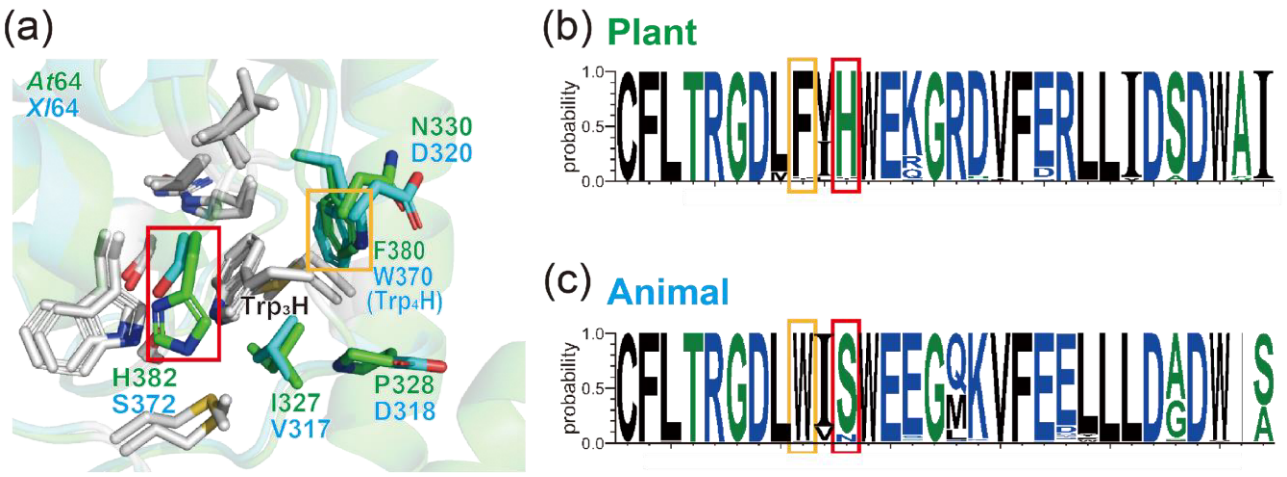

Figure 2. Structure and sequence analyses of plant and animal (6–4) PL orthologues. The phenylalanine inside the yellow box corresponds to F380 in *At*64. The histidine corresponding to H382 in *At*64 is highlighted in red. The electron-transferring Trp_4H (W370 in *Xl*64) is marked in yellow. The serine inside the red frame corresponds to S372 in *Xl*64. (a) The local three-dimensional structures around Trp_3H in *At*64 and *Xl*64. Residues conserved in both (6–4) PLs are shown in light grey. Residues unique to *At*64 and *Xl*64 are colored in green and cyan, respectively. (b and c) Primary structural analyses of (b) plant and (c) animal (6–4) PL orthologues.

Sequence analyses revealed that as high as 95% of compared plant (6–4) PL orthologues retain the His residue, and 92% of the animal (6–4) PL orthologues retain the Ser residue (Figures 2b and c). Interestingly, in no plant (6–4) PL orthologues is the histidine replaced with a serine, suggesting that the histidine residue could play a functional or at least an auxiliary role in the stabilization of $Trp_3H^{\bullet+}$ and thereby in the photoreduction of plant (6–4) PLs.

3.2.2 Mutation of His382 to Ser in At64 decelerating the photoreduction in vitro and impairing the photorepair capability in bacterial cells

To examine whether the His/Ser difference affects FAD photoreduction via the Trp-triad, I investigated steady-state photoreduction kinetics for the H382S mutant of *At*64 (*At*64-H382S), as previously performed[30] for the wild-type of *At*64 (*At*64-WT). *At*64-H382S was illuminated with >430

nm light in the presence of an external reductant under anaerobic conditions and the UV/Vis absorption spectral changes were monitored. Upon light illumination, the absorption band at 450 nm characteristic to FAD_{ox} decayed and the spectra were gradually converted to that of $FADH^-$ (via transient accumulation of small amounts of $FADH^{\bullet}$, as indicated by the absorption growth and decay between 500 and 700 nm; Figure 3a). Fitting the normalized absorption at 450 nm (A_{450}) with a monoexponential decay function revealed that FAD photoreduction in *At*64-H382S occurred with a half-life ($t_{1/2}$) of 222 ± 4 s, which is about 10-fold slower than that in *At*64-WT[30] ($t_{1/2}$ = 21.6 ± 0.5 s) under the same conditions (Figure 3b). To examine whether the less efficient photoreduction caused by the H382S mutation affects the (6–4) PP photorepair activity of *At*64, UV-sensitive *E. coli* SY32 cells, in which CPD lesions can be repaired due to a rescue plasmid coding *E. coli* CPD PL gene, were transformed with an *At*64-H382S expressing plasmid, in the same way as previously reported[30]. The survival rate was found to be about 10-fold lower in H382S than in WT (Figure 3c). These results indicate that the H382S mutation in *At*64 impairs the (6–4) PP photorepair in bacterial cells by hampering the preceding (and necessary) photoreduction reaction.

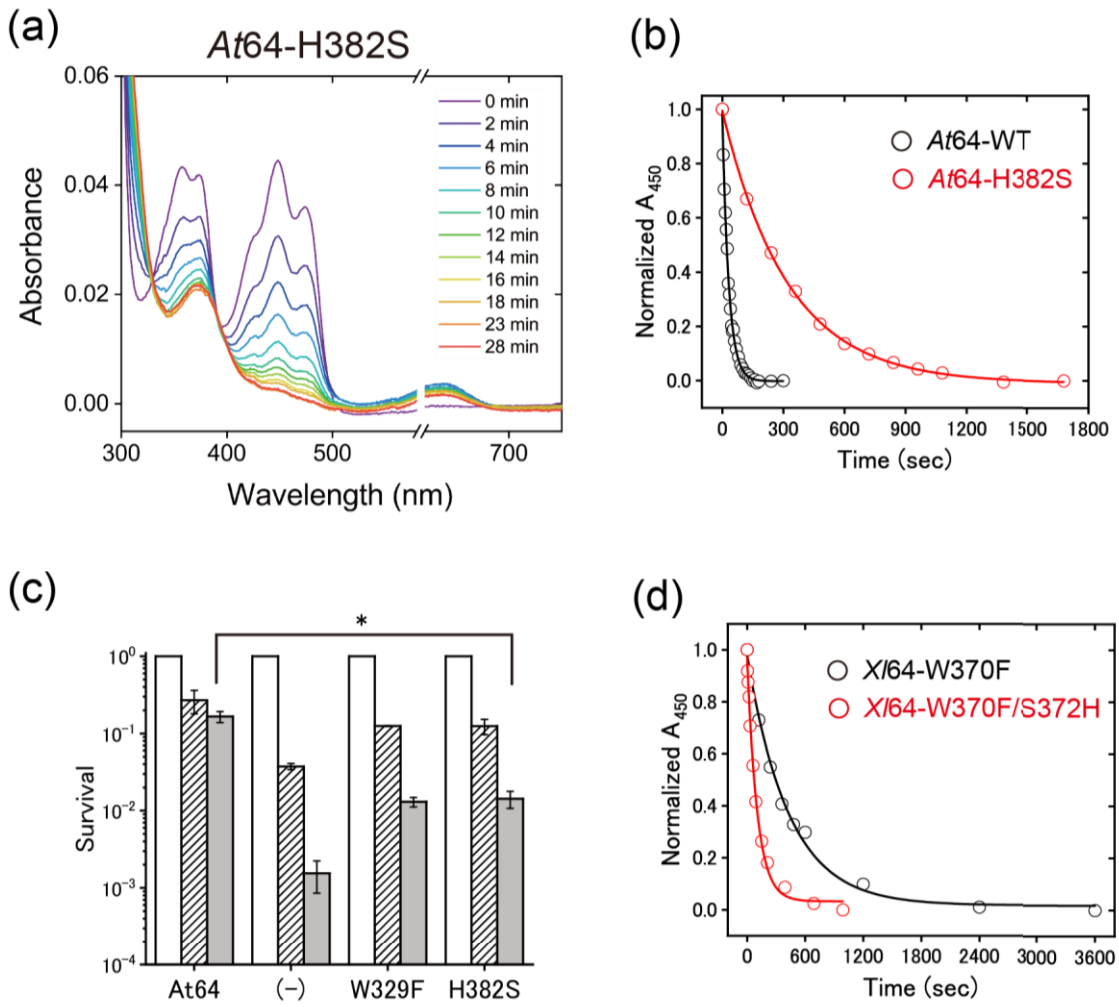

Figure 3. The influence of His→Ser and Ser→His substitutions on the photoreduction of and photorepair by *At*64 and *Xl*64, respectively. (a) Evolution of absorption spectra upon FAD photoreduction in *At*64-H382S. The H382S mutant exhibited the typical spectral changes from FAD_{ox} to $FADH^-$ upon white-light (> 430 nm) illumination with 5 mM of cysteine under anaerobic condition. Data between 580 and 620 nm are omitted due to an irreproducible bump in the region produced by instrumental problems. (b) Comparison of the decay of normalized A_{450} reflecting the FAD photoreduction in *At*64-WT and *At*64-H382S. Measured data points (empty circles) are fitted with monoexponential decay functions (solid lines). (c) (6–4) PP photorepair activity assay for *At*64 variants in *E. coli* cells. Survivals of the cells transformed with the plasmids encoding WT or mutants of *At*64 or an empty vector (annotated as (-)) upon 0 J m^{-2} (open bar), 0.3 J m^{-2} (shaded bar), and 0.6 J m^{-2} (grey bar) UV irradiation, followed by white light for 30 min. The W329F mutant is the mutant lacking Trp_3H. The experiments were performed in triplicates (n = 3) and the statistical significance was analyzed with a *t*-test, where the significance cutoff value was set to 0.05, and the asterisk indicates the P value of 0.0035. (d) The decay kinetics of normalized A_{450} in the *Xl*64-W370F and *Xl*64-W370F/S372H mutants showing that the S372H mutation in *Xl*64-W370F enhances the photoreduction efficiency in *Xl*64 lacking Trp_4H.

In the previous study[29] on FAD photoreduction in *Xl*64 containing a Trp-tetrad, the mutation of Trp_4H in *Xl*64 to Phe (*Xl*64-W370F) showed a comparatively slow photoreduction kinetics under the same conditions (Figure 3d, $t_{1/2}$ = 297 ± 19 s). Interestingly, the W370F/S372H double mutant of *Xl*64 (*Xl*64-W370F/S372H), which mimics the circumstance of the Trp-triad in *At*64, exhibited ~4-fold faster ($t_{1/2}$ = 73 ± 4 s) photoreduction kinetics than *Xl*64-W370F (Figure 3d), illustrating that the introduction of the His residue elevated the photoreduction capability via the Trp-triad in *Xl*64 lacking Trp_4H. Together, these results suggest that the His residue next to Trp_3H does indeed play an important role in the FAD photoreduction via the Trp-triad.

3.2.3 Photoreduction experiments on other His382 mutants

In general, His residues play a variety of roles in biological functions based on their polarity[31], acid-base properties[32], and the planarity/aromaticity[33]. To identify which feature of His382 in *At*64 controls the photoreduction via the Trp-triad, various His382 mutants were subjected to the photoreduction experiment. Although some mutants could not be isolated (presumably due to the loss of the structural integrity), I successfully purified the H382D, H382N, H382V and H382Y mutants of *At*64 without any apparent structural or functional perturbations as confirmed by their typical spectral changes during the photoreduction process (Figures 4a, b, c, and d). Their photoreduction kinetics were found to be 4.3, 3.3, 2.4, or 1.6-fold slower than *At*64-WT for the H382D, H382N, H382V, or H382Y mutant, respectively ($t_{1/2}$ = 92 ± 5 s for H382D, $t_{1/2}$ = 71 ± 4 s for H382N, $t_{1/2}$ = 53 ± 5 s for H382V, $t_{1/2}$ = 34 ± 3 s for H382Y, Figure 4e).

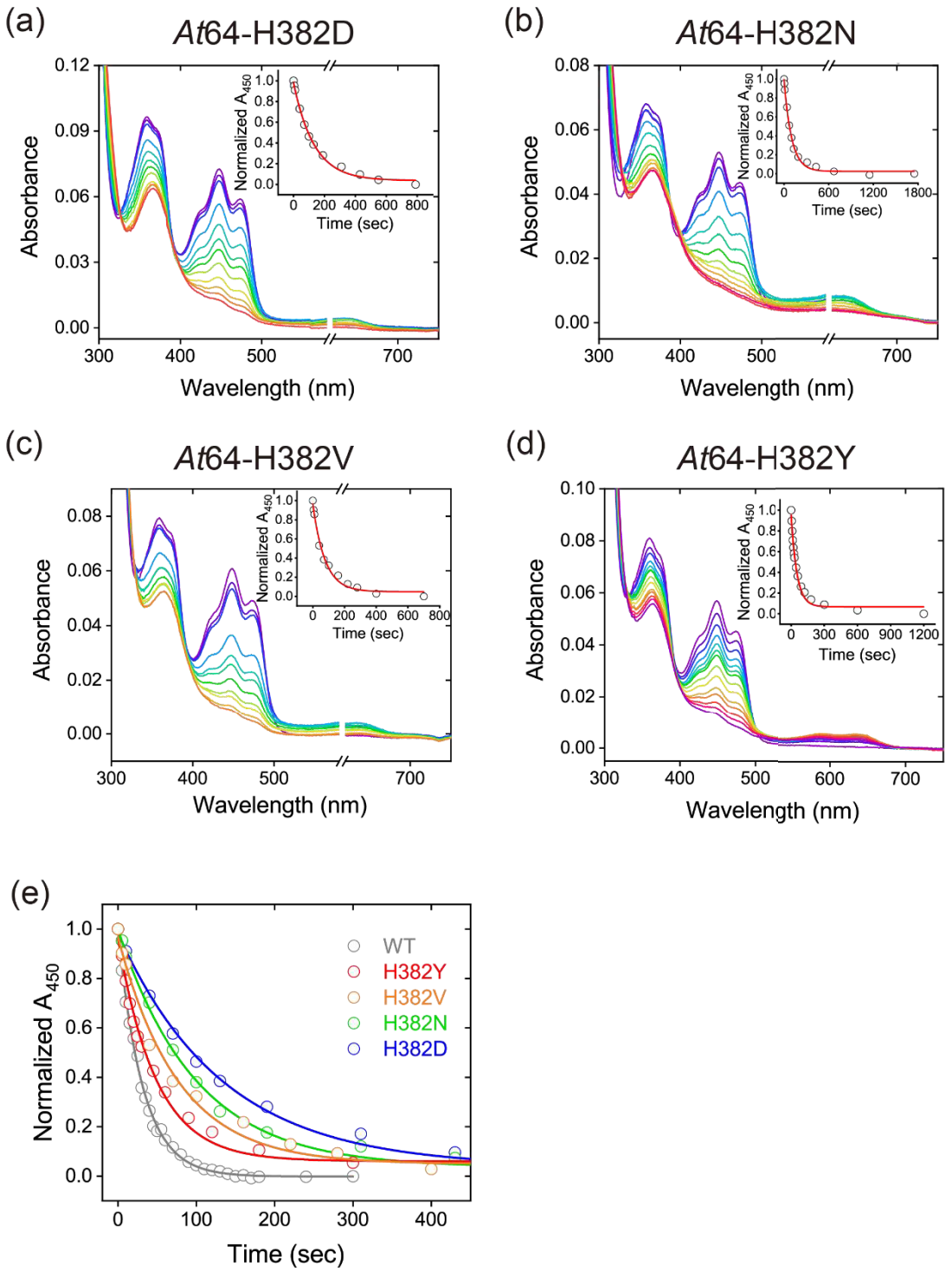

Figure 4. Photoreduction of FAD in His382 mutants of *At*64. (a, b, c, and d) Evolution of absorption spectra upon FAD photoreduction in the (a) H382D, (b) H382N, (c) H382V, and (d) H382Y mutants of *At*64. The plots of normalized A_{450} against time are reasonably well fitted with monoexponential functions as shown in the insets. Data between 580 and 620 nm for (a), (b), and (c) are omitted due to an irreproducible bump in the region produced by instrumental problems. (e) FAD photoreduction kinetics for H382Y (red), H382V (orange), H382N (green), and H382D (blue) *At*64 mutants reflected by the decay of normalized A_{450} values compared to WT (grey).

The slowest photoreduction kinetics of H382D among the tested mutants indicates that the capacity of His382 to act as a proton acceptor for $Trp_3H^{\bullet+}$ is likely not required to improve the photoreduction efficiency. The faster kinetics of H382V *vs.* that of H382N indicates that increased polarity near Trp_3H is not beneficial either. The most similar kinetics to *At*64-WT was observed for the H382Y mutant. This result suggests the possibility that the planarity/aromaticity or just plain bulkiness of the His and Tyr residues might be the key factor that boosts the photoreduction efficiency. Interestingly, the His→Tyr substitution is found in (6–4) PL orthologues from primitive plants such as *Lycopodiopsida* and *Bryophyta* (Blast-p search showed that the His residue is conserved among 95% of plant (6–4) PL orthologues and the rest has a Tyr residue in this position, Figure. 2b). Altogether, the photoreduction experiments on the His382 mutants suggest that small and polar residues are not good alternatives to His382 and that the proton-accepting ability and/or polarity of His382 are not required to make the FAD photoreduction in *At*64 efficient.

3.2.4 Molecular dynamics simulations suggesting the regulated solvation of Trp_3H in At64

Given the observations that FAD photoreduction in *At*64 significantly slowed down upon mutation of His382 in *At*64 to relatively compact and polar residues (Ser, Asn, and Asp), I considered the possible involvement of solvation of Trp_3H in the photoreduction. To evaluate the solvation, I performed molecular dynamics (MD) simulations for the His382 mutants in the same way as previously reported[30], and analyzed the presence of water molecules around the Trp_3H in the last 100 ns of the production runs. The area within 3.4 and 5.0 Å of the nitrogen atom of the Trp_3H indole ring

as was defined as the first (HS1) and the second (HS2) hydration shell, respectively (Figure 5a). Because bulk water molecules could come into HS1 through HS2 and HS2 could be susceptible to the mutation of His382, I first counted the number of water molecules in HS2 in each frame. As expected, the water molecule distribution in HS2 demonstrated that the replacement of His382 by Ser, Asn, and Asp residues resulted in an increased solvation of Trp_3H compared to Val, Tyr, and His residues (Figure 5b). To examine the influence of the solvation in HS2 on that in HS1, I also analyzed the water molecule distribution in HS1 (Figure 5c), showing a clear difference between the WT protein and all the His mutants. Indeed, WT exclusively bore only one water molecule in HS1 in the course of the simulation time, while the mutants could have more than two molecules in a frame. In the previous chapter, I described that a water molecule was stably captured proximal to Trp_3H during a MD simulation for WT (WAT1 in Figure 5a), and that the mutation of Ser412 (hydrogen-bonding to WAT1) to Ala significantly reduced the photoreducibility of *At*64[30]. As WAT1 is located in HS1, the observed single water molecule in the water molecule distribution in HS1 is assigned to be WAT1. It is conceivable that the mutation of His382 alters the coordination of WAT1, however, as shown in Figure 5d, the distance between the oxygen atom of WAT1 and the nitrogen atom of the indole ring of Trp_3H ($d_{O\cdots N^1}$) during 100 ns simulation time for all the mutants was approximately the same as in WT. This result suggests that the mutation of His382 does not significantly affect the WAT1 coordination and that another structural aspect is likely engaged in the fine-tuning effect of His382.

(a)

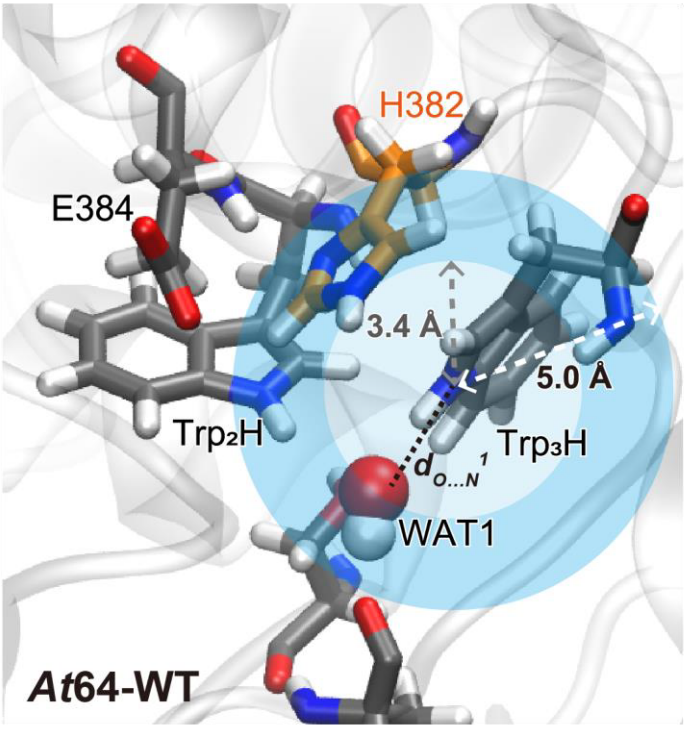

(b)

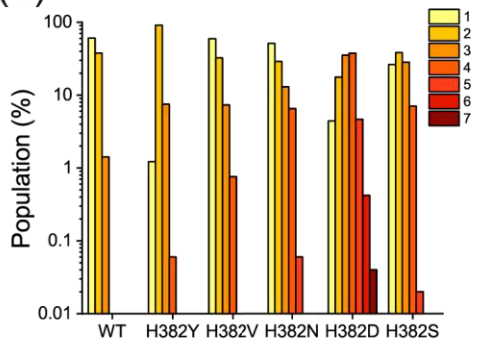

(c)

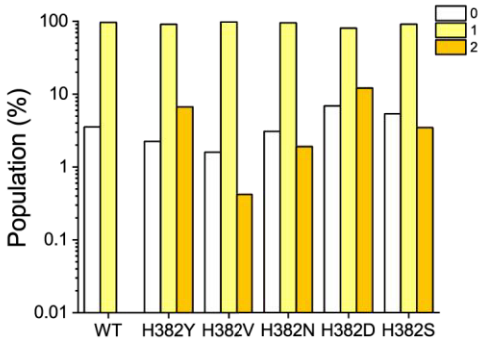

(d)

	$d_{O...N}^{1}$ (Å)
*At*64 (WT)	3.04 ± 0.19
H382Y	3.01 ± 0.17
H382V	2.98 ± 0.15
H382N	3.02 ± 0.17
H382D	3.10 ± 0.25
H382S	3.06 ± 0.20

(e)

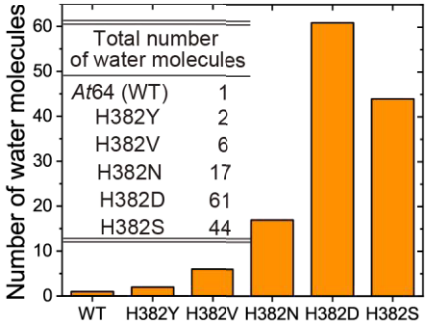

Figure 5. Trp_3H solvation in WT *At*64 and its His382 mutants in MD simulations. (a) A snapshot of the WT structure. The first (HS1) and the second (HS2) hydration shell of the nitrogen atom of the Trp_3H indole ring is colored in light and dark blue, respectively. (b) Number of water molecules in HS2 (within 5.0 Å of the nitrogen atom of the Trp_3H indole ring) for WT and mutant *At*64 proteins. The number of water molecules within HS2 in a frame are counted over all the frames. (c) Water molecules distribution in HS1 (within 3.4 Å of the nitrogen atom of the Trp_3H indole ring) for *At*64 variants. The numbers of water molecules within HS1 in a frame are averaged over all the frames. (d) The distance between the oxygen atom of WAT1 and the nitrogen atom of the indole ring of Trp_3H ($d_{O...N}^{1}$ in Figure 5a) during 100 ns simulation time for WT *At*64 and its H382 variants. (e) Total numbers of the respective water molecules coming in and out HS1 over the 100 ns simulation time window.

Thus, I hypothesized that the presence and/or behavior of the additional water molecules (other than WAT1) in HS1 could affect the photoreduction in the His382 mutants of *At*64. To explore the dynamic behavior of water molecules, I counted the total numbers of the water molecules coming in and out of the HS1 during the 100 ns simulation, by tracing the ID of the water molecules (Figure 5e). The results clearly show that there is a tendency that mutants with better water accessibility to HS1 are more difficult to photoreduce. As described above, WAT1 was the only water present in HS1 of WT, suggesting that His382 would play a role in preventing water access to Trp_3H. Interestingly, the result for the H382Y mutant, which exhibited the similar photoreduction kinetics to WT (Figure 4e), indicated that only one additional water molecule (WAT2) came into and out of HS1, and that other randomly moving water molecules outside HS1 did not enter HS1. Noteworthy, WAT2 in H382Y has been captured at the position corresponding to the place occupied by His382 in WT during the simulation time (Figure 6). The limited access of random water molecules into HS1 in H382Y (Figure. 5e) suggested that WAT2 prevents other water molecules from approaching Trp_3H, in a similar way to His382 in WT. In summary, the MD simulation and photoreduction experiments indicate that a more solvent-accessible environment around Trp_3H in the H382S, H382N, and H382D mutants could have a negative impact on their photoreduction, while the photoreduction of *At*64-WT and H382Y seems to be enhanced by regulating the solvent access to Trp_3H.

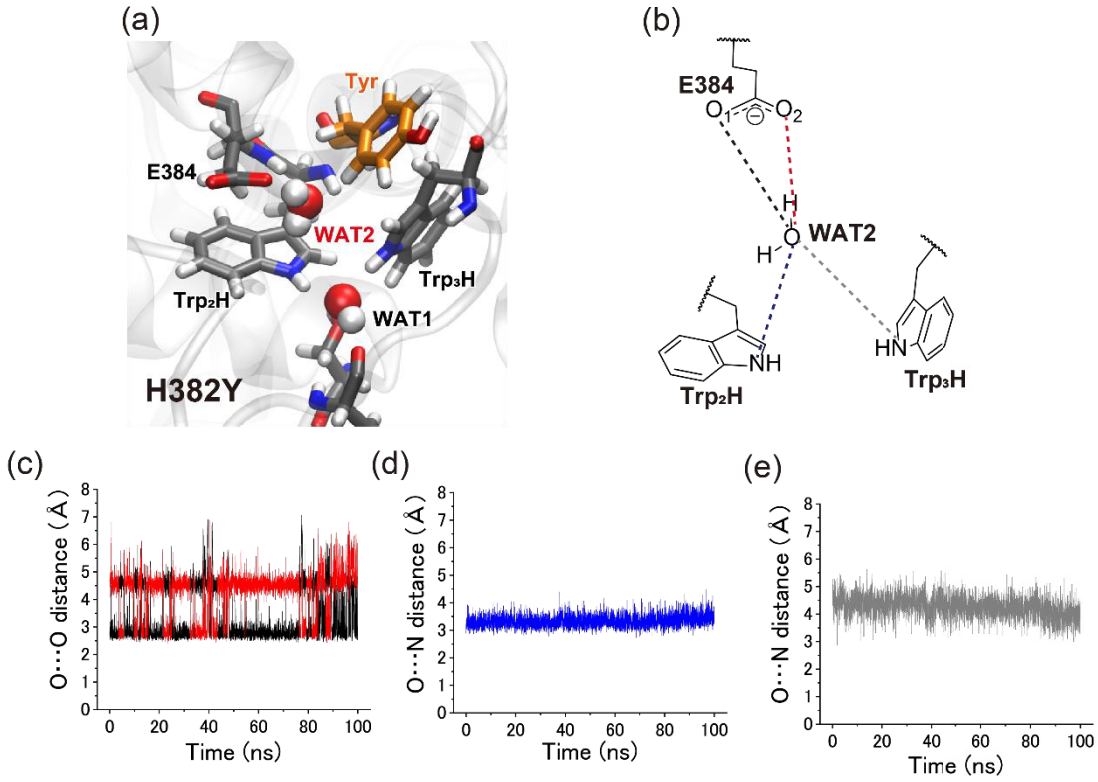

Figure 6. Orientation of the stably captured water molecule (WAT2) in H382Y *At*64. (a) A snapshot from the MD simulation for H382Y. (b) A schematic view of WAT2 recognition site. (c) The time development of the distance between the O_1 / O_2 atoms of the E384 side chain and the O atom of WAT2 plotted in black / red. (d) The time development of the distance between the O atom of WAT2 and the N atom of Trp_2H plotted in blue. (e) The time development of the distance between the O atom of WAT2 and the N atom of Trp_3H plotted in gray.

3.2.5 Transient absorption spectroscopy on ns–µs timescales revealing that the regulated solvent accessibility impedes $Trp_3H^{\bullet+}$ deprotonation in At64-WT

In order to further clarify the effects of mutations on the fate of the photoinduced $FAD^{\bullet-}$ $Trp_3H^{\bullet+}$ radical pair in *At*64, transient absorption spectroscopy in the ns-to-µs regime, where $Trp_3H^{\bullet+}$ deprotonation and/or $FAD^{\bullet-}$ $Trp_3H^{\bullet+}/Trp_3^{\bullet}$ charge recombinations are typically observed in PCSf proteins, were employed for WT and the least photoreducible mutant H382S (Figures 7a and b). Based on the reference absorption spectra of the expected photoinduced species[21] (Figure 7c), the photoreaction was followed at two selected wavelengths: at 457 nm, which is close to the maximum

of the expected bleaching of the FAD_{ox} absorption band (due to its reduction to $FAD^{\bullet-}$) and where the Trp radicals do not contribute much to the absorption change; and at 562 nm, which is close to one of the two maxima of the $TrpH^{\bullet+}$ absorption band and where the absorption changes due to FAD_{ox} reduction to $FAD^{\bullet-}$ (and subsequent reoxidation upon radical pair recombination) are expected to be relatively small.

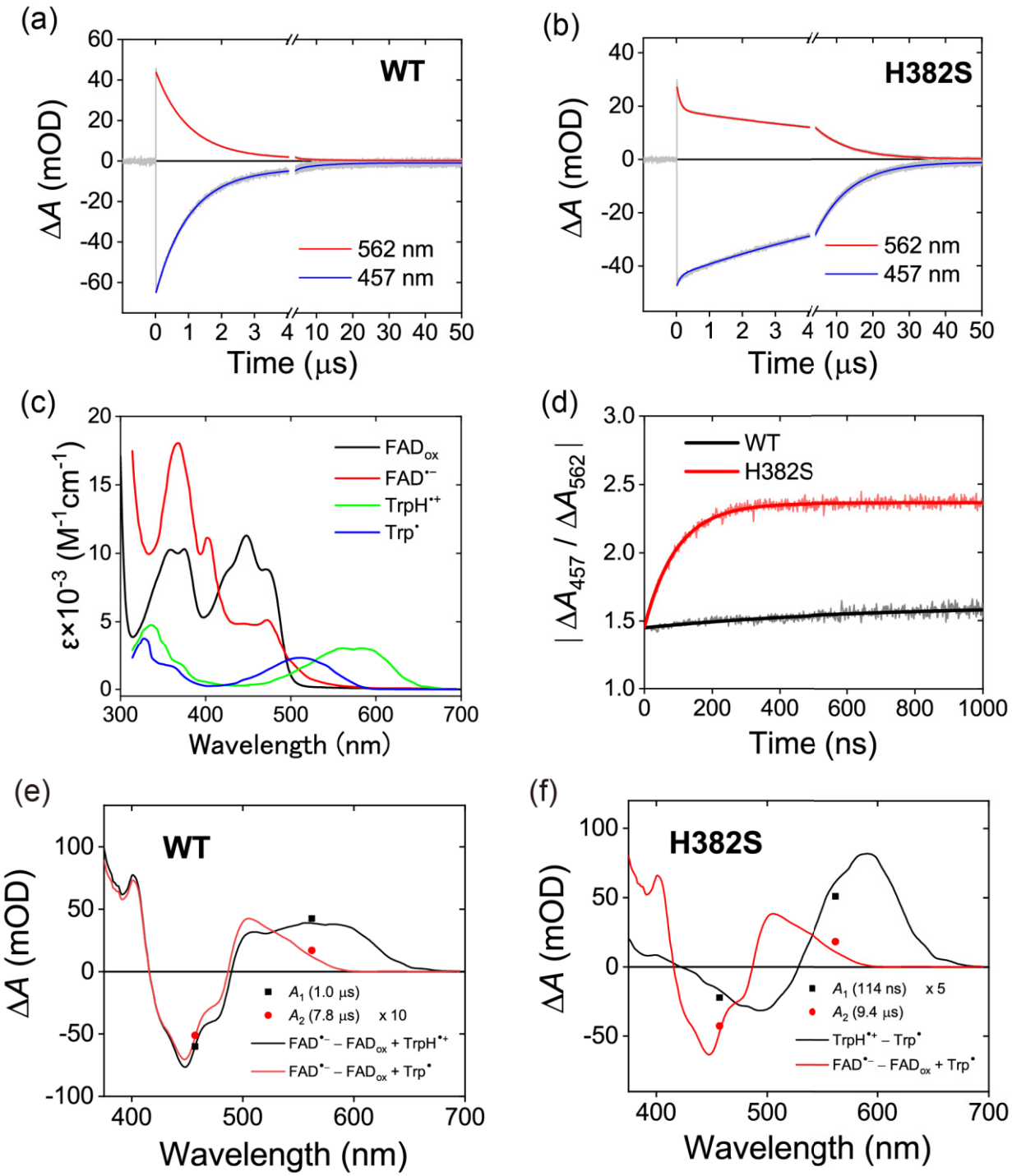

Figure 7. Transient absorption spectroscopy of WT and H382S *At*64 on a ns/μs timescale. Two representative wavelengths were chosen to follow the fate of the flavin and the Trp species separately: 457 nm, where the signal reflects mainly the FAD_{ox} absorption bleach due to its flash-induced reduction to $FAD^{\bullet-}$ and the subsequent recovery of FAD_{ox}, and 562 nm, where the major contribution to absorption changes should come from the formation and decay of $TrpH^{\bullet+}$ / $Trp^{\bullet}$ species. The recorded signals are shown in panels a) and b) in grey, results of their biexponential global fits are shown in blue (for 457 nm) and in red (for 562 nm). (a) Flash-induced absorption changes for ~125 μM *At*64-WT. (b) Flash-induced absorption changes for ~95 μM *At*64-H382S. (c)

Reference absorption spectra of FAD and Trp species expected to contribute to light-induced absorption changes in *At*64. Spectra are taken from the literature[21]. (d) Absolute value of the ratio of the 457 nm to the 562 nm signals for WT and H382S *At*64. Both traces begin at ~1.5, suggesting that the nature of the flash-induced radical pair is the same in both proteins at time zero. The factor of ~1.5 is consistent with the formation of $FAD^{\bullet-}$ $TrpH^{\bullet+}$ pairs. While this ratio changes only slightly and slowly in the WT protein (in line with $FAD^{\bullet-}$ $TrpH^{\bullet+}$ recombination being the major process), the ratio evolves dramatically in the H382S mutant (with τ ~100 ns), mainly due to the rapid decay phase in the 562 nm signal. Increase of this ratio suggests that $TrpH^{\bullet+}$ is transformed into $Trp^{\bullet}$, which absorbs less than $TrpH^{\bullet+}$ at 562 nm. (e and f) Superimposition of the phase amplitudes obtained from the biexponential fits of the transient absorption changes for (e) WT and (f) H382S *At*64 with the expected difference spectra (lines) reflecting the main underlying processes of the given kinetic phases (recombinations of the $FAD^{\bullet-}$ $TrpH^{\bullet+}$/$Trp^{\bullet}$ radical pairs to FAD_{ox} + TrpH (TrpH does not absorb in the shown region) and/or $TrpH^{\bullet+}$ deprotonation to $Trp^{\bullet}$).

Upon excitation by ~5 ns flashes at 480 nm, bleaching at 457 nm and absorption increase at 562 nm with the same initial ratio of the two signals of ~ –1.5 : 1 in both protein samples were induced, followed by a decay of all signals to zero within less than 50 µs (Figures 7a and b), suggesting that all photoinduced radicals recombined in this time window. However, the signal decays were markedly different in the two proteins: while the decay of the WT signals at both wavelengths was essentially monoexponential with a time constant τ_1 of ~1 µs and the signal ratio was changing only very little (indicating that charge recombination was the major process; according to the fit, traces of a slower τ_2 ~8 µs process amounting to less than 10% of the signal amplitudes were present), the decay of the H382S signals was clearly biexponential, with τ_1 of ~100 ns and τ_2 of ~9.5 µs. The ~100 ns phase was particularly visible at 562 nm and much less so at 457 nm, considerably changing the amplitude ratio of the two signals (see Figure 7d) and suggesting that the major underlying process of this phase was the deprotonation of $TrpH^{\bullet+}$ to $Trp^{\bullet}$, possibly with a bit of $FAD^{\bullet-}$ $TrpH^{\bullet+}$ recombination in parallel.

The initial ratio of the signal amplitudes at 457 and 562 nm of ~ –1.5 : 1 is consistent with the formation of $FAD^{\bullet-}$ $TrpH^{\bullet+}$ radical pairs in both proteins. In *At*64-WT, over 90% of these radical pairs seem to recombine directly with a time constant of ~1 µs (the amplitudes of this phase are in a good agreement with the difference spectrum of $FAD^{\bullet-}$ – FAD_{ox} + $TrpH^{\bullet+}$, see Figure 7e) and the $TrpH^{\bullet+}$ cation radicals seem to deprotonate in parallel in less than 10% of pairs, which then decay in ~8 µs. Indeed, the amplitudes of this minor phase fit well the difference spectrum of $FAD^{\bullet-}$ – FAD_{ox} + $Trp^{\bullet}$ (Figure 7e). In *At*64-H382S, the situation is markedly different. Since the $TrpH^{\bullet+}$ cation radicals rapidly deprotonate within the first ~100 ns kinetic phase (the amplitudes of this phase are consistent with the $TrpH^{\bullet+}$ – $Trp^{\bullet}$ difference spectrum, see Figure 7f), only a very small fraction of $FAD^{\bullet-}$ $TrpH^{\bullet+}$ pairs recombines directly (in competition with the fast deprotonation). The fraction of the remaining $FAD^{\bullet-}$ $Trp^{\bullet}$ pairs (Figure 7f) is hence much larger in H382S than in the WT protein. Nevertheless, the lifetimes of the $FAD^{\bullet-}$ $Trp^{\bullet}$ pairs are comparable in both proteins (~8 µs in WT *vs.* ~9.5 µs in H382S). Given that the ~1 µs $FAD^{\bullet-}$ $TrpH^{\bullet+}$ decay phase in WT reflects ~90% recombination and ~10% $TrpH^{\bullet+}$ deprotonation, the intrinsic time constant for $TrpH^{\bullet+}$ deprotonation is ~10 µs in this protein. This means that while the H382S mutation has virtually no impact on the lifetime of the $FAD^{\bullet-}$ $Trp^{\bullet}$ pairs (see above), it accelerates the $TrpH^{\bullet+}$ deprotonation by a factor of ~100 (from ~10 µs in WT to ~100 ns in H382S) and shortens the lifetime of the $FAD^{\bullet-}$ $TrpH^{\bullet+}$ pairs by a factor of ~10 (from ~1 µs in WT to ~100 ns in H382S). As far as I know, $Trp_3H^{\bullet+}$ deprotonation in *At*64 in ~10 µs is the slowest terminal $TrpH^{\bullet+}$ deprotonation rate ever reported for a WT PCSf protein (the second-slowest being the $Trp_4H^{\bullet+}$ deprotonation in *Xl*64 in ~2.5 µs under very similar conditions[21]).

The energy of the excitation pulses was also estimated using the $[Ru(bpy)_3]^{2+}$ actinometer[34], to calculate the quantum yield of the photoinduced $FAD^{\bullet-}$ $TrpH^{\bullet+}$ pairs detected at 'time zero' of the experiment, *i.e.*, pairs that had not been lost due to ultrafast recombination processes faster than the time resolution (*i.e.* ~5 ns, limited by the excitation pulse length). The yield of the detected $FAD^{\bullet-}$ $TrpH^{\bullet+}$ radicals seems to be slightly higher than 80% in *At*64, which means that the losses due to ultrafast $FAD^{\bullet-}$ $TrpH^{\bullet+}$ recombination are lower than 20%.

3.3 Discussion

3.3.1 Limited solvation of Trp_3H for productive photoreduction of FAD in At64

Upon photoactivation, *A. thaliana* (6–4) photolyase exhibits by far the slowest (~10 µs) deprotonation of the terminal $TrpH^{\bullet+}$ cation radical of all PCSf proteins studied to date. In the absence of extrinsic reductants *in vitro*, the consequence of this slow deprotonation rate is that most (~90%) of the photoinduced $FAD^{\bullet-}$ $Trp_3H^{\bullet+}$ radical pairs recombine as such (in ~1 µs) and the remaining ~10% of $FAD^{\bullet-}$ $Trp_3^{\bullet}$ pairs (in which $Trp_3H^{\bullet+}$ has been deprotonated) recombine in ~8 µs. Putting the ~10× faster FAD photoreduction in *At*64-WT (than in H382S) *in vitro* (Figure 3b) and the ~10-fold higher survival rate of WT-expressing *E. coli* cells in the repair activity assay (compared to cells expressing *At*64-H382S; Figure 3c) into context with these results, it seems that the extrinsic reductants act much more easily upon $TrpH^{\bullet+}$ than upon $Trp^{\bullet}$, both *in vitro* and *in vivo*. This is likely because $TrpH^{\bullet+}$ reduction requires a mere ET, while $Trp^{\bullet}$ reduction requires transfer of not just an electron but also of a proton (or of a hydrogen atom $H^{\bullet}$) and because ET can occur over longer

distances than the transfer of a proton or of a hydrogen atom can. In any case, formation of a much greater fraction (compared to WT) of the longer-lived $FAD^{\bullet-}$ $Trp^{\bullet}$ pairs in H382S does not seem to be able to compensate to any visible extent for the ~10× shortened lifetime of the $FAD^{\bullet-}$ $TrpH^{\bullet+}$ pairs in this mutant. The slow deprotonation of the terminal tryptophan cation radical and the consequently extended lifetime of the $FAD^{\bullet-}$ $Trp_3H^{\bullet+}$ pair (and likely also that of the $FADH^{-}$ $Trp_3H^{\bullet+}$ pair in the second photoactivation step) considerably enhance the propensity of *At*64 to photoactivation – by providing more time to the extrinsic reductant to quench $Trp_3H^{\bullet+}$ and thereby stabilize the reduced flavin by preventing recombination with its radical counterpart.

Searching for the cause of the unusually slow $Trp_3H^{\bullet+}$ deprotonation, I identified a neighboring histidine residue, which is highly conserved in plant (6–4) PLs (His382 in *At*64 numbering), and the mutation of which (to diverse alternative residues – Tyr, Val, Asn, Asp and/or Ser) indeed had a significant negative effect on the rate of *At*64 photoactivation *in vitro*. In the case of the *in vivo*-tested (and the least *in vitro*-photoactivatable) H382S mutant, the mutation also had a dramatically deleterious impact on the survival of UV-irradiated and Vis-reactivated *E. coli* cells, suggesting that the His382 residue next to the terminal (3rd) tryptophan likely plays an important role also in the *in-vivo* photoactivation of *At*64 via the Trp chain.

According to the MD simulations, the native His382 blocks access of solvent molecules to the nitrogen atom of $Trp_3H^{\bullet+}$ in *At*64 (Figure 8), and it does so much more efficiently than any alternative amino acid in the tested mutants. In the WT protein, the only water molecule interacting with $Trp_3H^{\bullet+}$, referred to as WAT1 in this text, is tightly coordinated by other amino acids within *At*64.

It never leaves the first hydration shell of the nitrogen atom of $Trp_3H^{\bullet+}$ and it does not interact with the bulk buffer enough to provide a functional channel for a proton transfer from $Trp_3H^{\bullet+}$ to the buffer.

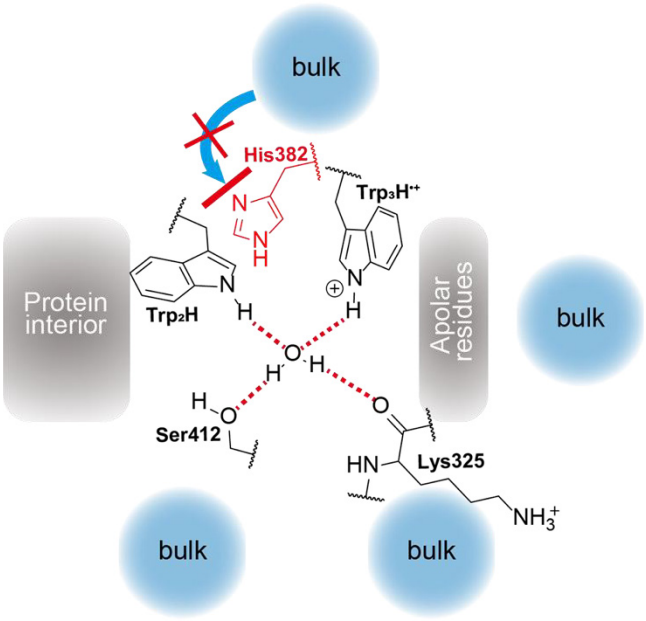

Figure 8. Schematic model showing how the surroundings of $Trp_3H^{\bullet+}$ prevent the proton release to the solvent. The nitrogen atom of $Trp_3H^{\bullet+}$ is encircled by the coordinated water molecule WAT1, non-polar residues (including I327 and F380 shown in Figure 2), and His382 (highlighted in red). WAT1 does not interact with and cannot escape to the bulk because it is fully restrained by the hydrogen bond interactions (indicated by dashed red lines) with the residues of the surrounding protein.

3.3.2 Unexpectedly high yields of the photoinduced $FAD^{\bullet-}$ $TrpH^{\bullet+}$ radical pair in At64

Finally, the efficiency of *At*64 photoactivation is further enhanced by exceptionally low losses (< 20%) due to ultrafast (< 5 ns) recombination of the photoinduced $FAD^{\bullet-}$ $Trp_1H^{\bullet+}$ and/or $FAD^{\bullet-}$ $Trp_2H^{\bullet+}$ radical pairs. This is significantly less than in any other PCSf protein studied so far. For comparison, in *E. coli* CPD PL ~35% of the photoinduced radical pairs are lost within the first few ns[35], in *Chlamydomonas reinhardtii* animal-like CRY it is ~50%[25], in *Xl*64 ~75%[21], and in *At*CRY

80 to 95%, depending on the presence or absence of ATP[17]. In *Dinoroseobacter shibae* NewPHL, which is an ancestral PL containing a mere Trp dyad, as much as ~90% of the photoinduced radical pairs are lost within the first few nanoseconds and most of the remaining ~10% pairs recombine within the next ~50 ns[36]. Interestingly, the structural comparison between *At*64 and *Xl*64 does not show any remarkable difference in the residues within 4 Å of FAD and Trp_1H (Figure 9a), but the residues around Trp_2H are different. Notably, an arginine residue (Arg387) is located near Trp_2H in *At*64, which is replaced with glutamine (Gln377) in *Xl*64 (Figure 9a). This arginine is highly conserved in plant (6–4) PL orthologues but is never found in any animal (6–4) PL (Figures 9b and c). The positively-charged guanidinium moiety of Arg387 could destabilize the localization of the hole on Trp_2H and accelerate the successive electron transfer from Trp_3H, leading to the ultrafast charge separation between FAD and Trp_3H and low recombination losses. This hypothesis will be addressed by future experimental and computational studies.

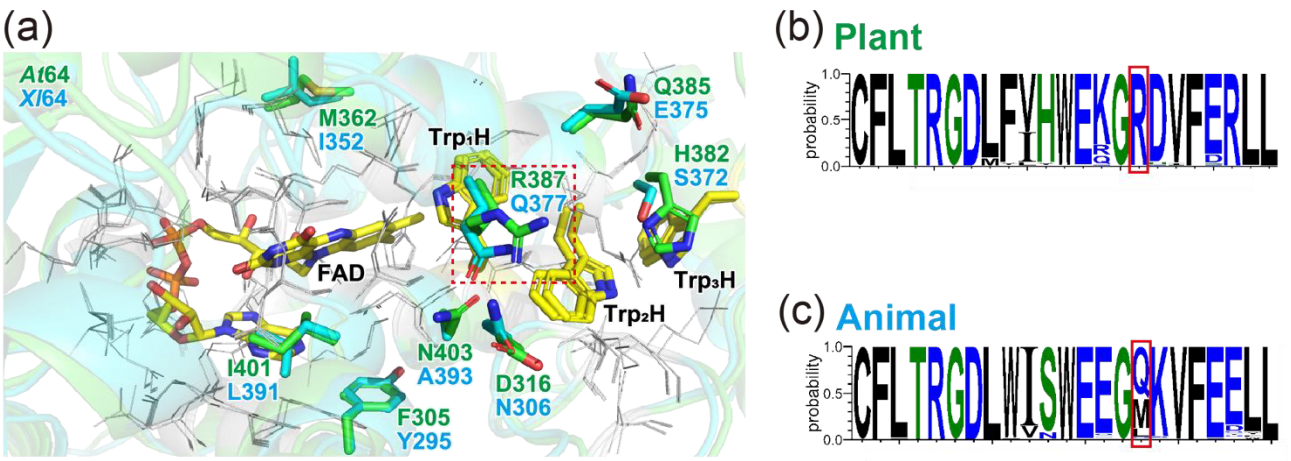

Figure 9. Primary and tertiary structural analyses of the environment of the electron-transferring chain in plant and animal (6–4) PL orthologues. (a) The three-dimensional structures of *At*64 and *Xl*64 are superimposed. The residues within 4 Å of FAD, Trp_1H, and Trp_2H are shown, and the white-grey colored residues in lines are conserved between *At*64 and *Xl*64. Residues unique to *At*64 and *Xl*64 are colored in green and cyan, respectively. Differences in the residues in the red dashed frame (R387 in *At*64 and Q377 in *Xl*64) could have an impact on the $FAD^{\bullet-} \cdots TrpH^{\bullet+}$ charge separation along the respective ET chains. (b and c) Primary structural analyses of (b) plant and (c) animal (6–4) PL orthologues. The residues in the red frame correspond to R387 in *At*64 and Q377 in *Xl*64.

3.4 Methods

Plasmid construction

For the (6–4) PP repair activity assay in bacterial cells[29,37,38] and protein production, pGEX-4T-1 and pET28a(+) plasmids that produce the (6–4) PLs were constructed, respectively. First, the desired mutations (W329F and H382S) of *At*64 were introduced into the pGEX-4T-1 plasmid carrying the *At*64-WT gene[29] with the QuikChange Site-Directed Mutagenesis Kit. The PCR primers used for the mutagenesis are shown in Table 1 (Entry 1 and 4). After sequencing, the obtained plasmids were used for the assay.

The mutant genes in the pGEX plasmids were then amplified and subcloned into the *Nde*I/*Xho*I restriction site of the pET-28a(+) vector with the specific primers as shown in Table 1 (Entry 8). The H382D, H382N, and H382V mutations of *At*64 were also introduced into the pET28a

vector carrying the *At*64-H382S gene by the QuikChange Site-Directed Mutagenesis kit (Table 1, Entry 2, 3, and 5). As for the H382Y mutant, the 5' upstream and 3' downstream of the mutation site were separately amplified using the primers shown in Table 1 (Entry 6), and the amplicons were fused into the pET-28a(+) vector linearized with the *Nde*I and *Xho*I treatment, by using the In-fusion HD Cloning Kit (Takara). The S372H mutation of *Xl*64 was introduced into the pET28a(+) vector carrying the reported *Xl*64-W370F gene[29] using the In-fusion HD Cloning kit with the specific primers shown in Table 1 (Entry 7). The obtained plasmids were sequenced and used for the protein production.

Table 1. Primers for PCR amplification.

Entry		Description		Sequence*
1		W329F	Forward	5′-TGCAAACAGATTCCATTCAACGAGGATCAT-3′
			Reverse	5′-ATGATCCTCGTTGAATGGAATCTGTTTGCA-3′
2		H382D	Forward	5′-GGATCTGTTCATAGATTGGGAACAAGGGCG-3′
			Reverse	5′-CGCCCTTGTTCCCAATCTATGAACAGATCC-3′
3		H382N	Forward	5′-GGATCTGTTCATAAACTGGGAACAAGGGCG-3′
			Reverse	5′-CGCCCTTGTTCCCAGTTTATGAACAGATCC-3′
4	*At*64	H382S	Forward	5′-GGATCTGTTCATATCTTGGGAACAAGGGCG-3′
			Reverse	5′-CGCCCTTGTTCCCAAGATATGAACAGATCC-3′
5		H382V	Forward	5′-GGATCTGTTCATAGTTTGGGAACAAGGGCG-3′
			Reverse	5′-CGCCCTTGTTCCCAAACTATGAACAGATCC-3′
6		H382Y	Forward 1 (with *Nde*I site)	5′-CCGCGCGGCAGCCATA TGGCTACTGGATCCGGT-3′
			Reverse 1	5′-CCTTGTTCCCAATATATGAACAGAT-3′
			Forward 2	5′-ATCTGTTCATATATTGGGAACAAGG-3′
			Reverse 2 (with *Xho*I site)	5′-GTGGTGGTGCTCGAGCT ATTTGAGTTTTGGTCGTTG-3′
7	*Xl*64	W370F/ S372H	Forward 1 (with *Nde*I site)	5′-CCGCGCGGCAGCCATAT GAGGCACAATTCCATCCA-3′
			Reverse 1	5′-TTCTTCCCAATGTATGAAGAGGT-3′
			Forward 2	5′-ACCTCTTCATACATTGGGAAGAA-3′
			Reverse 2 (with *Xho*I site)	5′-GTGGTGGTGCTCGAGTTAT TTTTTCTTGAACAATTCTGCC-3′
8	Subcloning primer		Forward (with *Nde*I site)	5′-CCGCGCGGCAGCCATA TGGCTACTGGATCCGGT-3′
			Reverse (with *Xho*I site)	5′-GTGGTGGTGCTCGAGCT ATTTGAGTTTTGGTCGTTG-3′

(6–4) PP repair activity assay in bacterial cells

The *E. coli* SY32 strain (*uvrA*$^{-}$, *recA*$^{-}$, *phr*$^{-}$), in which CPD PL activity is rescued by the pACYC184 plasmid coding *E. coli* CPD PL gene, has been used for (6–4) PP repair activity assay in bacterial cells[30]. SY32 cells were transformed with a pGEX-4T-1 plasmid expressing a (6–4) PL variant and the colonies were selected on Luria broth (LB) agar plates containing tetracycline (10 μg mL^{-1}) and ampicillin (80 μg mL^{-1}). The transformant was cultivated in 1.5 mL of LB medium containing tetracycline and ampicillin at 37°C overnight. The culture was diluted to OD_{600} = 0.5 with an LB medium. The diluted culture was induced with 2.4 μL of 10 mg mL^{-1} isopropyl-β-D-thiogalactoside (IPTG) and shaken at 37 °C for 1 h. The culture was appropriately diluted with phosphate-buffered saline, and 150 μL of aliquots were spread onto LB agar plates containing tetracycline and ampicillin. The plates were irradiated with 20 W UV germicidal lamp (UVL20PH-6, Sen Lights Co Ltd., Osaka, Japan) through metal mesh filters (2.0 μW cm^{-2}, calibrated with a UVX radiometer equipped with a 254 nm probe, UVP, LLC, Upland, CA) for 15 or 30 s to yield a total irradiance of 0.3 or 0.6 J m^{-2}, respectively. The plates were subsequently illuminated with fluorescent lamps (18 W × 4, FL20SSD/18, Toshiba, Tokyo, Japan) for 30 min, and then incubated at 37°C overnight. After incubation, the number of colonies was counted taking into account the dilution percentage. All survival rates were normalized to the number of colonies obtained without UV irradiation. The experiments were independently performed in triplicate (n = 3), and the statistical significance was analyzed with a Student's *t*-test. The significant cutoff value was set to 0.05.

Protein Purification

For purification of *At*64 variants, I modified the previously reported expression and purification protocol[39]. *E. coli* C41 (DE3) /pLysS (Lucigen) cells were transformed with a pET-28a(+) plasmid carrying the (6–4) PLs gene and grown in 2 L of LB medium containing kanamycin (20 μg mL^{-1}) in a 5 L flask with baffles at 37°C. When OD_{600} reached 1.2, the culture was cooled to 25 °C. Protein production was then induced with a final concentration of 0.2 mM IPTG, and the culture was further incubated at 25 °C for 24 h. After harvest, the pellet was frozen by liquid nitrogen and thawed on ice. The cells were resuspended in 40 mL of a lysis buffer (20 mM NaH_2PO_4, 500 mM NaCl, 5% glycerol, pH 7.4 adjusted by KOH, plus 65 mg of lysozyme) and lysed by sonication. The cell lysate was centrifuged, and the supernatant was loaded onto an open column filled with TALON Metal Affinity Resin (Clontech, TaKaRa) equilibrated with the lysis buffer. Proteins non-specifically bound to the resin were washed out with four column volumes of a wash buffer (20 mM NaH_2PO_4, 500 mM NaCl, 10 mM imidazole, 5% glycerol, pH 7.4 adjusted by KOH), and the His-tagged protein was eluted with an elution buffer (20 mM NaH_2PO_4, 500 mM NaCl, 500 mM imidazole, 5% glycerol, pH 7.4 adjusted by KOH). For further purification, the green eluate was loaded onto a HiTrap Heparin HP column (GE Healthcare) and purified with a step gradient of 100 – 500 mM NaCl in a buffer containing 50 mM Tris-HCl and 5% glycerol (pH 8.0). The purified protein was confirmed by 10% SDS-PAGE, and its concentration was measured based on the FAD absorbance at 450 nm using a molar extinction coefficient of 11 300 L mol^{-1} cm^{-1}.

Measurement of steady-state photoreduction kinetics by UV-vis absorption spectroscopy

Steady-state photoreduction for recombinantly-produced proteins was performed under anaerobic conditions as previously described[30]. 70 µL of protein diluted to 20 µM was applied to a Micro Bio-Spin 6 column (BIO-RAD) equilibrated with a reaction buffer (20 mM phosphate, 500 mM NaCl, 10% glycerol, pH 7.5). An aliquot (60 µL) of the eluate was transferred into an anaerobic 10 × 2 × 8 mm (length × width × height) inner volume quartz cuvette (Starna, 16.160-F/4/Q/10 GL 14/2/Z15). After the cuvette was sealed with a screw cap and PTFE-coated silicone and rubber septa, the air inside the cuvette was replaced with nitrogen through the septa. Further preparation was performed in an anaerobic glovebox. The sample was mixed with L-cysteine (the final concentration was 5 mM) and the reaction buffer up to a total volume of 240 µL under anaerobic and dark conditions.

The anaerobic samples were illuminated with continuous light (430 – 800 nm) from a MAX-150 xenon lamp (Asahi Spectra) through the 10 mm × 8 mm window on ice (illumination time varied depending on the sample). After shaking the sample gently, an absorption spectrum was recorded through the 10 mm path by a UV-vis spectrometer Lambda 35 UV-vis spectrometer (PerkinElmer) or V-730 spectrometer (JASCO)]. The absorbance at 450 nm of the obtained spectra was plotted and fitted with a monophasic exponential decay function with the Origin2019 software.

Transient absorption spectroscopy

The proteins were dissolved in a buffer consisting of 50 mM Tris-HCl (pH 8.0), 500 mM NaCl, and 5% glycerol, at final concentrations of ~125 μM for *At*64-WT and ~95 μM for *At*64-H382S. The transient absorption setup has been described in detail elsewhere[21,26,35]. Nd:YAG-pumped optical parametric oscillator (OPO; Brilliant B/Rainbow; ~5 ns, 480 nm, ~2 mJ cm^{-2}) was used as an excitation source. The laser energy was estimated from transient absorption signals using $[Ru(bpy)_3]^{2+}$ as an actinometer[34]. Monitoring light at two selected wavelengths (457 and 562 nm) was provided by continuous-wave lasers (Cobolt Twist™ and Oxxius 561–25-COL-002, respectively). The measuring light was perpendicular to the excitation laser beam and passed through the sample along the 10-mm path of a 2 × 2 × 10 mm (W × H × L) quartz cell with self-masking solid black walls (Starna). Flash-induced changes of the transmission of the sample were monitored behind the sample by a Si photodiode (Alphalas UPD-500-UP, <500 ps rise time) coupled to a Tektronics MSO 64 digital oscilloscope with bandwidth limit set to 200 MHz. All shown traces are averages of 16 signals recorded with a repetition rate of 2 Hz. The samples were measured at room temperature. Transient absorption kinetics were determined using the Levenberg–Marquardt least-squares optimization algorithm in Origin 2020 (by OriginLab), globally fitting the trend lines according to the equation: $y(t) = A_1 \times e^{-t/\tau 1} + A_2 \times e^{-t/\tau 2} + y_0$.

Estimation of the excitation energy and of the quantum yield of 'stable' $FAD^{\bullet-}$ $Trp_3H^{\bullet+}$ pairs detected by transient absorption spectroscopy

The energy of laser flashes entering the *At*64 samples in the transient absorption spectroscopic experiments (Figure 7) was estimated using the $[Ru(bpy)_3]^{2+}$ actinometer[34,40] under the same excitation conditions and geometry. The sample containing 32.3 μM $[Ru(bpy)_3]Cl_2$ had an absorbance A_{480} of 0.2164 over the 1 cm path and 0.0433 over the 2 mm path at the excitation wavelength (480 nm). A_{480} of 0.0433 is converted to a transmittance T_{480} of 90.51%, *i.e.* 9.49% of the excitation light was absorbed by the actinometer over the 2 mm path. The flashes induced an absorption change of ΔA_{457} = 0.0465 (recorded over 1 cm optical path; 64 signals were averaged). Assuming that the $\Delta\varepsilon_{457}$ value for the formation of the ^{3}MLCT (metal-to-ligand charge transfer state formed with a ~100% quantum yield) is close to ~1.1×10^{-4} $M^{-1}cm^{-1}$ as estimated for 450 nm[34] (which is reasonable given the shape of the difference spectrum[41]), one obtains a concentration of the excited $[Ru(bpy)_3]^{2+}$ complexes / formed ^{3}MLCT states of ~4.23 μM. In the excited volume of 40 μL, this concentration corresponds to ~1.69×10^{-10} mol of absorbed photons (out of the total ~1.78×10^{-9} mol, given that only 9.49% photons were absorbed). Since 480 nm photons have an energy of 249,220 J/mol, the energy absorbed by the $[Ru(bpy)_3]Cl_2$ actinometer was ~42 μJ. Considering that the window through which the sample was excited had a surface of 0.2 cm^2 (0.2 × 1.0 cm) and that only 9.49% of the excitation light was absorbed, one obtains an excitation energy (per pulse and per cm^2) of 2.23 mJ.

The ~125 μM *At*64-WT sample had an absorbance A_{480} of 1.0334 over the 1 cm path and 0.2067 over the 2 mm path at the excitation wavelength. A_{480} of 0.2067 is converted to a transmittance T_{480} of 62.13%, so 37.87% of the ~1.78×10^{-9} mol photons entering the sample (*i.e.* ~6.74×10^{-10} mol) were absorbed by the *At*64-WT sample over the 2 mm path. The maximum concentration of the flash-induced radical pairs in the excited volume of 40 μL in the hypothetical case of a 100% quantum yield would hence be ~16.9 μM. $\Delta\varepsilon_{457}$ corresponding to the formation of a $FAD^{\bullet-}$ $TrpH^{\bullet+}$ radical pair equals ε_{457} ($FAD^{\bullet-}$) – ε_{457} (FAD_{ox}) + ε_{457} ($TrpH^{\bullet+}$) ≅ (4740 – 9700 + 350) M^{-1} cm^{-1} = –4610 $M^{-1}cm^{-1}$ (TrpH does not absorb at 457 nm). The observed initial amplitude of the *At*64-WT signal at 457 nm $\Delta A_{457\ (t\rightarrow 0)}$ = –0.065 hence corresponds to ~14.1 μM $FAD^{\bullet-}$ $TrpH^{\bullet+}$ pairs, which is ~83% of the maximum of pairs that could have hypothetically been formed by the excitation flash.

Even though some of the ε values are not known precisely because the absorption spectra of the $FAD^{\bullet-}$ and $TrpH^{\bullet+}$ radicals can (and do) slightly vary from protein to protein, the quantum yields of most of the other PCSf proteins mentioned in the main text were determined by the same method (and essentially confirmed by later ultrafast experiments), so it is safe to say that the losses due to ultrafast recombination of the $FAD^{\bullet-}$ $Trp_1H^{\bullet+}$ and $FAD^{\bullet-}$ $Trp_2H^{\bullet+}$ radical pairs are indeed significantly lower in *At*64 than in the other studied PCSf proteins.

When the vertical axes are scaled to reflect the difference in protein (FAD) concentrations (Figure 7), the initial amplitudes of the signals obtained for the H382S mutant are practically the same as those for the WT protein, indicating that the quantum yield of the 'stable' $FAD^{\bullet-}$ $TrpH^{\bullet+}$ pairs (and the losses through their ultrafast recombination) are very similar in both proteins.

Multiple sequence alignment

For assignment of plant and animal (6–4) PL orthologues, I performed blastp[42] searches using the *At*64 and *Xl*64 amino acid sequences as representative plant and animal (6–4) photolyase sequences against the refseq_protein database with an *E*-value threshold of 10^{-150}. The resulting sequences (202 sequences for plants and 1471 sequences for animals) were aligned with COBALT[43]. From the multiple sequence alignments, the WebLogo[44] was created with the version 3.7.4.

Molecular dynamics simulations for solvation analyses

Molecular dynamics (MD) simulations for solvation analyses were conducted with the AMBER 16 program package[45], as reported previously for the simulation of *At*64-WT[30]. The initial structures of H382D, H382N, H382S, H382V, and H382Y mutants of *At*64 were generated with SWISS-MODEL[46] using the *At*64-WT crystal structure (PDB entry: 3FY4) as the template structure. I applied the Amber force field 14SB[47] and the previously prepared Amber force field[45] for the proteins and $FADH^-$, respectively. The proteins were solvated with TIP3P water model[48] in the simulation boxes with a margin of 12 Å from the proteins to the box boundaries, and the system was neutralized by adding some counter ions (Cl^-). In the following MD simulations, the SHAKE algorithm was used for the constraints[49], the periodic boundary condition with the particle mesh Ewald method was applied[50], and the simulation time step was set to 2 fs. The energy minimization for each system with the Sander module was performed for 5,000 steps with 10 kcal mol^{-1} $Å^{-2}$ of

restrictions on heavy atoms, and for 10,000 steps without any restrictions. After the system temperature was increased from 0 to 300 K for 100 ps with the NVT ensemble (T = 300 K), the system was equilibrated for 1 ns with the NPT ensemble (P = 1 atm and T = 300 K). Then, 200 ns MD simulation in the NPT ensemble (P = 1 atm and T = 300 K) was performed. The last 100 ns of the trajectory for each system was recorded every 20 ps and subjected to analyses. For *At*64-WT, the last 100 ns of the trajectory previously simulated in the same way[30] was used for analyses.

The time-development of an atomic distance was calculated with the distance command in the CPPTRAJ module of the AMBER 16 program package[51]. For solvation analyses, I defined the area within 3.4 and 5.0 Å of the nitrogen atom of the Trp_3H indole ring as the first hydration shell (HS1) and second hydration shell (HS2), respectively. The number of water molecules in HS1 and HS2 at every recording time-points was counted with the watershell command in CPPTRAJ. The behavior of the water molecules in the hydration shells was traced by identifying their IDs with the closest command in CPPTRAJ.

3.5 Conclusions

In this chapter, I found that random solvation of Trp_3H is blocked by the neighboring His residue and the Trp_3H residue is exclusively hydrogen-bonded to the fixed water molecule (which is the water mentioned in the previous chapter). A series of the experimental and theoretical studies suggested that the limited solvation represses the deprotonation of $Trp_3H^{\bullet+}$ and stabilizes the photoinduced $FAD^{\bullet-}$ $Trp_3H^{\bullet+}$ state for the efficient photoreduction. The newly identified mechanism expands the hitherto known clever tricks employed by the PCSf proteins to achieve efficient photoreduction. In addition, the transient absorption measurements revealed that the photoinduced charge-separation in *At*64 takes place with an unexpectedly high (~80%) quantum yield. The molecular origin of the low losses of charge-separated states will be addressed by a future study.

References

1. Sancar, A., Structure and function of DNA photolyase and cryptochrome blue-light photoreceptors. *Chem. Rev.* **103**, 2203–2238 (2003).
2. Chaves, I., Pokorny, R., Byrdin, M., Hoang, N., Ritz, T., Brettel, K., Essen, L.-O., van der Horst, G. T. J., Batschauer, A. & Ahmad, M., The cryptochromes: blue light photoreceptors in plants and animals. *Annu. Rev. Plant Biol.* **62**, 335–364 (2011).
3. Ritz, T., Adem, A. & Schulten, K., A model for photoreceptor-based magnetoreception in birds. *Biophys. J.* **78**, 707–718 (2000).
4. Hore, P. J. & Mouritsen, H., The radical-pair mechanism of magnetoreception. *Annu. Rev. Biophys.* **45**, 299–344 (2016).
5. Coesel, S., Mangogna, M., Ishikawa, T., Heijde, M., Rogato, A., Finazzi, G., Todo, T., Bowler, C. & Falciatore, A., Diatom *Pt*CPF1 is a new cryptochrome/photolyase family member with DNA repair and transcription regulation activity. *EMBO Rep.* **10**, 655–661 (2009).
6. Heijde, M., Zabulon, G., Corellou, F., Ishikawa, T., Brazard, J., Usman, A., Sanchez, F., Plaza, P., Martin, M., Falciatore, A., Todo, T., Bouget, F. Y. & Bowler, C., Characterization of two members of the cryptochrome/photolyase family from *Ostreococcus tauri* provides insights into the origin and evolution of cryptochromes. *Plant Cell Environ.* **33**, 1614–1626 (2010).
7. Zadow, A., Ignatz, E., Pokorny, R., Essen, L. O. & Klug, G., *Rhodobacter sphaeroides* CryB is a bacterial cryptochrome with (6–4) photolyase activity. *FEBS J.* **283**, 4291–4309 (2016).
8. Byrdin, M., Eker, A. P. M., Vos, M. H., & Brettel, K., Dissection of the triple tryptophan electron transfer chain in *Escherichia coli* DNA photolyase: Trp382 is the primary donor in photoactivation. *Proc. Natl. Acad. Sci. USA* **100**, 8676–8681 (2003)
9. Byrdin, M., Villette, S., Eker, A. P. M. & Brettel, K., Observation of an intermediate tryptophanyl radical in W306F mutant DNA photolyase from *Escherichia coli* supports electron hopping along the triple tryptophan chain. *Biochemistry* **46**, 10072–10077 (2007)
10. Kim, S., Sancar, A., Essenmachert, C. & Babcockt, G. T., Time-resolved EPR studies with DNA photolyase : Excited-state $FADH^{\bullet}$ abstracts an electron from Trp-306 to generate $FADH^{-}$, the catalytically active form of the cofactor. *Proc. Natl. Acad. Sci. USA* **90**, 8023–8027 (1993).
11. Brazard, J., Usman, A., Lacombat, F., Ley, C., Martin, M. M., Plaza, P., Mony, L., Heijde, M., Zabulon, G. & Bowler, C., Spectro-temporal characterization of the photoactivation mechanism of two new oxidized cryptochrome/photolyase photoreceptors. *J. Am. Chem. Soc.* **132**, 4935–4945 (2010).
12. Liu, Z., Tan, C., Guo, X., Li, J., Wang, L., Sancar, A. & Zhong, D., Determining complete electron flow in the cofactor photoreduction of oxidized photolyase. *Proc. Natl. Acad. Sci. U.S.A.* **110**, 12966–12971 (2013).

13. Aubert, C., Vos, M. H., Mathis, P., Eker, A. P. M. & Brettel, K., Intraprotein radical transfer during photoactivation of DNA photolyase. *Nature* **405**, 586–570 (2000).
14. Heelis, P. F., Payne, G. & Sancar, A., Photochemical properties of escherichia coli DNA photolyase: selective photodecomposition of the second chromophore. *Biochemistry* **26**, 4634–4640 (1987).
15. Einholz, C., Nohr, D., Rodriguez, R., Topitsch, A., Kern M., Goldmann, J., Chileshe, E., Okasha, M., Weber, S. & Schelicher, E., pH-dependence of signaling-state formation in *Drosophila* cryptochrome. *Arch. Biochem. Biophys.* **700**, 108787.
16. Berndt, A., Kottke, T., Breitkreuz, H., Dvorsky, R., Henning, S., Alexander, M. & Wolf, E., A novel photoreaction mechanism for the circadian blue light photoreceptor *Drosophila* cryptochrome. *J. Biol. Chem.* **282**, 13011–13021 (2007)
17. Müller, P., Bouly, J.-P., Hitomi, K., Balland, V., Getzoff, E. D., Ritz, T. & Brettel, K., ATP binding turns plant cryptochrome into an efficient natural photoswitch. *Sci. Rep.* **4**, 5175 (2014).
18. Müller, P. & Bouly, J. P., Searching for the mechanism of signaling by plant photoreceptor cryptochrome. *FEBS Lett.* **589**, 189–192 (2015).
19. Hitomi, K., DiTacchio, L., Arvai, A. S., Yamamoto, J., Kim, S.-T., Todo, T., Tainer, J. A., Iwai, S., Panda, S. & Getzoff, E. D., Functional motifs in the (6–4) photolyase crystal structure make a comparative framework for DNA repair photolyases and clock cryptochromes. *Proc. Natl. Acad. Sci. U.S.A.* **106**, 6962–6967 (2009).
20. Maul, M. J., Barends, T. R., Glas, A. F., Cryle, M. J., Domratcheva, T., Schneider, S., Schlichting, I. & Carell, T., Crystal structure and mechanism of a DNA (6–4) photolyase. *Angew. Chem. Int. Ed.* **47**, 10076–10080 (2008).
21. Müller, P., Yamamoto, J., Martin, R., Iwai, S. & Brettel, K., Discovery and functional analysis of a 4th electron-transferring tryptophan conserved exclusively in animal cryptochromes and (6–4) photolyases. *Chem. Commun.* **51**, 15502–15505 (2015).
22. Scheerer, P., Zhang, F., Kalms, J., von Stetten, D., Krauss, N., Oberpichler, I. & Lamparter, T., The class III cyclobutane pyrimidine dimer photolyase structure reveals a new antenna chromophore binding site and alternative photoreduction pathways. *J. Biol. Chem.* **290**, 11504–11514 (2015).
23. Zoltowski, B. D., Chelliah, Y., Wickramaratne, A., Jarocha, L., Karki, N., Xu, W., Mouritsen, H., Hore, P. J., Hibbs, R. E., Green, C. B. & Takahashi, J. S., Chemical and structural analysis of a photoactive vertebrate cryptochrome from pigeon. *Proc. Natl. Acad. Sci. USA* **116**, 19449–19457 (2019).
24. Langenbacher T., Immeln, D., Dick B. & Kottke T., Microsecond light-induced proton transfer to flavin in the blue light sensor plant cryptochrome, *J. Am. Chem. Soc.* **131**, 14274–14280 (2009).
25. Lacombat, F., Espagne, A., Dozova, N., Plaza, P., Müller, P., Brettel, K., Franz-Badur, S. & Essen, L. O., Ultrafast oxidation of a tyrosine by proton-coupled electron transfer promotes

light activation of an animal-like cryptochrome. *J. Am. Chem. Soc.* **141**, 13394–13409 (2019).

26. Müller, P., Ignatz, E., Kiontke, S., Brettel, K. & Essen, L. O., Sub-nanosecond tryptophan radical deprotonation mediated by a protein-bound water cluster in class II DNA photolyases. *Chem. Sci.* **9**, 1200–1212 (2018).
27. Posener, M. L., Adams, G. E., Wardman, P. & Cundall, R. B., Mechanism of tryptophan oxidation by some inorganic radical anions: a pulse radiolysis study. *J. Chem. Soc., Faraday Trans. 1* **72**, 2231–2239 (1976).
28. Dixon, W. T. & Murphy, D., Determination of acidity constants of some phenol radical cations by means of electron-spin resonance. *J. Chem. Soc., Faraday Trans.* **272**, 1221–1230 (1976).
29. Yamamoto, J., Shimizu, K., Kanda, T., Hosokawa, Y., Iwai, S., Plaza, P. & Müller, P., Loss of fourth electron-transferring tryptophan in animal (6–4) photolyase impairs DNA repair activity in bacterial cells. *Biochemistry* **56**, 5356–5364 (2017).
30. Hosokawa, Y., Sato, R., Iwai, S. & Yamamoto, J., Implications of a water molecule for photoactivation of plant (6−4) photolyase. *J. Phys. Chem. B* **123**, 5059–5068 (2019).
31. Deepak, R. N. V. K. & Sankararamakrishnan, R., N−H···N hydrogen bonds involving histidine imidazole nitrogen atoms: a new structural role for histidine residues in proteins. *Biochemistry* **55**, 3774–3783 (2016).
32. Holliday, G. L., Mitchell, J. B. O. & Thornton, J. M., Understanding the functional roles of amino acid residues in enzyme catalysis. *J. Mol. Biol.* **390**, 560–577 (2009).
33. Bhattacharyya, R., Saha, R. P., Samanta, U. & Chakrabarti, P., Geometry of interaction of the histidine ring with other planar and basic residues. *J. Proteome Res.* **2**, 255–263 (2003).
34. Müller, P. & Brettel, K., $[Ru(bpy)_3]^{2+}$ as a reference in transient absorption spectroscopy: differential absorption coefficients for formation of the long-lived ^{3}MLCT excited state. *Photochem. Photobiol. Sci.* **11**, 632–636 (2012).
35. Müller, P., Brettel, K., Grama, L., Nyitrai, M. & Lukacs, A., Photochemistry of wild-type and N378D mutant *E. coli* DNA photolyase with oxidized FAD cofactor studied by transient absorption spectroscopy. *ChemPhysChem* **17**, 1329–1340 (2016).
36. Lacombat, F., Espagne, A., Dozava, N., Plaza, P., Müller, P., Emmerich, H. J., Saft, M. & Essen L. O. Ultrafast photoreduction dynamics of a new class of CPD photolyases. *Photochem. Photobiol. Sci.* **20**, 733–746 (2021)
37. Coesel, S., Mangogna, M., Ishikawa, T., Heijde, M., Rogato, A., Finazzi, G., Todo, T., Bowler, C. & Falciatore, A., Diatom *Pt*CPF1 is a new cryptochrome/photolyase family member with DNA repair and transcription regulation activity. *EMBO Rep.* **10**, 655–661 (2009).
38. Nakajima, S., Sugiyama, M., Iwai, S., Hitomi, K., Otoshi, E., Kim, S. T., Jiang, C. Z., Todo, T., Britt A. B. & Yamamoto, K., Cloning and characterization of a gene (UVR3) required for photorepair of 6–4 photoproducts in *Arabidopsis thaliana*. *Nucleic Acids Res.* **26**, 638–644 (1998).

39. Li, J., Uchida, T., Ohta, T., Todo, T. & Kitagawa, T., Characteristic structure and environment in FAD cofactor of (6–4) photolyase along function revealed by resonance Raman spectroscopy. *J. Phys. Chem. B* **110**, 16724–16732 (2006).
40. Byrdin, M., Thiagarajan, V., Villette, S., Espagne, A. & Brettel, K., Use of ruthenium dyes for subnanosecond detector fidelity testing in real time transient absorption. *Rev. Sci. Instrum.* **80**, 043102 (2009).
41. Lachish, U., Infelta, P. P. & Grätzel, M., Optical absorption spectrum of excited ruthenium tris-bipyridyl ($Ru(bpy)_3^{2+}$). *Chem. Phys. Lett.* **62**, 317–319 (1979).
42. Altschul, S. F., Gish, W., Miller, W., Myers, E. W. & Lipman, D. J., Basic local alignment search tool. *J. Mol. Biol.* **215**, 403–410 (1990).
43. Papadopoulos, J. S. & Agarwala, R., COBALT: constraint-based alignment tool for multiple protein sequence. *Nucleic Acids Res.* **41**, W34–40 (2013).
44. Crooks, G. E., Hon, G., Chandonia, J. M. & Brenner, S. E., WebLogo: A sequence logo generator. *Genome Res.* **14**, 1188–1190, (2004).
45. Case, D. A., Babin, V., Berryman, J. T., Betz, R. M., Cai, Q., Cerutti, D. S., Cheatham, T. E., Darden, T. A., Duke, R. E., Gohlke, H., *et al.* Amber16. University of California, San Francisco.
46. Waterhouse, A., Bertoni, M., Bienert, S., Studer, G., Tauriello, G., Gumienny, R., Heer, F. T., de Beer, T. A. P., Rempfer, C., Bordoli, L., *et al.* SWISS-MODEL: Homology modelling of protein structures and complexes. *Nucleic Acids Res.* **46**, W296–W303 (2018).
47. Maier, J. A., Martinez, C., Kasavajhala, K., Wickstrom, L., Hauser, K. E. & Simmerling, C., ff14SB: Improving the accuracy of protein side chain and backbone parameters from ff99SB. *J. Chem. Theory Comput.* **11**, 3696–3713 (2015).
48. Jorgensen, W. L., Chandrasekhar, J., Madura, J. D., Impey, R. W. & Klein, M. L., Comparison of simple potential functions for simulating liquid water. *J. Chem. Phys.* **79**, 926–935 (1983).
49. Ryckaert, J.-P., Ciccotti, G. & Berendsen, H. J. C., Numerical integration of the cartesian equations of motion of a system with constraints: molecular dynamics of n-alkanes. *J. Comput. Phys.* **23,** 327–341 (1977).
50. Darden, T., York, D. & Pedersen, L., Particle mesh Ewald: an N·log(N) method for Ewald sums in large systems. *J. Chem. Phys.* **98**, 10089–10092 (1993).
51. Roe, D. R. & Cheatham, T. E., III. PTRAJ and CPPTRAJ: software for processing and analysis of molecular dynamics trajectory data. *J. Chem. Theory Comput.* **9**, 3084–3095 (2013).

Chapter 4

Mechanistic studies on photoinduced conformational changes in photolyase/cryptochrome superfamily

4.1 Introduction

In Chapters 2 and 3, I discovered the distinctive mechanisms allowing plant (6–4) photolyases to stabilize photoinduced charge-separated states for the productive photoreduction, by focusing on the surroundings of the final electron donating Trp residue. In Chapter 4, I tried to uncover a common factor regulating FAD photoreduction among photolyases and cryptochromes. I shed light on photoinduced conformational changes in photolyases, which has been less investigated than those in cryptochromes. Comprehensive analyses of conformational changes in plant (6–4) photolyase suggest a shared mechanism enabling photolyases and cryptochromes to undergo structural rearrangements. The knowledge will be helpful to disclose the detailed movement of residues in cryptochromes.

Photolyase and cryptochrome superfamily (PCSf) is a flavoprotein family with a high architectural similarity and a remarkable functional diversity[1,2]. Photolyases (PLs) are evolutionarily ancient enzymes able to repair UV-induced lesions in DNA in a light-dependent manner and are divided into CPD PLs and (6–4) PLs depending on their substrates: cyclobutane pyrimidine dimers (CPDs) and pyrimidine(6–4)pyrimidone photoproducts ((6–4) PPs). PLs harbor a flavin adenine dinucleotide (FAD) chromophore as a catalytic cofactor, and the essential process for the photorepair of the DNA damages is the photoinduced electron transfer from the two-electron reduced FAD state ($FADH^-$) to the substrates. On the other hand, cryptochromes (CRYs), evolutionarily diverged from PLs, are responsible for regulation of gene transcription concerning various biological events[3], such as photoreceptive plant growth[4,5] and circadian rhythm regulation in animals[6,7]. CRYs have a N-

terminal structural motif with a high similarity to PLs, which is called the photolyase homology region (PHR), and a highly variable C-terminal tail extension (CTE)[8]. The CTE in CRY from *Drosophila melanogaster* (*Dm*CRY) consists of 20 amino acid residues and is docked to PHR in the dark-adapted state[9,10], but suggested to be dissociated from the binding site upon the photoreception by the FAD cofactor[11-13]. Hence, the structural change in CTE is considered to trigger the signal transduction in *Dm*CRY[14].

FAD in PCSf proteins can exist in various redox states: the fully oxidized FAD_{ox}, one-electron reduced anionic radical $FAD^{\bullet-}$, one-electron reduced neutral radical $FADH^{\bullet}$, and two-electron reduced anionic $FADH^{-}$ states. While the most oxidized FAD_{ox} state is often found in recombinantly-produced PCSf proteins, the catalytically active state in PLs is $FADH^{-}$ and the signaling state in *Dm*CRY is suggested to be $FAD^{\bullet-}$, indicating that FAD needs to be reduced for their functions[15]. PCSf proteins activate (reduce) FAD in a light-dependent manner by employing a conserved process called photoactivation or photoreduction. Upon photoexcitation, the excited state of FAD ($^{*}FAD_{ox}$ or $^{*}FADH^{\bullet}$) abstracts an electron from a nearby Trp residue (Trp_1H)[16]. To keep the resultant $FAD^{\bullet-}$ or $FADH^{-}$ reduced, the hole on Trp_1H quickly migrates to Trp residues on the surface side via successive electron transfer along a Trp chain[17,18], composed of typically three Trp residues and one auxiliary Trp[19] or Tyr[20] residue in animal (6–4) PLs and CRYs. Finally, the terminal radical cation is quenched by external reducing agents[21].

It has been suggested that the photoreduction of FAD_{ox} to $FAD^{\bullet-}$ in *Dm*CRY accompanies the CTE structural changes, which can be recognized as the signal for partner proteins, such as a

circadian gene repressor called Timeless (TIM)[22] and an E3 ubiquitin ligase named jetlag (JET)[23]. Considering the report that photoreduction deficient mutants of *Dm*CRY can exhibit the photosensory function in *Drosophila* cells[24], however, the mechanism of the structural changes has not been well established.

Although the photoreduction pathway of *Dm*CRY is shared with (6–4) PLs[25], conformational changes in (6–4) PLs upon photoreduction have been less addressed than in *Dm*CRY[10,26]. Even though (6–4) PLs does not have CTE, Yamada *et al.* reported[27] that perturbation of the β-sheet conformation and very small changes in α-helicity in *Xenopus laevis* (6–4) PL were observed upon the reduction of FAD_{ox} to $FADH^{-}$. This result suggests that (6–4) PLs does not undergo drastic structural changes as observed in *Dm*CRY but experiences small conformational changes during the photoreduction process. Understanding of the molecular mechanism of the conformational changes in photoreduction of (6–4) PLs would thus provide a clue for the signal transduction of *Dm*CRY.

In Chapter 4, I investigated possible conformational changes of *Arabidopsis thaliana* (6–4) photolyase (*At*64) upon light illumination and whether the changes have an impact on its activation mechanism reducing FAD to $FADH^{-}$. A combination of structural analyses, electrochemical measurements, and steady-state photoreduction kinetics suggests that a photoinduced helix movement is involved in FAD photoreduction in *At*64. Based on the conservation of the key residues for the helix movement between *At*64 and *Dm*CRY, the proposed conformational rearrangement observed in *At*64 could therefore be an initiation of the drastic structural change in *Dm*CRY.

4.2 Results

4.2.1 Photoinduced structural changes in At64 suggested by HDX-MS measurement

To test the possibility that (6–4) PLs undergo conformational changes upon photoreduction of FAD, I performed hydrogen/deuterium exchange mass spectrometry (HDX-MS) measurement of *At*64 in dark and light conditions. When protein conformational changes are induced upon photoreduction and the changed moieties are more prone to be solvated than in the dark-adapted state, a difference in the deuterium uptakes of peptide fragments can be observed. Although the structural analysis by differential Fourier transform infrared (FTIR) spectroscopy is a powerful tool to provide the detail of the atomic positions of the movement, HDX-MS can tell us regions of movement in a panoramic manner.

*At*64 was recombinantly purified as previously described[28]. To prepare the light sample, FAD was photoreduced in the presence of DTT. Indeed, the dark and light samples mainly contained FAD_{ox} and $FADH^{-}$, respectively (Figure 1a). After each sample was incubated with D_2O buffer for 10, 100, 1000, and 10000 s, the sample was digested with immobilized pepsin and analyzed by ultra performance liquid chromatography-mass spectrometry (UPLC-MS). 95 peptides from *At*64 were identified, yielding 86.2% coverage with an overall redundancy of 2.80. For structural comparison of *At*64 between the dark and light conditions, a relative deuterium uptake map (dark minus light) was projected onto the crystal structure of *At*64 (Figure 1b). In this map, the most prominent difference is observed in a peptide including Asp396. Asp396 forms a salt bridge with Arg367 near the FAD chromophore (Figures 1b and c), and the salt bridge is strongly conserved in PCSf proteins. Recent

studies in other PCSf proteins[29-31] suggested that the salt bridge can be rearranged upon photoreduction to stabilize the reduced FAD states. Therefore, the most decelerated deuterium uptake observed in the peptide containing Asp396 is attributable to the movement of the salt bridge. This result also implies that the conformational change of Arg367 should take place associated with the salt bridge perturbation. Although no peptide fragments covering the N-terminal portion of the α15 helix, where Arg367 is located, was observed, a fragment on the C-terminal side of the helix was found to exhibit significantly slower uptakes in the light states than in the dark state (Figure 1b), indicating that the whole region of α15 could undergo conformational changes accompanied by the salt bridge perturbation.

Similar observations were obtained for the α17 helix flanking Asp396, and the peptides on the N-terminal and C-terminal sides had significantly different uptakes upon illumination, suggesting that α17 could also be rearranged to follow the salt bridge movement. Altogether, the HDX-MS measurement of *At*64 suggests that the α15 and α17 helices go through conformational changes triggered by the photoinduced Arg367/Asp396 salt bridge perturbation. Although HDX-MS analyses generally do not inform us how residues on these helices are reorganized in detail, the decreasing deuterium uptakes for these fragments on the helices upon illumination suggests a structural rearrangement to shield these residues from the solvent in the light state. One of the possible movements to explain the observed difference could be a shortening of the relative distance between the α15 and α17 helices. In the crystal structure of *At*64, the closest residues between the helices are Thr375 in α15 and Ser410 in α17, and the distance between O atoms of the side chain hydroxyl groups

is 5.1 Å (Figure 1c). I hypothesized that the photoinduced structural changes would make Thr375 and Ser410 closer and hydrogen-bonded upon the helices movement, which further would stabilize the closer position between α15 and α17 helices in the $FADH^-$ state.

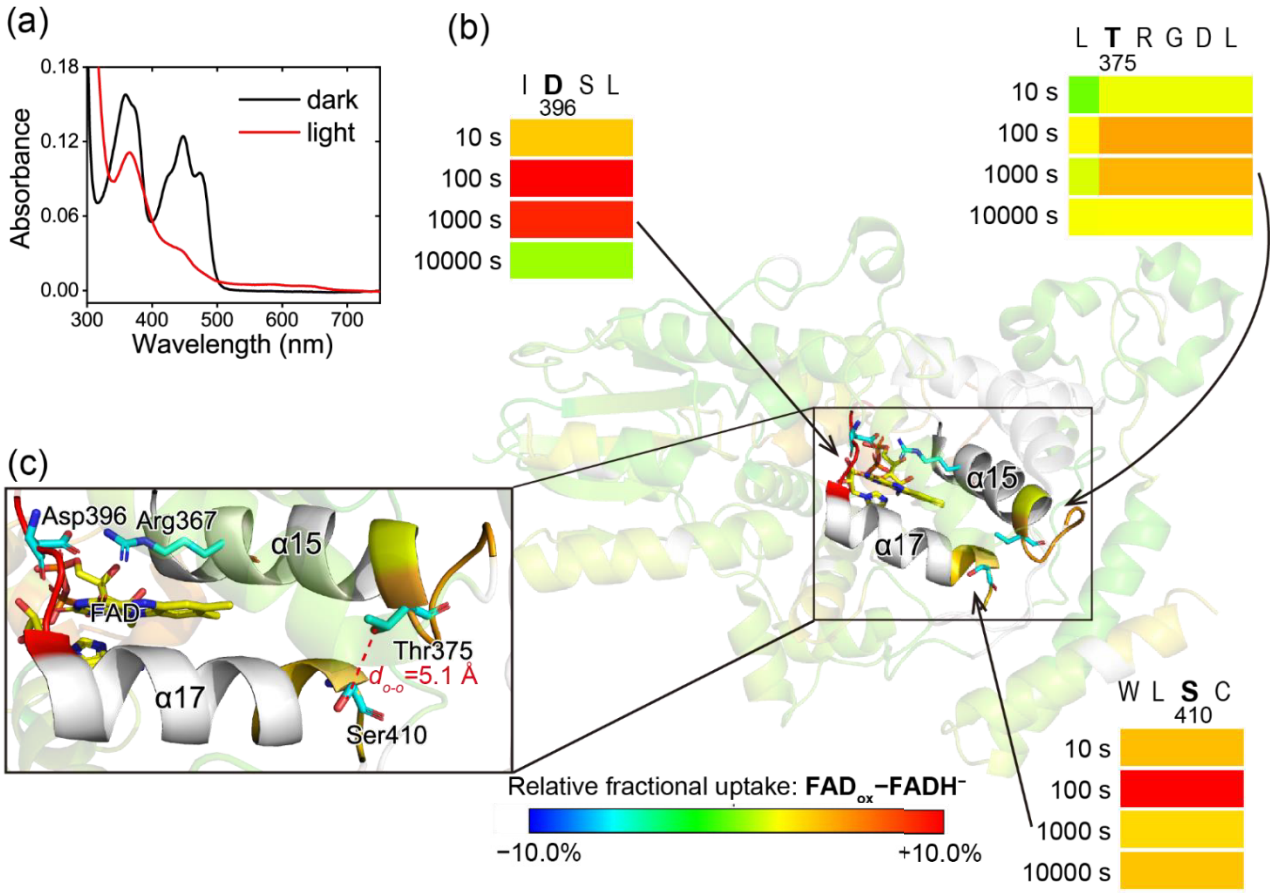

Figure 1. HDX-MS measurement of *At*64 in the dark (FAD_{ox}) and light ($FADH^-$) states. (a) UV-Vis spectra of *At*64 in the dark and light. The spectra confirmed that the dark and light samples mainly harbor FAD_{ox} and $FADH^-$, respectively. (b), (c) The relative fractional deuterium uptake at 1000 s in dark minus light (FAD_{ox} minus $FADH^-$) projected onto the crystal structure of *At*64 (PDB: 3FY4). For the white segments, no peptides could be assigned by the analysis. (c) Closer view on the α15 and α17 helices. Asp396, which shows the most prominent uptake difference, form a salt bridge with Arg367 on the FAD cofactor (yellow). Thr375 in α15 and Ser410 in α17 are the closest residues in these helices (the distance between O atoms of their hydroxyl groups is in 5.1 Å). The hydroxyl groups are potential to form a hydrogen bond because the difference in deuterium uptakes observed around the helices suggests a movement to make the helices closer upon the photoreduction.

4.2.2 Mutational effects of T375V on midpoint potential of FAD_{ox}/$FADH^-$ couple

There are possibilities that the structural rearrangement between α15 and α17 helices suggested by HDX-MS would modulate the redox stabilities of FAD in *At*64. To address the possibilities, I tried to compare the midpoint potentials of a $FAD_{ox}/FADH^-$ redox couple in the wild type of *At*64 (*At*64-WT) and a mutant, in which the Thr375 was replaced with the Val residue (*At*64-T375V). The side chain of the Val residue resembles that of the Thr residue except the presence of a methyl group instead of the hydroxy group, and therefore would not prevent α15 from approaching α17 in the $FADH^-$ state but is no longer able to form a hydrogen bond between Val375 and Ser410.

To measure the midpoint potentials, I employed a spectroscopic electrochemical method called the xanthine/xanthine oxidase (X/XO) method[32]. In the well-established technique to evaluate the midpoint potentials of flavin derivatives in other flavoproteins[15,33], electrons released from the oxidation of xanthine by xanthine oxidase reduces FAD and a reference dye simultaneously in the presence of a redox mediator. If the electron supply is slow enough to keep the equilibration of the oxidized and reduced forms of FAD and the dye, the Nernst equation is applied to each redox active compound, as follows.

$$E_p = E_{m,p} + \frac{RT}{n_p F}\ln\frac{[\mathrm{OX}]}{[\mathrm{RED}]} \quad \text{for FAD in protein} \tag{1}$$

$$E_D = E_{m,D} + \frac{RT}{n_D F}\ln\frac{[\mathrm{D_{OX}}]}{[\mathrm{D_{RED}}]} \quad \text{for a reference dye} \tag{2}$$

In these equations, reduction potentials of the reference dye and FAD shown in E_p and E_D are related to their concentration ratio between oxidized and reduced states ([OX] and [RED] for FAD, $[D_{OX}]$ and $[D_{RED}]$ for the dye) and their midpoint potentials ($E_{m,p}$ and $E_{m,D}$). R is the gas constant (8.314 J K^{-1} mol^{-1}), F is the Faraday constant (96,485 C mol^{-1}), T is the absolute temperature (298 K in the

experiment), and n_p and n_D are the numbers of electrons for the reduction of FAD in the protein and the dye, respectively. Supposing that their midpoint potentials are similar to each other (within 30 mV), the reduction potentials should be equal to each other ($E_p = E_D$), and the following equation holds.

$$E_{m,p} + \frac{RT}{n_p F} \ln \frac{[\mathrm{OX}]}{[\mathrm{RED}]} = E_{m,D} + \frac{RT}{n_D F} \ln \frac{[\mathrm{D_{OX}}]}{[\mathrm{D_{RED}}]} \quad (3)$$

To calculate the midpoint potential in *At*64 ($E_{m,p}$) based on Equation 3, the number of electrons to reduce FAD and the reference dye should be required. Here, Safranin T was used as the reference dye, which is known to undergo the two-electron reduction in the X/XO system ($n_D = 2$). On the other hand, FAD in *At*64 can exist in fully oxidized FAD_{ox}, one-electron reduced neutral radical $FADH^{\bullet}$, and two-electron reduced anionic $FADH^{-}$ states. Based on the characteristic UV/Vis absorption spectrum to each FAD species (Figure 2a), I first determined the number of electrons for the reduction of FAD_{ox} in *At*64-WT by monitoring disappearance of FAD_{ox} at 450 nm and formation of $FADH^{\bullet}$ at 635 nm. Indeed, the reduction of FAD_{ox} (plus Safranin T) by the X/XO system showed the decrease in the absorbance changes at 450 nm and a very low level of the absorbance increase at 635 nm (inset of Figure 2b). UV/Vis absorption spectra before and after the reaction (Figure 2b) also confirmed the conversion of FAD_{ox} to $FADH^{-}$ with a very small amount of $FADH^{\bullet}$ formation (a few % of the total FAD concentration) and simultaneous two-electron reduction of Safranin T as shown in the decrease in the absorbance at 510 nm. The results clearly demonstrate that FAD_{ox} is reduced to $FADH^{-}$ without accumulation of $FADH^{\bullet}$ in the X/XO system, meaning that the FAD in *At*64-WT undergoes the two-electron reduction in the system ($n_p = 2$) and that [OX] and [RED] in Equation 3

can be interpreted as the concentration of FAD_{ox} and $FADH^-$ ([FAD_{ox}] and [$FADH^-$]). By substituting constant values into Equation 3, Equation 4 was obtained for the data analyses.

$$12.8 \ln \frac{[\mathrm{D_{OX}}]}{[\mathrm{D_{RED}}]} = 12.8 \ln \frac{[\mathrm{FAD_{ox}}]}{[\mathrm{FADH^-}]} + E_{m,p} - E_{m,D} \quad (4)$$

To calculate the midpoint potential of the $FAD_{ox}/FADH^-$ couple in *At*64-WT ($E_{m,p}$) according to Equation 4, I monitored the concentration ratio of FAD and Safranin T between oxidized and reduced states during the reduction by the X/XO system. The decrease in the absorbance at 450 nm and 510 nm showed the reduction of FAD_{ox} and Safranin T, respectively (Figure 2c). After the reduction was confirmed by the UV/Vis absorption spectra recorded before and (1 h) after the reaction (Figure 2c), the Nernst concentration terms (12.8 ln ([oxidized]/[reduced]) for FAD and Safranin T) were plotted (Figure 2d). The plots yielded a slope of 1.01 ± 0.18, which was in good agreement with the expected value of 1 from Equation 4, and an intercept of 0.323 ± 5.0 mV. Because the intercept value corresponds to the difference in the midpoint potential of FAD and Safranin T ($E_{m,p} - E_{m,D}$), and the midpoint potential of Safranin T is known to be −289 mV vs. SHE ($E_{m,D}$ = −289 mV vs. SHE), the midpoint potential of $FAD_{ox}/FADH^-$ couple in *At*64-WT was found to be −289 ± 5.0 mV vs. SHE.

To perform the measurement for the *At*64-T375V mutant, the number of electrons for the reduction of FAD in *At*64-T375V by the X/XO system was also evaluated. In contrast to the case of *At*64-WT, the absorption at 635 nm by $FADH^{\bullet}$ was growing during the reduction for 1 hour (Figures 2e and f). The formation ratio of $FADH^{\bullet}$ after 1 hour was estimated to be ~42 %, meaning that *At*64-T375V undergoes the concomitant one- and two-electron reduction of FAD. In the case of the mixed-type reduction, n_p cannot be defined and therefore midpoint potentials cannot be obtained by the

X/XO method. However, the result indicates that the T375V mutation could affect the stability of the reduced FAD states. While the observed two-electron reduction of FAD_{ox} in *At*64-WT indicates that the midpoint potential of $FADH^{\bullet}/FADH^{-}$ couple is much higher than that of $FAD_{ox}/FADH^{\bullet}$ couple, the relationship between two redox couples could be disturbed in *At*64-T375V. The mutational effect of T375V supports the idea that the reduction of FAD to $FADH^{-}$ induces the structural rearrangement of the α15 and α17 helices, leading to stabilization of the $FADH^{-}$ state in *At*64-WT. Although the possibility that the mutation affects local structures of the α15 helix resulting in the modulation of the midpoint potentials cannot be excluded, it can be safely concluded that the α15 helix plays a key role in stabilizing $FADH^{-}$ in *At*64-WT.

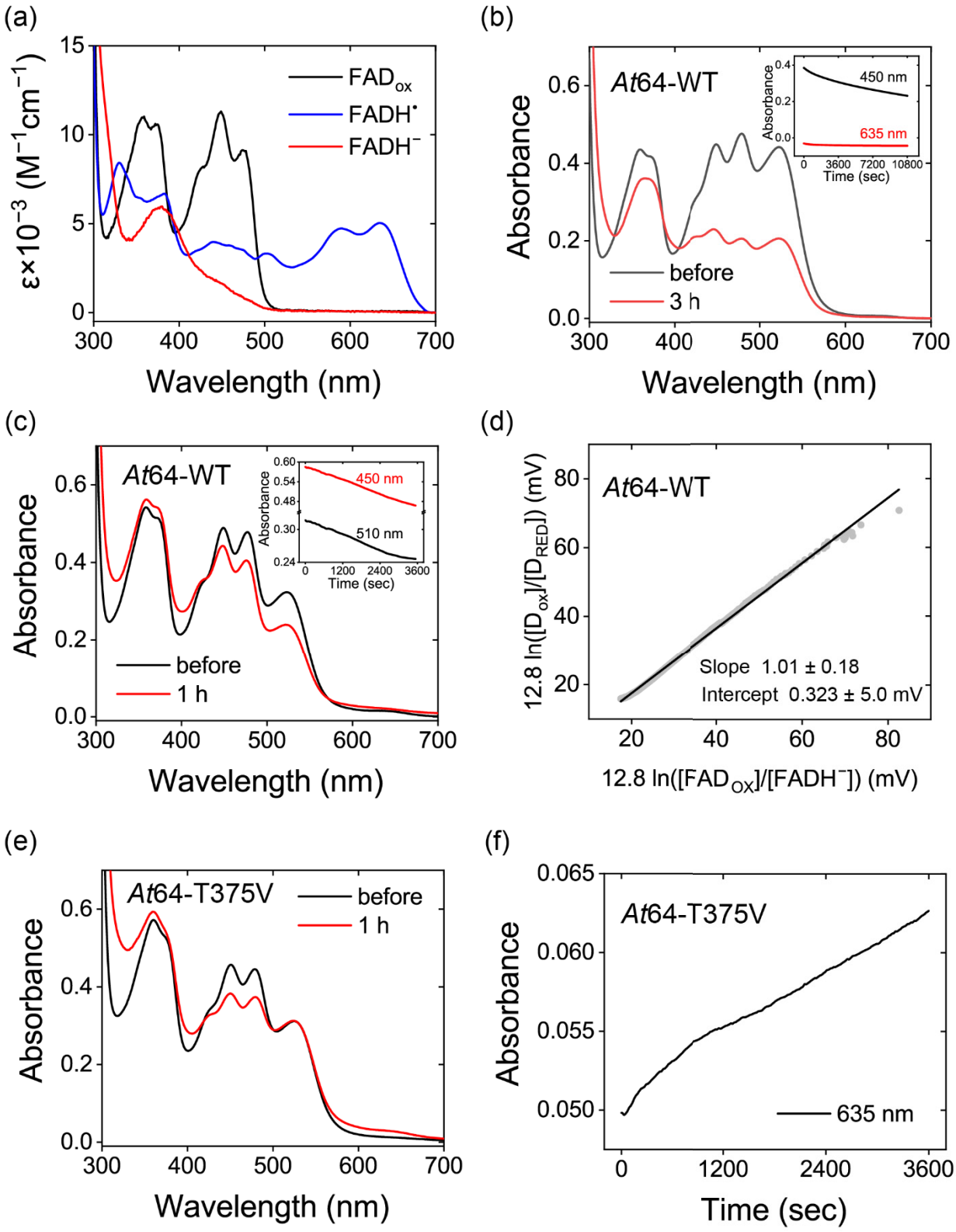

Figure 2. Spectroscopic electrochemical measurement of midpoint potentials of FAD in *At*64 variants. (a) Reference absorption spectra of FAD species expected to be produced during the measurement. (b) The UV/Vis absorption spectra recorded before and (3 h) after the reduction of FAD in *At*64-WT and Safranin T by the xanthine/xanthine oxidase system. The spectra show a very low contribution of $FADH^{\bullet}$ to the reaction. The inset shows the absorption changes at 450 nm and 635 nm measured every 10 s for 3 h, suggesting the reduction of FAD_{ox} to $FADH^{-}$ without a significant accumulation of $FADH^{\bullet}$. (c) The UV/Vis absorption spectra recorded before and (1 h) after the reduction of FAD in *At*64-WT and Safranin T by the xanthine/xanthine oxidase system. The spectra indicate a

gradually conversion of FAD_{ox} to $FADH^-$ and a simultaneous reduction of Safranin T. The inset shows absorption changes at 450 nm and 510 nm measured every 10 s for 1 h. (d) Plots of Nernst concentration terms (FAD in *At*64-WT vs. Safranin T). The midpoint potential of FAD_{ox}/ $FADH^-$ couple in *At*64-WT is calculated to be −289 ± 5.0 mV vs. SHE by analyzing the plots with Equation 4. (e) The UV/Vis absorption spectra recorded before and (1 h) after the reduction of FAD in *At*64-T375V by the xanthine/xanthine oxidase system. The spectra show an increasing absorption around 600 nm, contributed by an accumulation of $FADH^{\bullet}$ state. (f) Changes in absorbance at 635 nm during the reduction of FAD in *At*64-T375V. The increase in the absorbance shows the transient accumulation of $FADH^{\bullet}$.

4.2.3 Impact of hydrogen-bonding formation between Thr375 and Ser410 on photoreduction steady-state kinetics

As shown in the modulated midpoint redox potential of FAD in the *At*64-T375V mutant, it should be an interesting question whether the mutation of T375V has an impact on the photoreduction ability of *At*64. Then, the steady-state photoreduction kinetics for *At*64-T375V was evaluated, as previously described for *At*64-WT[28]. *At*64-T375V was illuminated with >430 nm light in the presence of an external reductant under anaerobic conditions, and the UV/Vis absorption spectral changes were recorded. The overall spectral changes of the mutants upon illumination indicated that FAD_{ox} was gradually converted into $FADH^-$, via transient accumulation of as small amounts of $FADH^{\bullet}$ as observed for *At*64-WT (~10%)[28], as seen in the absorption growth and decay between 500 and 700 nm (Figure 3). The decay of the normalized absorption at 450 nm characteristic for FAD_{ox} was fitted with a monoexponential decay function, and FAD photoreduction in *At*64-T375V was found to occur with a half-life ($t_{1/2}$) of 61.1 ± 6.2 s (Figure 3a). The value indicates that the photoreduction kinetics for *At*64-T375V is about 2.8-fold slower than that in *At*64-WT ($t_{1/2}$ = 21.6 ± 0.5 s)[28]. The slow kinetics shows that the mutation decelerates its photoactivation process, suggesting that a hydrogen bond

between Thr375 and Ser410 would anchor α15 and α17 helices upon the assumed structural rearrangement, which would enhance the photoreduction in *At*64.

To evaluate the effect of the accessibility of α15 to α17 on the photoreduction in *At*64, the photoreduction kinetics for the Ala mutant (*At*64-T375A) was also measured. As a result, *At*64-T375A showed about 2.1-fold slower photoreduction kinetics than *At*64-WT but 1.4-fold faster kinetics than *At*64-T375V ($t_{1/2}$ = 45.0 ± 2.8 s for *At*64-T375A, Figure 3b). The moderate mutational effect of T375A on the photoreduction kinetics sounds reasonable, because the side chain of the Ala residue, which cannot form a hydrogen bond with Ser410 as well as Val in *At*64-T375V, is less hindered than the Val side chain, and therefore such structural rearrangement between α15 and α17 more likely takes place than the case of *At*64-T375V. Altogether, the conformational changes of the α15 and α17 helices are suggested to play a role in the photoreduction of FAD in *At*64.

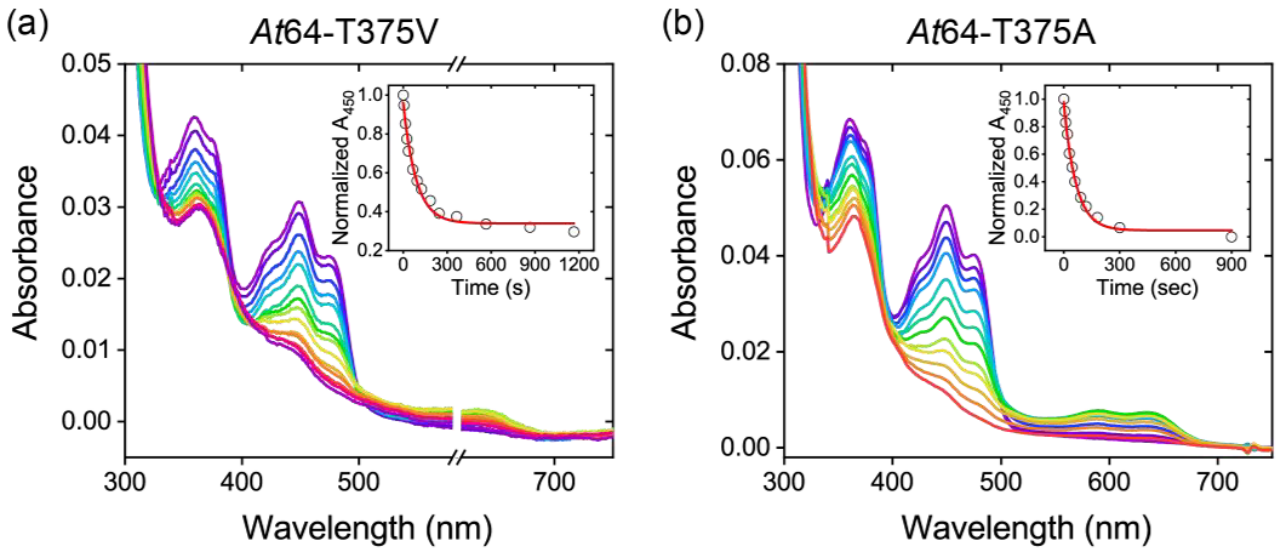

Figure 3. Evolution of absorption spectra upon FAD photoreduction in the (a) T375V and (b) T375A mutants of *At*64. The plots of normalized A_{450} against time are reasonably well fitted with monoexponential functions as shown in the insets. (a) Data between 580 and 620 nm are omitted due to an irreproducible bump in the region produced by instrumental problems.

4.3 Discussion

4.3.1 Possible helix movements upon reduction of FAD in At64 and other PCSf proteins

In this study, I investigated the possibility that *A. thaliana* (6–4) photolyase undergoes structural changes upon FAD photoreduction. HDX-MS measurement disclosed the structural difference between the FAD_{ox} and $FADH^-$ states, where the α15 and α17 helices come closer in the $FADH^-$ state, presumably caused by the conformational change of the Arg367/Asp396 salt bridge underneath the isoalloxazine ring of FAD, so that a hydrogen bond would be formed between the Thr375 and Ser410 residues located in the C-terminal part of the helices. The hypothetical stabilization of *At*64 in the $FADH^-$ state due to the rearrangement was supported by the midpoint potential measurements of *At*64 variants, in which a mutation (T375V) disturbed a balance between midpoint potentials of the $FAD_{ox}/FADH^{\bullet}$ and $FADH^{\bullet}/FADH^-$ couples. Recently, Maestre-Reyna *et al*.[29] observed the photoinduced conformational changes in the corresponding Arg/Asp salt bridge in a class II CPD photolyase from *Methanosarcina mazei* (*Mm*CPDII) by time-resolved serial femtosecond crystallography (TR-SFX). However, no such movements of the helices flanking the salt bridge was observed in the molecular movie of *Mm*CPDII captured by TR-SFX. This is not mysterious because the amino acid sequence identity between *At*64 and *Mm*CPDII is low (~23%) and Thr375 and Ser410 in *At*64 are not conserved in *Mm*CPDII (Figure 4). These differences suggest that the hydrogen-bonding formation between α15 and α17 upon photoreduction would govern the helix movements. A recent molecular dynamics simulation of *Drosophila melanogaster* cryptochrome

(*Dm*CRY) in the FAD_{ox} and $FAD^{\bullet-}$ states suggested the possibility that the perturbation of the Arg/Asp salt bridge could play a role in a large structural change of its C-terminal tail extension (CTE)[31]. Although there were no descriptions about the movements of the helices corresponding to the α15 and α17 helices in *At*64 in the report, their results clearly indicated that higher root mean square fluctuation (RMSF) values in the helices were found out in the $FAD^{\bullet-}$ state than in the FAD_{ox} state. I tentatively assumed that the origin of the fluctuation in *Dm*CRY can be assigned to the helix movement observed in *At*64, because *Dm*CRY also possesses the Thr and Ser residues corresponding to Thr375 and Ser410 in *At*64 (Figure 4, even though *At*64 and *Dm*CRY share only 37% of amino acid residues). The HDX-MS measurements of *At*64 and the structural analyses of other PCSf proteins suggest a unified picture of the structural movement that stabilizes the reduced state of FAD (Figure 5). First, the extraordinarily conserved Arg/Asp salt bridge is rearranged upon the reduction of FAD. In the case of (6–4) PLs and animal cryptochrimes, which possess Thr and Ser residues in the helices flanking to the Arg/Asp salt bridge, the two helices get closer to each other, so that a hydrogen bond is formed between the Thr and Ser residues, to stabilize the anionic reduced FAD states ($FAD^{\bullet-}$ and $FADH^{-}$).

	367	375	396	410
*At*64	ARHCV	ACFLT	IDSDW	WMWLS
*Xl*64	ARHAV	ACFLT	LDADW	WLWLS
*Dm*64	ARHAV	ACFLT	LDSDW	WQWLS
*Dm*CRY	LRNTV	ATFLT	LDADW	WMWVS
*Ec*CPD	LRMIT	ASFLV	IDGDL	WQWAA
*Mm*CPDII	TRMYW	AK---	LDGRD	IAWSI
*At*CRY1	IRVVV	SSFFV	LDADL	WQYIT
*At*CRY2	IRVIV	SSFAV	LDADL	WQYIT

Figure 4. Sequence alignments of representative PCSf proteins. The Arg367/Asp396 salt bridge (red) is exclusively conserved among the proteins. The proposed hydrogen bond between Thr375 and Ser410 (green) could be formed in (6-4) PLs and *Dm*CRY. It is noted that the following abbreviations are used: *At* = *Arabidopsis thaliana*; *Xl* = *Xenopus laevis*; *Dm* = *Drosophila melanogaster*; *Ec* = *Escherichia coli*; *Mm* = *Methanosarcina mazei*; 64 = (6–4) photolyase; CRY = cryptochrome; CPD = cyclobutane pyrimidine dimer photolyase; CPDII = class II cyclobutane pyrimidine dimer photolyase

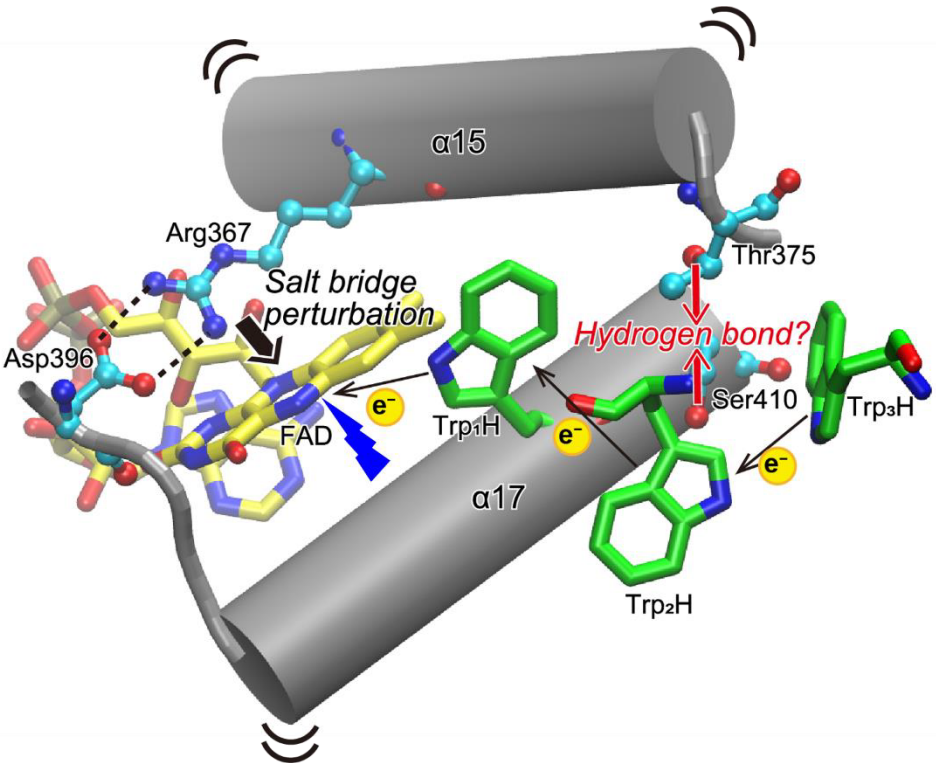

Figure 5. Schematic illustration for photoinduced structural changes in *At*64. The photoinduced electron transfer between FAD and Trp residues (in green) perturbs the Arg367/Asp396 salt bridge. The structural rearrangement could make the α15 and α17 helices closer. The position of helices may be locked by a hydrogen bond between Thr375 and Ser410.

4.3.2 Low midpoint potential of FAD characteristic for (6–4) PLs

Apart from the discussion of the photoinduced conformational change in *At*64, it is noted that this electrochemical measurement is the first determination of the midpoint potential of the $FAD_{ox}/FADH^-$ couple in (6–4) PLs. The value calculated for *At*64-WT is surprising, because CPD PLs have much higher midpoint potential ($E_m = -289 \pm 5$ mV vs. SHE for *At*64-WT vs. $E_m = -182 \pm 2$ mV vs. SHE for *Escherichia coli* CPD PL[34]), in spite of the shared repair mechanisms among (6–4) PLs and CPD PLs, in which they employ the photoinduced electron transfer from $FADH^-$ to UV-induced lesions. In a previous study[28], evaluated oxidation kinetics of $FADH^-$ to FAD_{ox} for (6–4) PLs exhibited a tendency of a faster $FADH^-$ oxidation in (6–4) PLs than in CPD PLs. The observation can be explained by the lower midpoint potential measured for *At*64-WT. The low midpoint potential for *At*64 could be drawback in keeping the repair-active $FADH^-$ state in (6–4) PLs. It could, however, be beneficial for the electron transfer from $FADH^-$ to the substrates, which is the first reaction step for the repair. In future, it will be addressed how PCSf proteins including (6–4) PLs optimize midpoint potentials of FAD for their functions in detail. This study suggests that the hydrogen-bonding formation between Thr375 and Ser410 could be one of the factor to regulate the midpoint potential in *At*64.

4.4 Methods

Plasmid construction and protein purification

Plasmid construction and purification of *At*64 variants were conducted as previously described[28]. The mutation of T375V was introduced into the pET-28a(+) plasmid carrying the *At*64-WT gene with the QuikChange Site-Directed Mutagenesis Kit. The set of PCR primers was as follows: d(TAGCCTGTTTTCTTGTTCGTGGGGATCTGT) and d(ACAGATCCCCACGAACAAGAAAACAGGCTA). As for the T375A mutant, the 5' upstream and 3' downstream of the mutation site were separately amplified using the following primer sets: d(CCGCGCGGCAGCCATATGGCTACTGGATCCGGT) and d(ATCCCCACGAGCAAGAAAACA) for the fragment on the 5' side; d(TGTTTTCTTGCTCGTGGGGAT) and d(GTGGTGGTGCTCGAGCTATTTGAGTTTTGGTCGTTG) for the fragment on the 3' side. The amplicons were fused into the pET-28a(+) vector linearized with *Nde*I and *Xho*I treatment, by using the In-fusion HD Cloning Kit (Takara). The obtained plasmids were sequenced.

E. coli C41 (DE3) /pLysS (Lucigen) cells were transformed with a pET-28a(+) plasmid containing the (6–4) PLs gene for the protein production. The protein was produced and purified as previously described[28] and confirmed by 10% SDS-PAGE. The concentration was measured based on the FAD absorbance at 450 nm using a molar extinction coefficient of 11,300 L mol^{-1} cm^{-1}.

HDX-MS measurement

HDX-MS was essentially carried out as described previously[35]. The injection of the respective samples was done manually, due to the requirement of blue-light illumination (λ_{max}= 455 nm, 224,41 µmol·m^{-2}·s^{-1}) for the fully reduced state (FADH^{-}). 5 µL (50 µM) *At*64 was diluted with 45 µL of D_2O-containing buffer (50 mM Tris-HCl, 500 mM NaCl, 5% glycerol, pH 8.0) and incubated for 10, 100, 1000 or 10000 s at 25 °C. H/D exchange was stopped by mixing 50 µL of the sample with an equal volume of quench buffer (400 mM KH_2PO_4/H_3PO_4, 2 M guanidine-HCl, pH 2.2) kept at 1 °C and immediately injected into an ACQUITY UPLC M-class system with HDX technology (Waters)[36]. *At*64 was digested with immobilized pepsin at 12 °C in water +0.1% (v/v) formic acid at a flow rate of 100 µL/min and the resulting peptides were trapped on a C18 column at 0.5 °C. After 3 minutes, the C18 trap column was placed in line with an ACQUITY UPLC BEH C18 1.7 µm 1.0 × 100 mm column (Waters), and the peptides were separated at 0.5 °C with a gradient of water +0.1% (v/v) formic acid (eluent A) and acetonitrile +0.1% (v/v) formic acid (eluent B) at a flow rate of 30 µL/min. The gradient was as follows: 0–7 min/95–65% A, 7–8 min/65–15% A, 8–10 min/15% A, 10–11 min/5% A, 11–16 min/95% A. Mass spectra were recorded on a G2-Si HDMS mass spectrometer (Waters) in High Definition MS (HDMS) positive ion mode[37,38]. [Glu1]-fibrinopeptide B (Waters) was used for lock-mass correction. Non-deuterated samples of *At*64 were prepared similarly employing non-deuterated buffer (50 mM Tris-HCl, 500 mM NaCl, 5% glycerol, pH 8.0). Here, mass spectra were acquired in Enhanced High Definition MS (HDMS) positive ion mode. For another round of injection, the immobilized pepsin was washed three times with 80 µl of

4% (v/v) acetonitrile and 0.5 M guanidine hydrochloride. All measurements were performed in triplicates. Peptide identification and assignment of deuterium incorporation were done using the PLGS and DynamX 3.0 software (Waters), respectively, as described elsewhere[35].

Midpoint Potential Measurement

Midpoint potentials of FAD in *At*64 variants were measured by a method based on a slow electron supply from a xanthine/xanthine oxidase reaction[32]. In detail, a protein was buffer-exchanged to Redox Buffer (20 mM Phosphate, 500 mM NaCl, 10% glycerol, pH 7.0) with a Micro Bio-Spin 6 column (BIO-RAD) and mixed with a reference dye (Safranin T) solution. The volume of the protein and Safranin T was set to ensure an absorbance of >0.3 at 450 nm and 510 nm. The sample was transferred into an anaerobic 10 × 2 × 8 mm (length × width × height) inner volume quartz cuvette (Starna, 16.160-F/4/Q/10 GL 14/2/Z15) and degassed through the cap with rubber septa. To avoid inflowing of oxygen into the sample, the cuvette was transported into a glove box. In the glove box, a redox mediator methylviologen (30 μM final conc.), xanthine (300 μM final conc.), glucose (10 mM final conc.), 25 μg of glucose oxidase, and 50 μg of catalase were mixed. After incubation for 15 min to decompose the remaining oxygen by glucose, glucose oxidase, and catalase, xanthine oxidase (94 nM final conc.) was added to start electron supply to the system. The absorption changes at two selected wavelengths (two of 450 nm, 510 nm and 635 mm) were recorded every 10 s for 1 or 3 h by a UV/Vis V-730 spectrometer (JASCO). In addition, UV/Vis spectra were recorded to check

the structural integrity and the reaction progress before and after the measurement, by Lambda 35 UV-vis spectrometer (PerkinElmer). The data were analyzed by Equation 4 as described in ***4.2.2***.

Steady-state photoreduction kinetics

Steady-state photoreduction for recombinantly-produced proteins was performed under anaerobic conditions as previously described[28]. 70 μL of protein diluted to 20 μM was applied to a Micro Bio-Spin 6 column (BIO-RAD) equilibrated with a reaction buffer (20 mM phosphate, 500 mM NaCl, 10% glycerol, pH 7.5). An aliquot (60 μL) of the eluate was transferred into an anaerobic 10 × 2 × 8 mm (length × width × height) inner volume quartz cuvette (Starna, 16.160-F/4/Q/10 GL 14/2/Z15). After the cuvette was sealed with a screw cap and PTFE-coated silicone and rubber septa, the air inside the cuvette was replaced with nitrogen through the septa. Further preparation was performed in an anaerobic glovebox. The sample was mixed with L-cysteine (the final concentration was 5 mM) and the reaction buffer up to a total volume of 240 μL under anaerobic and dark conditions.

The anaerobic samples were illuminated with continuous light (430 – 800 nm) from a MAX-150 xenon lamp (Asahi Spectra) through the 10 mm × 8 mm window on ice (illumination time varied depending on the sample). After shaking the sample gently, an absorption spectrum was recorded through the 10 mm path by Lambda 35 UV-vis spectrometer (PerkinElmer). The absorbance at 450 nm of the obtained spectra was plotted and fitted with a monophasic exponential decay function with the Origin2019 software.

4.5 Conclusions

So far, cryptochromes have drawn a great attention due to their photoresponsive structural changes required to express their functions, but the possibility that their evolutionarily relative photolyases undergo conformational changes to perform their functions has not been addressed well. In this study, I investigated the structural changes upon photoreduction of FAD in *A. thaliana* (6–4) photolyase. HDX-MS measurements suggested that the structural changes should occur (to smaller extent than that in cryptochromes) in α15 and α17 and may trigger a helix movement to make the helices closer by forming a hydrogen bond between Thr375 and Ser410. Furthermore, the helix movement was supported by mutational experiments, in which the replacement of Thr375 in *At*64 into Val disturbed midpoint potentials of FAD and FAD photoreduction kinetics. Inspired by these results, I proposed a model (Figure 5): the anion on FAD produced by photoinduced electron transfer from a nearby Trp residue disturbs the Arg367/Asp396 salt bridge residing near FAD and triggers conformational rearrangements of the α15 and α17 helices, which may be locked by a hydrogen bond between Thr375 and Ser410 to stabilize *At*64 in catalytically active $FADH^-$ state. Because the key residues for the changes are strongly conserved among other (6–4) PLs and animal cryptochromes, the proposed mechanism could be involved in drastic structural changes observed in animal cryptochromes, represented by *Drosophila melanogaster* cryptochrome.

Reference

1. Sancar, A., Structure and function of DNA photolyase and cryptochrome blue-light photoreceptors. *Chem. Rev.* **103**, 2203–2237 (2003).
2. Muller, M. & Carell, T., Structural biology of DNA photolyases and cryptochromes. *Curr. Opin. Struct. Biol.* **19**, 277–285 (2009).
3. Chaves, I., Pokorny, R., Byrdin, M., Hoang, N., Ritz, T., Brettel, K., Essen, L. O., van der Horst, G. T., Batschauer, A. & Ahmad, M., The cryptochromes: blue light photoreceptors in plants and animals. *Annu. Rev. Plant Biol.* **62**, 335–364 (2011).
4. Ahmad, M. & Cashmore, A. R., HY4 gene of *A. thaliana* encodes a protein with characteristics of a blue-light photoreceptor. *Nature* **366**, 162–166 (1993).
5. Guo, H. Yang, H., Mockler, T. C. & Lin, C., Regulation of flowering time by *Arabidopsis* photoreceptors. *Science* **279**, 1360–1363 (1998).
6. Sancar, A., Regulation of the mammalian circadian clock by cryptochrome. *J. Biol. Chem.* **279**, 34079–34082 (2004).
7. Collins, B., Mazzoni, E. O., Stanewsky, R. & Blau, J., *Drosophila* CRYPTOCHROME is a circadian transcriptional repressor. *Curr. Biol.* **16**, 441–449 (2006).
8. Chaves, I., Yagita, K., Barnhoorn, S., Okamura, H., van der Horst, G. T. & Tamanini, F., Functional evolution of the photolyase/cryptochrome protein family: importance of the C terminus of mammalian CRY1 for circadian core oscillator performance. *Mol. Cell. Biol.* **26**, 1743–1753 (2006).
9. Zoltowski, B. D., Vaidya, A. T., Top, D., Widom, J., Young, M. W. & Crane, B. R., Structure of full-length *Drosophila* cryptochrome. *Nature* **480**, 396–399 (2011).
10. Berntsson, O., Rodriguez, R., Henry, L., Panman, M. R., Hughes, A. J., Einholz, C., Weber, S., Ihalainen, J. A., Henning, R., Kosheleva, I., Schleicher, E. & Westenhoff, S., Photoactivation of *Drosophila* melanogaster cryptochrome through sequential conformational transitions. *Sci. Adv.* **5**, eaaw1531 (2019).
11. Ozturk, N., Selby, C. P., Annayev, Y., Zhong, D. & Sancar, A., Reaction mechanism of *Drosophila* cryptochrome. *Proc. Natl. Acad. Sci. USA* **108**, 516–521 (2011).
12. Vaidya, A. T., Top, D., Manahan, C. C., Tokuda, J. M., Zhang, S., Pollack, L., Young, M. W. & Crane, B. R., Flavin reduction activates *Drosophila* cryptochrome. *Proc. Natl. Acad. Sci. USA* **110**, 20455–20460 (2013).
13. Chandrasekaran, S., Schneps, C. M., Dunleavy, R., Lin, C., DeOliveira, C. C., Ganguly, A. & Crane, B. R., Tuning flavin environment to detect and control light-induced conformational switching in *Drosophila* cryptochrome. *Commun. Biol.* **4**, 249 (2021).
14. Conrad, K. S., Manahan, C. C. & Crane, B. R., Photochemistry of flavoprotein light sensors. *Nat. Chem. Biol.* **10**, 801–809 (2014).
15. Lin, C., Top, D., Manahan, C. C., Young, M. W. & Crane, B. R., Circadian clock activity of cryptochrome relies on tryptophan-mediated photoreduction. *Proc. Natl. Acad. Sci. USA* **115**, 3822–3827 (2018).

16. Byrdin, M., Eker, A. P., Vos, M. H. & Brettel, K., Dissection of the triple tryptophan electron transfer chain in *Escherichia coli* DNA photolyase: Trp382 is the primary donor in photoactivation. *Proc. Natl. Acad. Sci. USA* **100**, 8676–8681 (2003).
17. Brazard, J., Usman, A., Lacombat, F., Ley, C., Martin, M. M., Plaza, P., Mony, L., Heijde, M., Zabulon, G. & Bowler, C., Spectro-temporal characterization of the photoactivation mechanism of two new oxidized cryptochrome/photolyase photoreceptors. *J. Am. Chem. Soc.* **132**, 4935–4945 (2010).
18. Liu, Z., Tan, C., Guo, X., Li, J., Wang, L., Sancar, A. & Zhong, D., Determining complete electron flow in the cofactor photoreduction of oxidized photolyase. *Proc. Natl. Acad. Sci. USA* **110**, 12966–12971 (2013).
19. Müller, P., Yamamoto, J., Martin, R., Iwai, S. & Brettel, K., Discovery and functional analysis of a 4th electron-transferring tryptophan conserved exclusively in animal cryptochromes and (6–4) photolyases. *Chem. Commun.* **51**, 15502–15505 (2015).
20. Lacombat, F., Espagne, A., Dozova, N., Plaza, P., Müller, P., Brettel, K., Franz-Badur, S. & Essen, L. O., Ultrafast oxidation of a tyrosine by proton-coupled electron transfer promotes light activation of an animal-like cryptochrome. *J. Am. Chem. Soc.* **141**, 13394–13409 (2019).
21. Heelis, P. F., Payne, G. & Sancar, A., Photochemical properties of *Escherichia coli* DNA photolyase: selective photodecomposition of the second chromophore. *Biochemistry* **26**, 4634–4640 (1987).
22. Ceriani, M. F., Darlington, T. K., Staknis, D., Mas, P., Petti, A. A., Weitz, C. J. & Kay, S. A., Light-dependent sequestration of TIMELESS by CRYPTOCHROME. *Science* **285**, 553–556 (1999).
23. Koh, K., Zheng, X. & Sehgal, A., JETLAG resets the *Drosophila* circadian clock by promoting light-induced degradation of TIMELESS. *Science* **312**, 1809–1812 (2006).
24. Ozturk, N., Selby, C. P., Zhong, D. & Sancar, A., Mechanism of photosignaling by *Drosophila* cryptochrome: role of the redox status of the flavin chromophore. *J. Biol. Chem.* **289**, 4634–4642 (2014).
25. Paulus, B., Bajzath, C., Melin, F., Heidinger, L., Kromm, V., Herkersdorf, C., Benz, U., Mann, L., Stehle, P., Hellwig, P., Weber, S. & Schleicher, E., Spectroscopic characterization of radicals and radical pairs in fruit fly cryptochrome - protonated and nonprotonated flavin radical-states. *FEBS J.* **282**, 3175–3189 (2015).
26. Yamada, D., Yamamoto, J., Zhang, Y., Iwata, T., Hitomi, K., Getzoff, E. D., Iwai, S. & Kandori, H., Structural changes of the active center during the photoactivation of *Xenopus* (6–4) photolyase. *Biochemistry* **55**, 715–723 (2016).
27. Yamada, D., Zhang, Y., Iwata, T., Hitomi, K., Getzoff, E. D. & Kandori, H., Fourier-transform infrared study of the photoactivation process of *Xenopus* (6–4) photolyase. *Biochemistry* **51**, 5774–5783 (2012).
28. Hosokawa, Y., Sato, R., Iwai, S. & Yamamoto, J., Implications of a water molecule for photoactivation of plant (6–4) photolyase. *J. Phys. Chem. B* **123**, 5059–5068 (2019).

29. Maestre-Reyna, M., Yang, C. H., Y., Nango, E., Huang, W. C., Putu, E. P. G. N.,Wu, W. J., Wang, P. H., Franz-Badur, S., Saft, M., Emmerich, H. J., Wu, H. Y., Lee, C. C., Huang, K. F., Chang, Y. K., Liao, J. H., Weng, J. H., Gad, W., Chang, C. W., Pang, A. H., Sugahara, M., Owada, S., Hosokawa, Y,. Joti, Y., Yamashita, A., Tanaka, R., Tanaka, T., Fangjia, L., Tono, K., Hsu, K. C., Kiontke, S., Schapiro, I., Spadacini, R., Royant, A., Yamamoto, J., Iwata, S., Essen, L. O., Bessho, Y. & Tsai, M. D., Serial crystallography captures dynamic control of sequential electron and proton transfer events in a flavoenzyme. *Nat. Chem. in press* (2022).
30. Holub, D., Lamparter, T., Elstner, M. & Gillet, N., Biological relevance of charge transfer branching pathways in photolyases. *Phys. Chem. Chem. Phys.* **21**, 17072–17081 (2019).
31. Wang, Y., Veglia, G., Zhong, D. & Gao, J., Activation mechanism of *Drosophila* cryptochrome through an allosteric switch. *Sci. Adv.* **7** (2021).
32. Maklashina, E. & Cecchini, G., Determination of flavin potential in proteins by xanthine/xanthine oxidase method. *Bio. Protoc.* **10**, e3571 (2020).
33. Zhu, W., Haile, A. M., Singh, R. K., Larson, J. D., Smithen, D., Chan, J. Y., Tanner, J. J. & Becker, D. F., Involvement of the beta3-alpha3 loop of the proline dehydrogenase domain in allosteric regulation of membrane association of proline utilization A. *Biochemistry* **52**, 4482–4491 (2013).
34. Damiani, M. J., Nostedt, J. J. & O'Neill, M. A., Impact of the N5-proximal Asn on the thermodynamic and kinetic stability of the semiquinone radical in photolyase. *J. Biol. Chem.* **286**, 4382–4391 (2011).
35. Franz-Badur, S., Penner, A., Strass, S., von Horsten, S., Linne, U. & Essen, L. O., Structural changes within the bifunctional cryptochrome/photolyase *Cr*aCRY upon blue light excitation. *Sci. Rep.* **9**, 9896 (2019).
36. Wales, T. E., Fadgen, K. E., Gerhardt, G. C. & Engen, J. R., High-speed and high-resolution UPLC separation at zero degrees Celsius. *Anal. Chem.* **80**, 6815–6820 (2008).
37. Li, G. Z., Vissers, J. P., Silva, J. C., Golick, D., Gorenstein, M. V. & Geromanos, S. J., Database searching and accounting of multiplexed precursor and product ion spectra from the data independent analysis of simple and complex peptide mixtures. *Proteomics* **9**, 1696–1719 (2009).
38. Geromanos, S. J., Vissers, J. P., Silva, J. C., Dorschel, C. A., Li, G. Z., Gorenstein, M. V., Bateman, R. H. & Langridge, J. I., The detection, correlation, and comparison of peptide precursor and product ions from data independent LC-MS with data dependant LC-MS/MS. *Proteomics* **9**, 1683–1695 (2009).

List of Publications

1. **Yuhei Hosokawa**, Ryuma Sato, Shigenori Iwai, and Junpei Yamamoto, Implications of a water molecule for photoactivation of plant (6–4) photolyase. *J. Phys. Chem. B* **123**, 5059–5068 (2019).
2. **Yuhei Hosokawa**, Pavel Müller, Hirotaka Kitoh-Nishioka, Shigenori Iwai, and Junpei Yamamoto, Limited solvation of an electron donating tryptophan stabilizes a photoinduced charge-separated state in plant (6–4) photolyase. *Submitted*.

List of Related Publications

1. Junpei Yamamoto, Kohei Shimizu, Takahiro Kanda, **Yuhei Hosokawa**, Shigenori Iwai, Pascal Plaza, and Pavel Müller, Loss of fourth electron-transferring tryptophan in animal (6–4) photolyase impairs DNA repair activity in bacterial cells. *Biochemistry* **56**, 5356–5364 (2017).
2. Ayaka Morimoto, **Yuhei Hosokawa**, Hiromu Miyamoto, Rajiv Kumar Verma, Shigenori Iwai, Ryuma Sato, and Junpei Yamamoto, Key interactions with deazariboflavin cofactor for light-driven energy transfer in *Xenopus* (6–4) photolyase. *Photochem. Photobiol. Sci.* **20**, 875–887 (2021).
3. Manuel Maestre-Reyna, Cheng-Han Yang, Eriko Nango, Wei-Cheng Huang, Eka Putra Gusti Ngurah Putu, Wen-Jin Wu, Po-Hsun Wang, Sophie Franz-Badur, Maritin Saft, Hans-Joachim Emmerich, Hsiang-Yi Wu, Cheng-Chung Lee, Kai-Fa Huang, Yao-Kai Chang, Allan Pang, Michihiro Sugahara, Shigeki Owada, **Yuhei Hosokawa**, Yasumasa Joti, Ayumi Yamashita, Rie Tanaka, Tomoyuki Tanaka, Luo Fangjia, Kensuke Tono, Kai-Cheng Hsu, Stephan Kiontke, Igor Schapiro, Roberta Spadaccini, Antoine Royant, Junpei Yamamoto, So Iwata, Lars-Oliver Essen, Yoshitaka Bessho, and Ming-Daw Tsai, Serial crystallography captures dynamic control of sequential electron and proton transfer events in a flavoenzyme. *Nat. Chem. in press* (2022).

International Symposium

1. **Yuhei Hosokawa**, Ryuma Sato, Shigenori Iwai, and Junpei Yamamoto, Impact of a water molecule on photoreduction of (6-4) photolyase, DFG Roundtable Discussion Meeting “Conformational Dynamics of Photoreceptors at a Different Time Scales”, Castle Ringberg, Germany, Oct. (2019).

Acknowledgments

The present studies have been carried out at Division of Chemistry, Graduate School of Engineering Science, Osaka University, during 2016–2022 under the supervision of Professor Shigenori Iwai.

I would like to express heartfelt appreciation to Professor Shigenori Iwai of Osaka University for insightful discussions and continuous supports throughout the course of the study. I wish to give special thanks to Associate Professor Junpei Yamamoto for his invaluable instructions and enormous help in all the time of my research. I would like to express gratitude to Assistant Professor Miyako Shiraishi for constructive comments and technical supports. I would also like to thank Professor Keiichiro Suzuki for his treasured comments. I thank all the members of the Professor Iwai's group, especially Dr. Yuma Terai, Ms. Ayaka Morimoto, Mr. Hiroyoshi Morita, Mr. Hiromu Miyamoto, Ms. Mai Nakamura, and Mr. Takahiro Kanda.

My research would not have been possible without the support of many collaborators. I would like to express gratitude to Dr. Ryuma Sato of Otsuka Pharmaceutical Co., Ltd. for his kind support, which was really influential in shaping my computational analyses. I also thank Dr. Pavel Müller of Université Paris-Saclay (France) for his enormous contribution to time-resolved absorption spectroscopic studies. I appreciate the team of Professor Lars-Oliver Essen of Philipps Universität Marburg (Germany), especially Mr. Martin Saft, to help me conduct mass spectrometric experiments. I am grateful to Professor Shuji Nakanishi of Osaka University for sharing his anaerobic glovebox. I thank you to all the people who taught me precious scientific techniques.

I appreciate the financial support from JSPS KAKENHI Grant Number JP 21J13329.

Finally, I would like to extend my sincere thanks to my family, especially Mr. Akinobu Hosokawa, Ms. Satoko Hosokawa, Mr. Kenji Hosokawa, Mr. Minoru Kawabata, and Ms. Eiyo Kawabata. Thank you for your warm encouragement.

March 2022

Yuhei Hosokawa